Development of a Micro-thermal Sensor Based on 3-omega Technique for Dynamic
Freezing Applications

A DISSERTATION
SUBMITTED TO THE FACULTY OF
UNIVERSITY OF MINNESOTA BY

Harishankar Natesan

IN PARTIAL FULFILLMENT OF THE REQUIREMENTS
FOR THE DEGREE OF
DOCTOR OF PHILOSOPHY

Advisor: John C. Bischof

March 2019

Dedication

In memory of my dad.

Abstract

Atrial Fibrillation (AF) is a major heart disease affecting millions of people every year. If left untreated, AF can cause cardiovascular disease, stroke and even death. Cryoablation for PV (Pulmonary Vein) isolation has been used for more than 10 years in AF treatment, which involves freezing ($< -60\ ^0C$) and subsequent scarring of PV using a cold balloon/ catheter surface. Despite widespread and growing clinical use, the precise dosing and treatment times for cryoablation can vary depending on cooling surface contact, tissue thickness, and freeze completion through the wall. Without this knowledge, the treatment can be expected to have diminishing efficacy and may contribute to collateral injury. For instance, under-freezing may lead to inadequate treatment, while over-freezing can damage adjacent tissues (esophagus, lung and nerves), thereby creating complications. Clearly, there is a need to monitor this process to ensure complete treatment while avoiding complications. Unfortunately, the approaches for monitoring cryotherapy in the treatment of other diseases using clinical imaging cannot work for PV due to poor spatial resolution (mm). Thus, there is a pressing need to improve monitoring of cryoablation of the PV to reproducibly supply information on freezing within tissues at the millimeter to sub-millimeter level. Here then we present a response to this need through development of a micro- thermal sensor based on the "3ω" technique. We propose that a disposable thermal sensor based on 3ω technology can be deployed on a balloon to measure tissue contact, thickness and the initiation and completion of freezing in the PV all with an accuracy better than 1 mm.

The 3ω technique, on which the sensor is based, was originally developed for thin inorganic materials. The technique was first modified for measurement of thermal conductivity of soft, hydrated biological tissues. Using the new sensor, for the first time, we have measured the

thermal conductivity of thin porcine cardiac tissues *in vitro* addressing a major knowledge gap to inform focal therapy modeling for atrial fibrillation. This information is critical for successful treatment planning/prediction of therapy impact in the PV and surrounding tissues.

Next, we show a dynamic use of the sensor for monitoring an idealized therapy in *in vitro* thin tissues (≤ 2 mm). For this, we demonstrated the ability of the sensor (on a flat substrate) to sense contact, flow, tissue thickness and freeze front in idealized systems. Specifically, the sensor was used to sense contact with tissue vs. water, ice (frozen agargel) thickness, and freeze initiation and completion. The success of this study suggests that integration of "3ω" sensors onto cardiology probe surfaces (i.e. balloons or catheters) can monitor cryoablation and by extension other PV focal therapies.

As a next step, we integrated these sensors onto cryoballoons using transfer printing techniques. The 3ω sensor technology has traditionally been used for flat and rigid substrates. Therefore, we modified the shape of the sensor from a linear to a serpentine shape for integration onto balloon substrates. Next, using numerical analyses, we investigated the ability of the modified sensor on a flat substrate to differentiate measurements in limiting cases of ice, water and fat. These numerical results were then complemented by experimentation by micro-patterning the serpentine sensor onto a flat substrate and onto a flexible balloon. In both formats (flat and balloon) the serpentine sensor was experimentally shown to: (1) identify tissue contact vs. fluid, (2) distinguish tissue thickness in the 0.5 to 2 mm range, and (3) measure the initiation and completion of freezing as previously reported for a linear sensor. This study demonstrates proof of principle that a

serpentine 3ω sensor on a balloon can monitor tissue contact, thickness and phase change which is relevant for cryo and other focal thermal treatments of PV to treat atrial fibrillation.

Table of Contents

List of Tables

List of Figures

0. Statement of Contributions

The thesis work consists of three stand-alone publications in the first three chapters, which have been subjected to peer-review process, while Chapter 4 has been submitted for publication as well.

Chapter 1 is a review article that is authored by myself under the guidance of Dr. John Bischof. This chapter discusses new measurement tools and opportunities for thermal conductivity and specific heat capacity measurement of biological tissues at the micro and nanoscale.

Natesan, H., & Bischof, J. C. (2017). Multiscale thermal property measurements for biomedical applications. ACS Biomaterials Science & Engineering, 3(11), 2669-2691.

Chapter 2 is a textbook chapter that is authored by Shaunak Phatak and myself under the guidance of Dr. John Bischof. In this chapter, we have compiled thermal conductivity and specific heat capacity values of human and porcine systems in the subzero and supra-zero temperature ranges for the purposes of aiding the development of accurate models of conditions and pathologic treatments involving bio-heat transfer mechanisms.

Phatak, S., Natesan, H., Choi, J., Sweet, R., & Bischof, J. (2017). Thermal Properties of Porcine and Human Biological Systems. Handbook of Thermal Science and Engineering, Kulacki, F. (Eds.), Springer 1-26.

Chapter 3 is a technical article that showed thermal conductivity measurements of porcine thin cardiac tissues for the first time using 3ω technique. Further, we demonstrate that a micro-thermal sensor based on the *3ω* technique can sense tissue contact, thickness and phase change *in vitro* under idealized conditions in 0.5 to 2 mm thick tissues relevant to cryoablation of the pulmonary vein (PV). This article is authored by myself and Dr. John Bischof with assistance of Wyatt Hodges, Dr. Sean Lubner, Dr. Jeunghwan Choi and Dr. Chris Dames. I, Dr. Jeunghwan Choi and

Dr. John Bischof contributed to the conception and design of the experiment to measure thermal conductivity, sense contact and thickness. Wyatt Hodges, Dr. Sean Lubner and Dr. Chris Dames contributed to the conception and carried out experiments to sense phase change. Wyatt Hodges and Chris Dames carried out the theoretical comparison for thickness and phase change experiments.

Natesan, H., Hodges, W., Choi, J., Lubner, S., Dames, C., & Bischof, J. (2016). A micro-thermal sensor for focal therapy applications. Scientific reports, 6, 21395.

Chapter 4 is a technical article that focuses on modifying the micro-thermal sensor from a linear format to a serpentine format for integration onto a flexible balloon. Next, using numerical analyses, the ability of the modified sensor on a flat substrate was studied to differentiate measurements in limiting cases of ice, water and fat. These numerical results were then complemented by experimentation by micro-patterning the serpentine sensor onto a flat substrate and onto a flexible balloon. In both formats (flat and balloon) the serpentine sensor was experimentally shown to: (1) identify tissue contact vs. fluid, (2) distinguish tissue thickness in the 0.5 to 2 mm range, and (3) measure the initiation and completion of freezing as previously reported for a linear sensor. The numerical analysis and experimentation were performed by me. These sensors were integrated onto balloons by Dr. Limei Tian and Dr. John Rogers. The article was written by me under the guidance of Dr. John Bischof with assistance on sensor fabrication sections from Dr. Tian and Dr. Rogers.

Natesan, H., Tian, L., Rogers, J., & Bischof, J. In submission to Journal for Biomechanical Engineering

Chapter 5 consists of conclusion and future research directions for this thesis work authored by me under the guidance of Dr. John Bischof.

Appendix A is a technical article that discusses about the adaptation of the 3ω method—widely used for rigid, inorganic solids—into a reusable sensor to measure k of soft biological samples, two orders of magnitude thinner than conventional tissue characterization methods. Analytical and numerical studies quantify the error of the commonly used "boundary mismatch approximation" of the bi-directional 3ω geometry, confirm that the generalized slope method is exact in the low-frequency limit, and bound its error for finite frequencies. Dr. Sean Lubner authored the manuscript under the guidance of Dr. Chris Dames with assistance from Dr. Jeunghwan Choi, Geoff Wehmeyer, Bastian Waag, Vivek Mishra, myself, and Dr. John Bischof. I confirmed the results of thermal conductivity of mouse liver using a second 3ω instrument that I built at Bioheat and Mass Transfer Lab at the University of Minnesota.

Lubner, S. D., Choi, J., Wehmeyer, G., Waag, B., Mishra, V., Natesan, H., Bischof, J., & Dames, C. (2015). Reusable bi-directional 3 ω sensor to measure thermal conductivity of 100-µ m thick biological tissues. Review of Scientific Instruments, 86(1), 014905.

Appendix B is a technical article that shows microporous poly (ε-caprolactone) biomaterials could be used to attract metastasizing breast cancer cells *in vivo* early in tumor progression. In order to enhance the therapeutic potential of these scaffolds, they were modified such that infiltrating cells could be eliminated with non-invasive focal hyperthermia. My contribution was to measure thermal conductivity and specific heat capacity of the scaffolds infiltrated with cells post-harvest. I also assisted in the writing sections on thermal property measurement of this manuscript.

Pelaez, F., Manuchehrabadi, N., Roy, P., Natesan, H., Wang, Y., Racila, E., ...,Bischof, J., & Azarin, S. M. (2018). Biomaterial scaffolds for non-invasive focal hyperthermia as a potential tool to ablate metastatic cancer cells. Biomaterials, 166, 27-37.

Appendix C is a technical article that is not directly related to my thesis work. Using DSC, the specific heat capacity of five CPAs was measured. c_p was measured in the minimal and maximal cases of crystallization for VS55 and DP6 to understand their crystallization behavior. This chapter was authored by Shaunak Phatak with assistance from myself, Dr. Jeunghwan Choi, Dr. Kelvin Brockbank under the guidance of Dr. John Bischof. The experimentation and modeling work was led by Shaunak Phatak with assistance from myself.

Phatak, S., Natesan, H., Choi, J., Brockbank, K. G., & Bischof, J. C. (2018). Measurement of Specific Heat and Crystallization in VS55, DP6, and M22 Cryoprotectant Systems With and Without Sucrose. Biopreservation and biobanking, 16(4), 270-277.

1. Multi-Scale Thermal Property Measurements for Biomedical Applications

The following chapter has been reproduced with permission from "*Natesan, H., & Bischof, J. C. (2017). Multiscale thermal property measurements for biomedical applications. ACS Biomaterials Science & Engineering, 3(11), 2669-2691*" Copyright 2017 American Chemical Society

1.1. Introduction

Bioheat transfer based innovations in health care include applications such as focal treatments for cancer and cardiovascular disease and the preservation of tissues and organs for transplantation. As outlined in Table 1.1, biodestruction, (commonly known as focal or thermal therapy) and biopreservation comprise the two main applications of bioheat transfer. Thermal therapy refers to the application of heat or cold to destroy tumors and other diseased systems in the body[1]. Recently, there has been a major drive towards use of thermal therapy to ablate thin tissues (<5 mm thick) for cardiovascular and other diseases. For instance, Medtronic has received FDA approval for ArcticFront[TM] cryoballoons, which cryoablate pulmonary veins (< 2mm thick) for the treatment of atrial fibrillation, and work is underway to establish renal and hepatic arteries as targets for thermal treatment of hypertension and diabetes, respectively[2-4].

Biopreservation refers to the preservation of biomaterials (Table 1.1) to increase their shelf lives for tissue and organ transplant (i.e. regenerative medicine), in vitro fertilization, germplasm preservation of endangered species and food science. Biopreservation, which involves cooling biomaterials to very low temperatures (<-80 ^{0}C) in the presence of cryoprotective agents (CPAs) at specific rates to slow down all biological activity, is important for successful organ banking[5]. At least 1 in 5 patients die waiting for an organ transplant, making it one of the most pressing medical problems of the 21st century[6]. In fact, The White House has called for "new breakthroughs treating cancer and ending the wait for organ transplants" and has directed hundreds of millions of federal

5

Table 1.1. Overview of common bioheat transfer applications

(Modified with permission from [15]. Copyright 2016 World Scientific

	Application	Temperature	Description	Rep. ref.*
Biopreservation	Vitrification	<-140 °C	Preservation by attaining a glassy state	[10-11]
	Freezing	<-20 °C	Preservation by freezing in presence of cryoprotective agents (CPA)	[8-9]
	Lyophilization/ Freeze Drying	<-20 °C	Preservation by drying after freezing	[12-14]
	Hypothermic preservation	0 to 36 °C	Preservation at temperatures between 0 °C and 36 °C	[16-17]
Biodestruction	Cryotherapy/ Cryoablation	<-20 °C	Destruction of tissue by freezing	[18-19]
	Mild hyperthermia	37 to 43 °C	As an adjuvant to sensitize tumors to radiation and chemotherapy	[20]
	Thermal ablation	>50 °C	Destruction of tissue by heating	[21]

*Representative reference

dollars to research and development[7] in those fields. Long term preservation involves storing the biomaterials at low temperatures (~-80 °C)[8-9] or in a glassy/vitrified state (<-130 °C)[10-11] so as to slow down metabolism and biological activity. In some cases, as in lyophilization[12-14], this involves dehydration by freezing followed by storage at room temperature.

The ability to preserve or destroy is directly dependent on the temperature history of the biomaterials. Thus, thermal measurement and modeling are necessary to either avoid or induce the injury required. A commonly used equation to model this thermal behavior is called the bioheat equation,

$$\rho c_p \frac{\partial T}{\partial t} = \nabla.(k\nabla T) + Q_{bl} + Q_m + Q_s \tag{1.1}$$

where thermophysical properties of biomaterials such as density (ρ), specific heat capacity (c_p) and thermal conductivity (k) can be experimentally measured, usually *in vitro* to avoid the interference of perfusion with the measurement. Q_{bl} is the blood perfusion term, which reduces the efficacy of thermal therapies by acting as a heat sink. For cryoablation, the biomaterials will have two phases: frozen and unfrozen, and Q_{bl} would be absent in the frozen regime. For cryopreservation, Q_{bl} would always be absent as the tissues would already have been removed from the body. Heat source term (Q_s) refers to the endothermic/ exothermic heat release from several phase change events generally associated with water, but to a lesser extent proteins and lipids in the biomaterial. Q_s and Q_{bl} are typically large compared to metabolic heat generation (Q_m) and hence Q_m is sometimes neglected[61]. Thus, measurement of thermal properties (k, Cp), latent heat and phase change temperatures is necessary for a complete understanding of the heat transport in biomaterials. In this review paper, we will first define and discuss thermal property measurements of biomaterials. Next, we will

Table 1.2. Overview of thermal conductivity 'k' measurement techniques

Biomaterial	k measurement	Length Scale	Rep. Ref.
Macroscale	[a]Steady state	> 2 mm	22-24,25
	[b]Transient		26-28 29-30 31-36 37-39 40-44
Thin Tissue scale	Supported 3ω	10 μm- 2 mm	45-47
	Laser flash		48-50
Cellular scale	Supported 3ω	1- 100 μm	43, 51-52
	[c]TDTR	100 nm- 1 μm	53-54
	[d]SThM	Spatial: 50-500 nm Vertical: 1-10 nm	55-56
Molecular scale	TDTR	50 - 100 nm	53-54
	[e]TAM	1-20 nm	57-60

[a]Steady state techniques include: guarded hot plate[22-24], radial heat flow[25]
[b]Transient techniques include: thermal comparator[26-28], heated thermocouple[29-30], transient hot wire[31-36], transient thermistor probe[37-39], pulsed decay[40-44]
[c]TDTR- Time Domain Thermoreflectance
[d]SThM- Scanning Thermal Microscopy
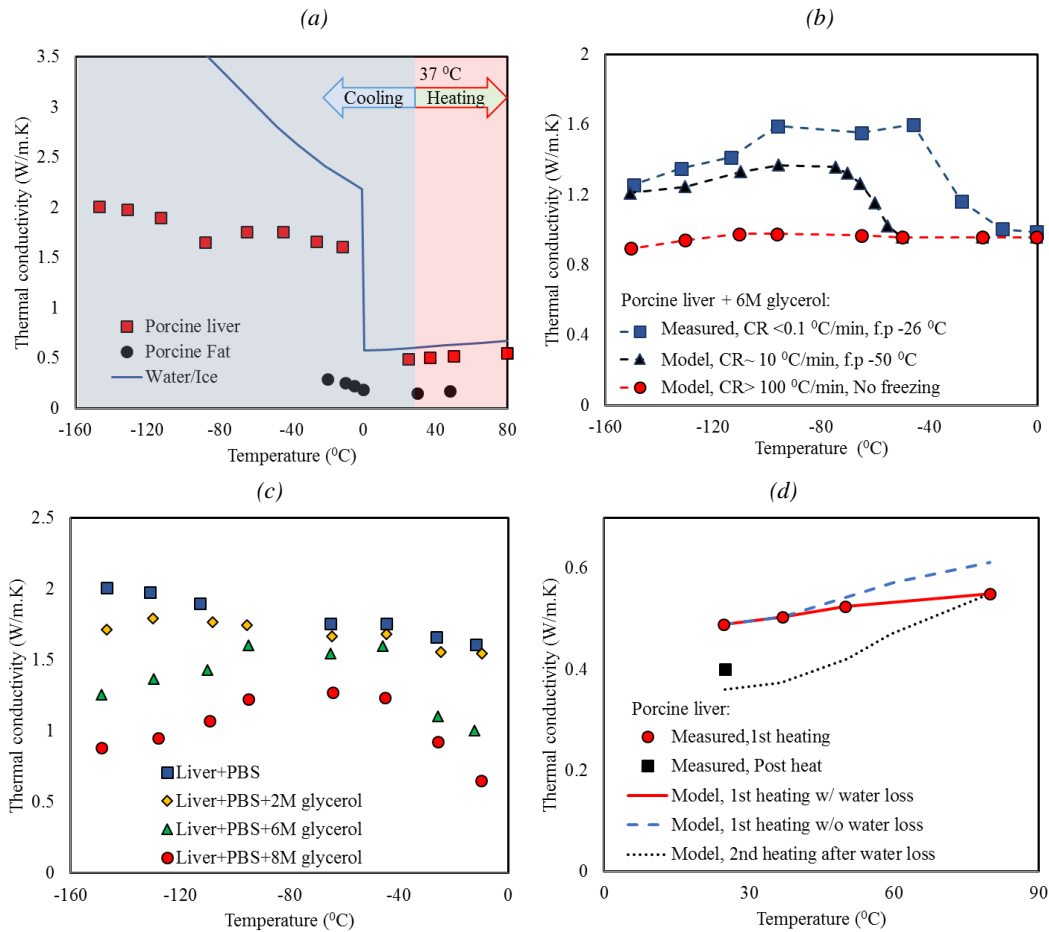
Figure 1.1. Thermal conductivity measurement of biomaterials. *(a) Thermal conductivity of porcine tissues as a function of temperature. Porcine liver[62], with >70% water content has higher k than porcine fat[63] with <10% water content and lower k than water/ice. Frozen liver has higher k than that of fresh liver due to freezing of the water content; (b) Thermal conductivity of porcine liver +6 M glycerol determined at different cooling rates from 0 0C to -150 0C. Higher cooling rates lead to lower crystallization fraction and hence higher k; (c) Thermal conductivity of porcine liver treated with PBS (phosphate buffer saline) solution and varying glycerol concentrations; (d) Thermal conductivity of porcine liver during first heating and post heating. Water loss after first heating reduces k as supported by the results of the model. Figures (b), (c) and (d) are redrawn from [14,62,43]. Copyright 2010, 2008, 2013 Elsevier, Elsevier, and American Society of Mechanical Engineers.*

explain various micro and nanoscale measurement techniques which currently define the limits of these measurement techniques. Finally, we will discuss various opportunities that are driving the need for new micro and nanoscale measurements.

1.2. Thermal Properties of Biomaterials

The thermal properties of a biomaterial refer to its thermal conductivity and calorimetric parameters such as specific heat capacity, latent heat and phase change temperature of various internal molecular events. Portions of this review were significantly modified and refined from a larger chapter on thermal conductivity written by the authors[15].

1.2.1. Thermal conductivity of biomaterials

Thermal conductivity (k) is an important property of biomaterials that determines its ability to transfer heat. Using Fourier's law, k can be expressed as, $k = -Q/\nabla T$, where Q is heat flux (W/m^2) and ∇T is temperature gradient (K/m). A common technique to determine k is to apply a known heat flux followed by measuring the resulting temperature gradient in the biomaterial. Though Fourier's law can break down at small length and time scales, it is generally valid for biomaterials[15]. Historically, thermal conductivity measurement of biomaterials began with refrigerated foods. In such cases, k of biomaterials was either directly measured[22-23, 73-74] or predicted using models developed based on weight averaging of the composition[75-78]. The pursuit of thermal conductivity measurement of macroscale biomaterials has led to several bulk methods, which have been reviewed in detail elsewhere[14]. These techniques cannot be used for thin tissues or cellular systems (1 μm - 2 mm) due to the inherent limitation of using larger probes (>1 mm). Further, these

Table 1.3. Overview of calorimetric measurement techniques

Bio-material	Calorimetric measurement	Typical sample size	Temperature scan rate (^{0}C/min)	Rep. Ref.
Tissue scale	*DSC	1-10 μL	<750	62
Cellular scale	*DSC	1-10 μL	<750	64
	Nanocalorimetry	0.5- 1 nL	<1,000	65-66
Molecular scale	Nanocalorimetry	1-100 pL	<10,000,000	67-72

*DSC- Differential Scanning Calorimetry

measurements and models do not take into account the temperature dependence of k especially for temperatures $< -40\ ^0C$ and $> 40\ ^0C$[14, 79]. Finally, k of biomaterials is measured under quasi equilibrium, which cannot be applied to non-equilibrium situations like cryopreservation, where the biomaterial often undergoes supercooling, vitrification, and/or devitrification[80]. For instance, a biomaterial subjected to higher cooling rates would more likely possess lower crystal fractions. In this case, a lower fraction of crystals would reduce k closer to that of water and a larger fraction of crystals would increase its k value closer to that of ice in a cooling rate dependent manner. Recently, a number of studies have been able to account for this by making non-equilibrium measurements of k as a function of both temperature and thermal history (eg. cooling rate)[14, 35-36, 80]. As shown in Fig. 1.1, the value of k for a typical biomaterial is influenced by composition (water, protein, and lipids), phase (water vs ice), non-equilibrium conditions (cooling rate), additive concentration (e.g. CPAs), and water loss at suprazero temperatures. Several thermal conductivity measurement techniques listed in Table 1.2 will be reviewed in Section 1.3.

1.2.2. Calorimetric measurements of biomaterials

Calorimetric measurement broadly includes the measurement of specific heat capacity, latent heat during phase change and phase change temperature in biomaterials. These parameters can be used to study the kinetics and the thermodynamics of phase change events that in some sense are a quantitative metric of the injury process. Similar to k, specific heat capacity (c_p) of biomaterials with and without CPAs need to be measured and they typically follow the trends at suprazero and subzero temperatures as shown in Fig 1.2.

Next, latent heat is another important parameter in calorimetric measurements. For instance, water, protein, lipids, DNA and RNA are building blocks of biomaterials. Any change to their phase or native state can result in direct biological injury. For instance, at sub-physiological temperatures in

10

(a)
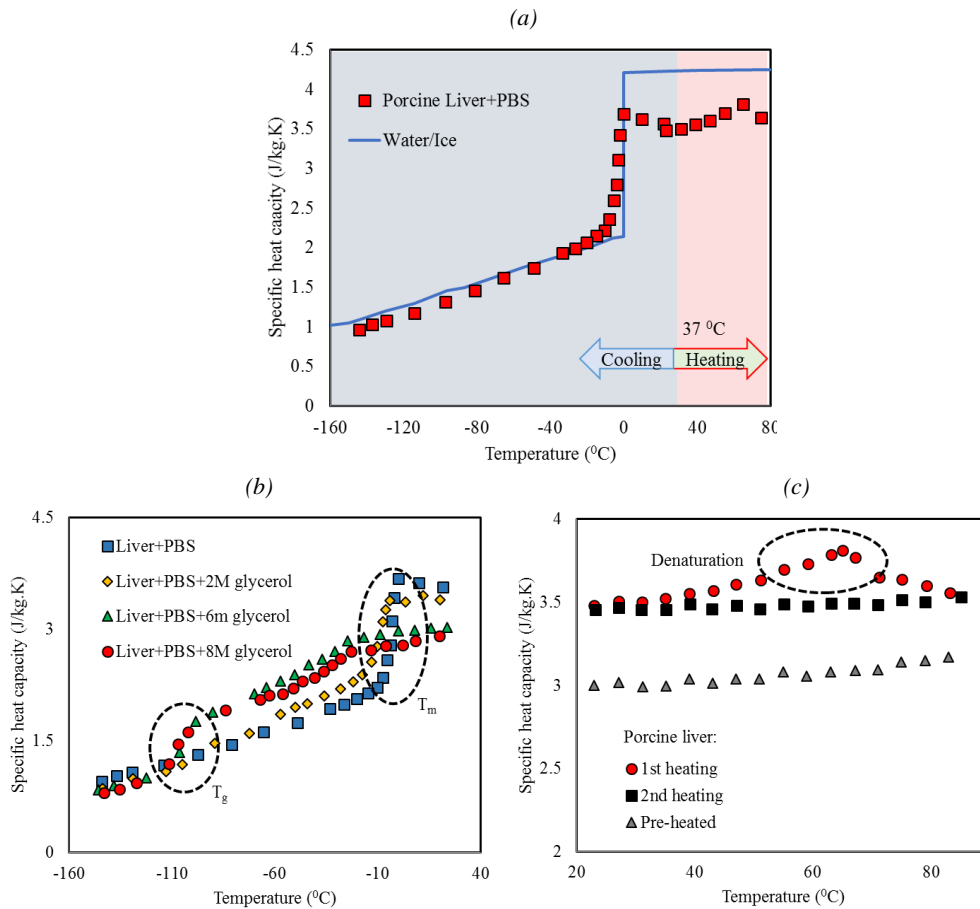
Figure 1.2. Specific heat capacity measurement of biomaterials.(a) *Specific heat capacity of porcine liver in PBS* [14] *(b) Specific heat capacity of porcine liver in PBS with and without glycerol solutions during heating from -150 ^0C to 25 ^0C at 5 ^0C/min; Temperature regions corresponding to glass transition (T_g) and melting peaks (T_m) are denoted by dotted lines; (c) Apparent specific heat capacity of porcine liver during heating from 20 ^0C to 85 ^0C. Apparent c_p term includes latent heat and sensible heat. In 1st heating, protein denatures irreversibly releasing latent heat. During 2nd heating, c_p does not show latent heat release for T>40 ^0C. c_p 1st and 2^n heating samples are measured using DSC inside a closed pan. Pre- heated samples are first heated in ambience and then measured using DSC. Thus, they have lower c_p due to water loss from evaporation. Figures (b, c) are redrawn from* [43, 81]. *Copyright 2013 Elsevier and American Society of Mechanical Engineers*

cryobiology, water-ice phase change is one of the most important events linked to cell injury (Fig. 1.3). At slower cooling rates (<10 ^0C/min in fibroblasts), water leaves the cell due to osmotic imbalance resulting in cellular dehydration[82]. At high cooling rates (>60 ^0C/min in fibroblasts), water can supercool and often result in intracellular ice formation (IIF)[83]. Importantly, these biophysical responses are highly dependent on the size and type of cell[9] and the attachment state which enhances both IIF and water transport[84-88]. Further, at supraphysiological temperatures

11

during focal thermal therapies, lipids undergo melting, inducing hyperpermeability of membranes and protein denaturation, both of which have been linked to the injury process[89,64]. Based on such overwhelming evidence, it is clear that these phase change events are critical determinants of either life or death after temperature changes. Calorimetric measurement of such events is an important step towards understanding and improving bioheat transfer processes. Several measurement techniques are outlined in Table 1.3.

1.3 Thermal Conductivity Measurement Techniques

1.3.1. Microscale thermal conductivity measurement techniques

Commonly used 3ω and laser flash methods for inorganic materials, introduced in Table 1.4, are now techniques that can be adapted for measuring thermal conductivity of thin tissues and systems.

i. 3ω method

For the past three decades, the 3ω method has been a popular and effective tool in measuring thermal conductivity of thin inorganic materials such as amorphous solids[47], multilayered films[90-92] with anisotropy[93-94], suspended wires [95] and even liquids[96-98]. The principle of this technique, originally developed by Cahill is illustrated in Fig. 1.4 (a). The measurement comprises a long, thin metallic heater line (1 to 3 mm long, 10 to 100 μm wide, <100 nm thick) microfabricated onto a sample of interest. By applying alternating current ($I_0 \sin(\omega t)$), the heater line is electrically heated with a DC and an AC component, $Q_{AC} = Q_0 \sin(2\omega t)$. At the heater line, these components of Joule heating produce a temperature response with a corresponding DC and '2ω' AC component. The AC temperature oscillations propagates and decays radially away from the heater resembling a semi-cylinder with a radius of penetration depth $(D/2\omega)^{0.5}$, where D is the thermal diffusivity. The length of the semi-cylindrical region affected by the temperature oscillations of the heater line is approximately the length of the heater line as well. Importantly, the magnitude of the temperature
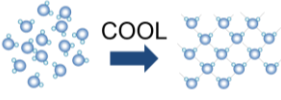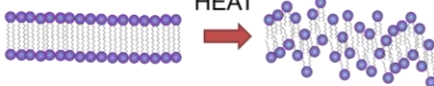
Cellular phase change events	Structural changes at the molecular level	Phase change Temperature (^{0}C)	Heat release (J/g)
Freezing of pure water[99]	COOL	<0 ^{0}C	334
Freezing of biomaterials[14]		<0 ^{0}C	100-300
Melting of pure lipids[100]	HEAT	>30 ^{0}C	1-10
Denaturation of pure proteins[101]	HEAT	>40 ^{0}C	1-50

Figure 1.3. Important phase change events on biomolecules with their corresponding latent heat. On cooling, water freezes upon supercooling below 0 ^{0}C. On heating, the lipids (> 30 °C) in the cell eventually change from lamellar to liquid crystalline phase. On further heating to above protein phase transition temperature (> 40 °C), native proteins in the cells denature to form folded proteins.

oscillations at the heater strip is inversely proportional to k of this semi-cylindrical region in the substrate. These oscillations containing information of k, subsequently cause the electrical resistance (R) of the heater line to fluctuate at '2ω'. Finally, when multiplied by the 1ω current, this 2ω resistance fluctuation causes a voltage oscillation across the heater at the 3rd harmonic, giving this method its name. This method can be defined a quasi-steady state technique as the AC temperature fluctuations (2ω) achieve a repetitive steady state for long time scales typically involved in the measurement (>>1/2ω).

The equation between thermal conductivity and the 3ω voltage can be derived based on a one dimensional heat transfer model where a semi-infinite solid is heated at the surface with an infinitely thin periodic heat source[47].

$$k_{\text{in phase}} = \left[\frac{V_{1\omega}^3}{4\pi l R^2} \frac{dR}{dT} \right] \frac{d\ln(\omega)}{dV_{3\omega,\text{in phase}}} \tag{1.2}$$

In Eqn. (1.2), R and dR/dT are obtained by calibrating the sensor to establish the R vs T relationship.

By sweeping the heater electrical frequency 'ω' and measuring the resulting in phase 3ω voltage,

13

Table 1.4. Micro-scale techniques for thermal conductivity measurement

(Reprinted from [15]. Copyright 2016 World Scientific

Technique	Heat source	Temperature Measurement	Heat transfer model	Directionality	Rep. Ref.
3ω method	[a]Electrical (1-1000 Hz)	Third harmonic voltage response	1-D Quasi- steady cylindrical	Cross plane and in plane	[47]
Laser flash method	[b]Optical (Single laser pulse)	Infrared detection of the opposite side	Transient Cylindrical	Cross plane and in-plane	[48, 102]

[a]Electrical- Heat source heated by Joule heating
[b]Optical- Heat source heated by photothermal effect

the slope $(dV_{3\omega, \text{ in phase}}/d(\ln \omega))$ can be experimentally determined and substituted in Eqn. (1.2). Hence this method is known as the slope method and offers several advantages. For instance, this technique is robust against contact resistance between the heater and the substrate. In addition, surface parasitic heat loss is negligible as the temperature oscillations are small (0.1- 1 ^{0}C) and localized within the substrate.

Recently, a new "supported" 3ω method (Fig. 1.4 (b)) has been developed. Instead of deploying the 3ω line on the substrate to be tested, the line is created on a separate substrate that is then brought into contact with the tissue. Thus, the temperature oscillations in this case would represent a cylinder, with each half being in the substrate and the tissue. This method allowed for the first-time the thermal conductivity measurements in thin porcine cardiac tissues[45, 103] (Fig. 1.4 (c)), biological solutions[104], and single cells[105]. The accuracy of this technique for fresh tissues/water is 6%-7% and for frozen tissues/ ice is 2%-5[45]. Further, as the tradition 3ω has been used to measure composite inorganic materials[91, 106], the same should be possible with supported 3ω method for composite tissues. A major issue during measurement of wet biological tissues and cells is water layer(s) and/or evaporation from the sample. A thin layer of water could form between the sample

and the sensor, which could result in overestimation of the k of the sample. Next, evaporation of water content in the biomaterial cools the sample (evaporation is endothermic), acting as a heat sink, results in a higher apparent k. Hence, it is necessary to monitor evaporation and/or water loss for accurate measurement in thin systems.

ii. Laser flash method

One of the earliest noncontact optical thermal conductivity techniques[48] is the laser flash method which can potentially be modified for use with biomaterials. As an established, ASTM standardized technique[107], scientists have used it extensively with thin films such as polymers (14- 250 µm thick) [108-109], carbon nanotubes (0.6-1.4 mm thick)[110], glass[111], metals (18 µm -1 mm thick)[112-114], materials with anisotropy[113], wood[115], and even liquids[50, 116] at both low (T > -268 ^{0}C)[117] and high temperatures[112] (>1000 ^{0}C). Further, it has been used to measure interfacial contact resistance[118-120]. The principle of operation is depicted in Fig. 1.5 (a). It is a transient technique, where the heat source is a short duration laser pulse. This approximates an instantaneous heat source heating one side of a sample. The thermal energy diffuses across the sample resulting in a temperature rise on the opposite side, usually measured by a thermocouple or an infrared thermometer. From the transient temperature rise, thermal diffusivity (α=k/ ρc) of the sample can be determined by applying a suitable thermal transport model. In contrast to 3ω technique, thermal conductivity is only indirectly determined from α if ρ and c are known. For instance, based on the one dimensional Cartesian developed by Parker and his co-workers[48], an expression for α and ρc is shown in the following equations,

$$\alpha = \frac{0.48L^2}{\pi^2 t_{1/2}} \quad (1.3)$$

where L is the sample thickness (m) and $t_{1/2}$ is time for the back surface to reach half the maximum temperature rise (s), and

15

$$\rho c = \frac{Q}{LT_m} \tag{1.4}$$

(a)

(b)

(c)   *(d)*
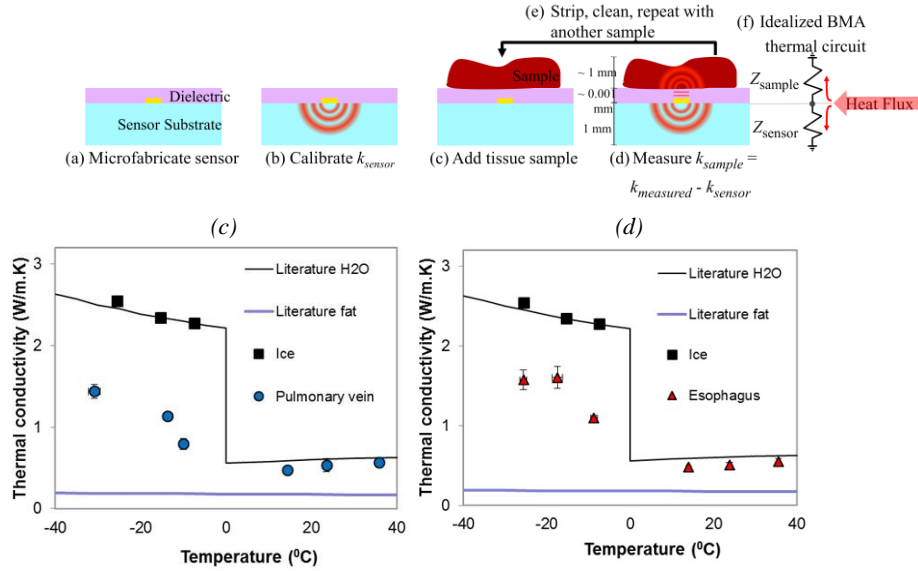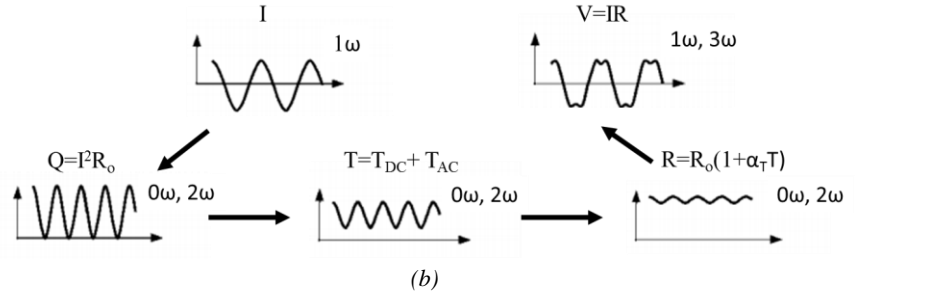
Figure 1.4. 3ω method. *(a) Principle of operation of the 3ω method (I- current, R- electrical resistance, Q- Joule heating, T- temperature, α_T- temperature coefficient of resistance), (b) Side view of supported 3ω method with steps involved in thermal conductivity measurement; (c) Supported 3ω measurements of porcine PV, and (d) esophagus. Measurements are the average ± standard deviation of N = 5 samples and validated using ice measurements (black points). The black and yellow trend-line data are k values of water, ice and fat from literature[121]. Figure (a) is reprinted and redrawn from [46]Figures (b), (c) are reprinted from [45], [103]. Copyright 2015 and 2016 American Institute of Physics and Nature*

where T_m is maximum temperature rise at the rear surface (K). Using α and ρc from Eqns. (1.3) and (1.4), thermal conductivity of the sample can be determined. An important error from this model arises from assuming the sample to be a black body, which absorbs all incoming radiation. This error can be minimized by applying a layer of black coating over the sample surface[122]. Other errors include the uncertainty in sample thickness, parasitic heat loss, finite pulse duration and multi-dimensional heat flow. The uncertainty of this technique is ±3-5%[123].

16
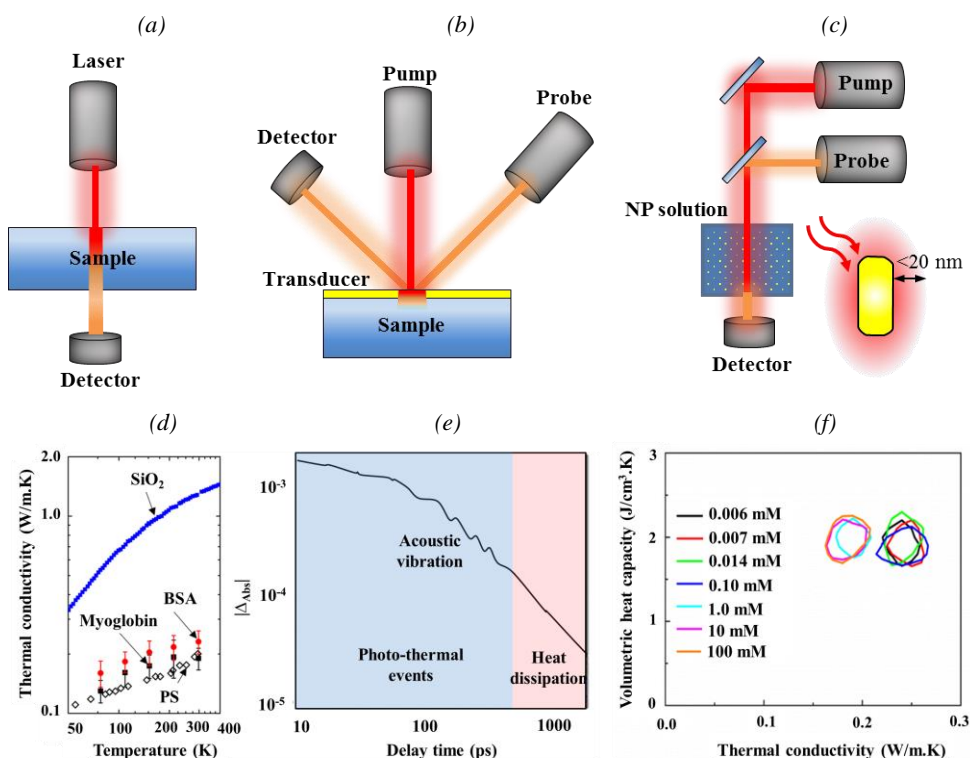
Figure 1.5. Optical techniques for thermal conductivity measurement. (a) Laser flash method, (b) Time-Domain Thermoreflectance Method; (c) Transient absorption method. Inset showing the heating of an individual gold nanorod with a coating (green color) heated by the pump beam; (d) Thermal conductivity measurement of thin protein films using TDTR. (e) Plot of transient absorption signal vs. time; (f) Thermal conductance and volumetric specific heat of CTAB coated on the gold nanorod surface. Figure from (d) reprinted from reference [124]. Figures (a) is modified from[15] and (e) and (f) are reprinted from [58]. Copyrights 2014, 2016, 2013 American Chemical Society, World Scientific and American Chemical Society

For applications with thin biological tissues (< 2 mm), this technique would face limitations from evaporative heat and water loss from the wet sample as also seen in 3ω method. Tada and co-workers addressed this limitation by encapsulating the liquid sample (~1 mm) between two thin metal disks held together by capillary force. As one of the metal disks is heated, heat diffuses from the disk through the liquid sample to the other side introducing the issue of contact resistance between the disk and the sample. Laser flash technique has been successfully used to measure the thermal conductivity of water[50], molten salt[125] and human tooth (1.2- 1.5 mm thick)[126].

1.3.2. Nanoscale thermal conductivity measurement techniques

Nanoscale thermal conductivity measurement techniques are advanced state of the art techniques developed for small length (1 nm-1 μm) and time scales (100 ps- 10 ns). A representative list is shown in Table 1.5, and discussed in the following sections.

i. Time domain thermoreflectance (TDTR) method

TDTR is a noninvasive optical technique that has been used to measure thermal conductivity of thin films[53, 127-128] with directionality[129-133] and composite layers[54]; and microscale liquid droplets[134] and thermal conductance across solid-solid interfaces[135], solid-liquid interfaces[136] across self-assembled monolayers of molecular chains[137] and even chemical bonds[138]. The technique uses a pump probe setup as shown in Fig 1.5 (b). A pump beam (spot size- 10-20 μm) produces ultrashort train of pulses (~100 fs) rapidly heating the sample surface. The surface subsequently cools down after each pulse at a specific rate depending on the thermal conductivity of the sample. This surface temperature drop changes the optical reflectance of the sample surface (thermoreflectance). After a suitable time delay (< 100 ps), the probe beam irradiates the surface and its reflection is detected by an optical sensor. By monitoring the change in reflectance, the optical sensor measures the temperature change and ultimately the thermal conductivity using a suitable thermal transport model. A simple one-dimensional Cartesian model can be approximated if penetration depth is smaller than the pump beam spot size (~10 μm-100 μm)[53-54, 127, 134]. In the case of biomaterials, penetration depth ($\sqrt{\alpha t}$) at ultrashort time scales (~100-1000 ps) corresponds to 100-600 nm in biomaterials.

For samples with poor thermoreflectance coefficient, a thin metallic transducer (e.g. gold, 50-100 nm thick) can be used as shown in Fig. 1.5 (b). TDTR has been used to measure thermal conductivity of thin protein films[124] (Fig. 1.5 (d)). The measurement accuracy is ~7% at probe beam

sampling frequency of 10 MHz[139]. A major source of uncertainty arises from the thickness and thermoreflectance behavior of the transducer. The transducer thickness can be reduced by the use of recently developed and highly sensitive transducer based on TR-MOKE (Time resolved Magneto Optical Kerr effect). In TR MOKE, the transducer is magnetic, whose highly sensitive temperature response to laser heat energy is measured based on thermo-magnetic and magneto-optical effects[133, 140-141]. TDTR faces several limitations in nanoscale bioheat transfer applications. First, the transducers generally have a weak but linear relationship between the optical reflectance and temperature. Hence, a temperature rise of the order of $10\,^0C$ is necessary for measurable change in the output signal[142], which is significantly higher than other techniques such as 3ω method (temperature rise~0.1- 1^0C[46]). Next, due to limitations with thin film geometry, thermal transport around nanoparticles in suspended medium cannot be measured.

A variation of TDTR is possible if the pump beam is modulated at a frequency 'ω' resulting in a periodic heat source. This technique, which has been used to measure thermal conductivity of materials such as thin metal films (20-100 nm thick)[143] with anisotropy, multilayer structures[144], carbon nanotubes[145] and thermal conductance at the interface[146], is referred to as frequency domain thermoreflectance method (FDTR)[147]. As the name implies, the change of the measuring parameter i.e., thermoreflectance of the transducer with pump beam frequency (100 kHz- 200 MHz) is fitted to an analytical model to determine k. As it relies of frequency change of the pump beam, the mechanical delay stage for probe beam is not needed reducing the complexity of the experimental setup. Further, the thermal penetration depth $(2\alpha/\omega)^{0.5}$ can easily be controlled by changing the modulated frequency of the pump beam. Also, this technique can simultaneously measure k and c_p and measure interface conductance if the thermal diffusivity is at least $3\text{x}10^{-6}$ m^2/s[147]. However,

thermal diffusivity of biomaterials is usually less than 2 x10^{-6} m^2/s. A disadvantage of this technique is that it has poor sensitivity for in plane thermal conductivity[147].

ii. Transient absorption method (TAM)

Similar to TDTR, TAM is also a pump-probe technique developed in the last decade to measure thermal conductivity of nanoparticle (NP) coating (1- 10 nm) and thermal conductance at the interface around nanoparticles in the suspended state. Metallic NP such as gold are the transducers of thermal energy through photo-thermal effect[148]. On laser irradiation, free electrons of the NP are excited to oscillate with a frequency depending on NP geometry and material. Surface plasmon resonance (SPR) occurs when the incident light frequency matches with the natural frequency of the free electrons. SPR significantly increases the absorbance of the nanoparticles. Following this absorption, several events ensue: (i) electron-electron coupling in the nanoparticle within 1 ps, followed by electron-phonon coupling for energy transfer from electron to the NP lattice over 1-10

Table 1.5. Nanoscale techniques for thermal conductivity measurement

(Reprinted from [15]. Copyright 2016 World Scientific)

Technique	Heat source	Temperature measurement	Heat transfer model	Directionality	Rep. Ref
Time domain thermoreflectance (TDTR) microscopy	[a]Optical – Laser (> 1 MHz pulsed)	Using surface reflectivity dependence on temperature	Transient	In- plane and cross plane	53-54
Transient Absorption Method (TAM)	[a]Optical – Laser (> 1 MHz pulsed)	Using Transmitted signal to measure absorbance	Transient	Spherical radial	57-60
Scanning Thermal Microscopy (SThM)	[b]Electrical	Thermocouple, thermistor or RTD	Quasi- steady model	Spherical radial	55-56

[a]Optical- Heat source heated by photothermal effect
[b]Electrical- Heat source heated by Joule heating

ps, (ii) thermal equilibration of the phonons across the particle, and the excitement of acoustic mode vibrations which cause oscillations in the measured signal at < 300 ps, and (iii) the diffusion regime, in which the NP lattice dissipates heat into the surroundings (hundreds of ps to a few ns). Therefore, nanoparticles act as transducers of laser thermal energy.

For temperature measurement, this technique relies on the relationship between temperature and
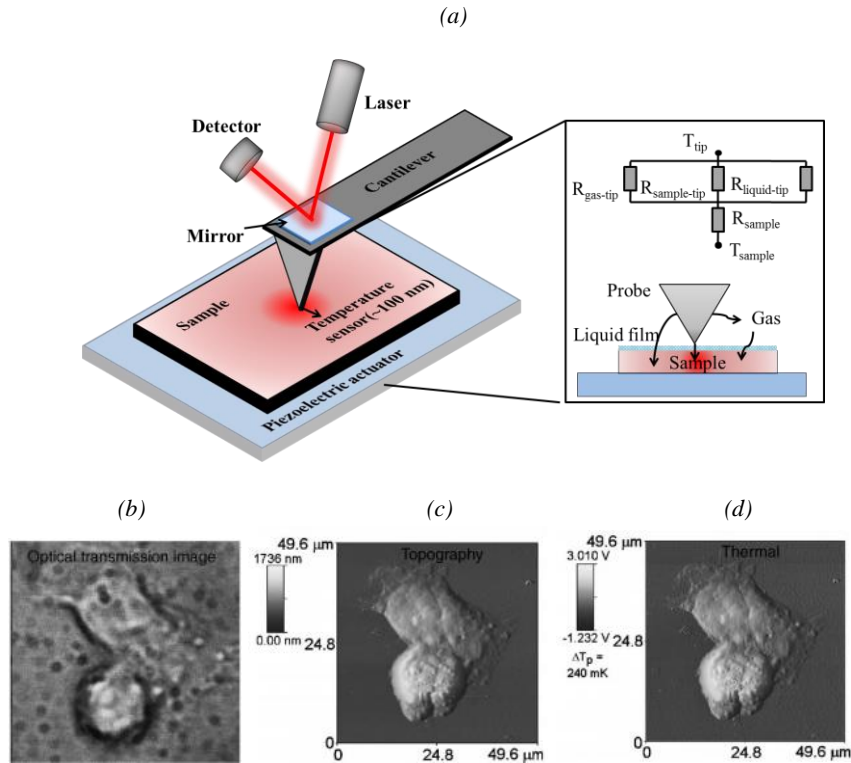
Figure 1.6. Scanning thermal microscopy. *(a) Schematic with the inset showing the heat transfer mechanism between the heated tip and the sample. (b) Optical Transmission image; (c) Topography; (d) Thermal image of nucleus of HeLa cells attached to a glass substrate undergoing mitosis. Figures (a) and (b-d) reprinted from* [15,149]*. Copyright 2016, 2003 World Scientific and Elsevier*

optical absorption of the nanoparticles instead of reflectance as in TDTR. The experimental setup is illustrated in Fig. 1.5 (c)[59-60, 150]. As a femtosecond pump beam heats the NPs, it is cooled by the surrounding medium. The subsequent temperature drop at short time scales (<1000 ps) changes the optical absorbance (Δ_{Abs}) of the NPs. After a time delay, the probe beam shoots an ultrashort pulse

through the nanoparticle solution. The change in the transmitted signal is monitored by a photo-detector. If the scattered signal is minimum, Δ_{Abs} can be determined from the transmitted signal. Thus, transient Δ_{Abs} behavior as shown in Fig. 1.5 (f) contains information about the temperature response of the NPs. However, the behavior of Δ_{Abs} at short time scales (<500 ps) is dominated by photo-thermal events such as phonon-electron coupling (<10 ps) and acoustic phonon vibrations (<100 - 500 ps) within the nanoparticle. Only above 500 ps, Δ_{Abs} represents the thermal dissipation from the hot nanoparticles to the surrounding medium. For time scale < 1000 ps, the penetration depth is of the order of 1-20 nm from the surface of the NP. Interestingly, this is of the same order as that of the NP coating thicknesses used in many biomedical applications. Therefore, thermal properties of the nanoparticle interface and coatings could be determined from Δ_{Abs} in the diffusion regime (500-1000 ps). A main drawback is that only certain nanoparticles with minimum scattering and maximum absorption qualify as suitable transducer for this technique. For instance, gold nanorods can be used with near infrared Ti-sapphire laser as they have minimum scattering and maximum absorption in the near infrared frequency regime (700-1000 nm). In addition, TEM relies on several characterization steps such as UV-vis absorption spectrometer, transmission electron microscopy, ζ-potential and dynamic light scattering measurements before measuring thermal properties. Nevertheless, TEM have been used to successfully measure the thermal properties (k, c_p) of the coatings such as CTAB and PEG (Fig. 1.5 (f))[57-58]. In some cases, the nanoparticles have also been immobilized on a quartz support and immersed in organic solvents to measure thermal conductance at the nanorod - fluid interface[150]. Therefore, TAM offers unique opportunities to address some unanswered questions about thermal transport around the nanoparticles at small time (<1000 ps) and length scales (1-20 nm)[151]

Several optical techniques such as laser flash method, TDTR and TAM have been discussed in the previous sections (Fig. 1.5). Apart from these techniques, there are other optical techniques such

22

as thermal lens microscopy[152] and photoluminescence[153] based methods used for measuring thermal conductivity and/or thermal diffusivity of biological cells. Though optical techniques are non-invasive and non-contact, the spatial resolution is limited by the diffraction limit of optics (~300 nm). Thus, SThM discussed in the next section accounts for this drawback by using a physical probe as detailed in the next section.

iii. Scanning thermal microscopy (SThM) method

SThM uses a nanoscale heated probe to qualitatively measure thermal conductivity[56, 154-158] or temperature[55, 159-161] on the sample surface or its sub-surface[162-164] in the range of hundreds of nm to µm range. The probe (~100 nm) can be microfabricated to simultaneously act as a heater and a thermometer[165]. The schematic of SThM is shown in Fig. 1.6. The probe is attached to a cantilever, while the sample sits on a stage. A mirror attached to a cantilever reflects light onto a photodiode to inform the vertical and horizontal movement of the probe. As the probe scans the surface, the sample surface displaces the probe depending on its topography. Meanwhile, the stage moves the sample to maintain constant gap between the probe and the sample surface. During the scan, a constant current heats the probe, while the sample surface cools it resulting in temperature decay (Fig. 1.6 (a-inset))[56]. This transient temperature change of the probe is monitored to qualitatively determine thermal conductivity of the sample near the surface.

This method has been used to probe inorganic nanomaterials such as carbon nanotubes[166] and polyethylene nanofibers[167] with a spatial resolution as small as 50 nm. SThM has been used directly on biomaterials, generating thermal images such as those inside of living HeLa tumour cells as shown in Fig. 1.6[149]. This suggests, for instance, that SThM may one day be able to directly measure the intracellular activity of different organelles or compartments of living cells. This technique can also measure phase change temperature at a single location[162, 168-172].

23

Despite the possibility of in situ thermal imaging of biomaterials by SThM, there are also several limitations. For instance, an important drawback is that it offers only qualitative measurements of thermal conductivity. As the thermal transport mechanism between the hot probe and the sample is complex and not fully understood (Fig. 1.6 (a-inset))[165, 173-175], proper heat transfer models and calibration techniques are still under development. Another drawback is that the temperature measurement is significantly affected by the surface roughness. For instance, topography and thermal imaging in HeLa cells appear highly correlated in Fig. 1.6 (b). If these limitations are overcome, this system is an excellent tool to physically probe thermal conductivity of sub-nanoscale intracellular components such as cytoplasm, nucleus, cell membranes in the presence of additives (i.e. chemical and NPs) and/or phase change (i.e. crystals).

1.3.3. Applications for multiscale thermal conductivity measurement

i. Thin tissue and cellular scale applications (10 nm- 2mm)

A recent review on the measurement of thermal properties of large tissues (>2 mm thick) and organs sheds light on lack of similar measurements in thin tissues (< 2 mm) and cells (<100 μm) in literature[14, 52, 176]. Further, thermal property measurement of thin, anisotropic and/or composite structures such as in Fig. 1.7 (a) remain largely unexplored. However, anisotropy in larger muscle tissues have been studied in the past as shown in Fig. 1.7 (b). During freezing, the presence of ice crystals significantly impact the thermal conductivity depending on its direction, fraction and morphology. First, crystal growth occurs in the direction of the temperature gradient thereby artificially introducing anisotropy in thermal conductivity. Directional crystal growth is commonly observed during cryoablation of tissues. Next, crystallized fraction is determined by the cooling rate as described in Section 1.2, which in turn affects the k to a large extent. Finally, the ice crystal morphology depends on the freeze front being planar, dendritic or epitaxial. One instrument, the

directional solidification stage, has been developed to study such crystal growth morphology[177]. This stage, also known as the Bridgeman technique, achieves anisotropic crystal growth by moving the sample at a given speed from a warm to a cold block with a temperature gradient of over 20 ^{0}C/mm. In solutions, the phase front develops from planar into dendritic structure (Fig. 1.7 (c). The space between the dendrites, which can be 10's μm, is occupied by an unfrozen region, which on further cooling becomes a eutectic mixture. The resulting ice crystal morphology would be alternating layers of ice and eutectic mixture (Fig. 1.7 (c)), resulting in an anisotropic, composite thermal conductivity. On freezing complex biological organs, ice crystals follow the open fluidic pathways for crystal growth such as vasculature extracellular spaces in liver and other organs[178-179]. It is unclear what the implications of this anisotropy are on frozen tissues during cryotherapy as it is largely unstudied. On the other hand, freezing during cryopreservation involves the random nucleation of small ice crystals. After nucleation, the ice crystals grow in random directions as shown in Fig. 1.7 (d) diminishing the issue of anisotropy[180].

In the case of cryopreservation, there is a need to study the influence of thermal history on thermal properties of thin tissues (eg. arteries)[181-182]. Specifically, vitrification often fails from crack formation and crystallization. The presence of ice crystals changes thermal property changes by 50 – 100% in crystallized vs. non-crystallized biomaterials as shown in Figs. 1 and 2. In the case of cracks, the ensuing voids would be expected to change the *k* value. Due to lack of microscale thermal conductivity measurement techniques, these areas of interest remain largely unexplored. Nevertheless, 3ω technique and laser flash method as discussed in Section 1.3 offer excellent opportunities to measure thermal properties of anisotropic, composite, and thin tissues and cells.

ii. Molecular scale applications (1-100 nm)

At small length scales (<100 nm) and short time scales (<100 ns), there are several bioheat transfer applications under development for biomolecular manipulation. For instance, at high temperatures, plasmonic nanosurgery uses pico to femtosecond laser pulses to optically heat metallic nanoparticles (e.g. gold) to achieve high local temperatures near the nanoparticle surface, even above the boiling point of water. Such techniques are used in several applications such as nanoscale membrane melting[185], selective protein denaturation[186], sub-wavelength surgery[187] and molecular drug release[188]. In these techniques, there is a need to predict the energy needed to attain necessary temperature at the nanoparticle surface. Thus, nanoscale techniques like TAM can be used as shown
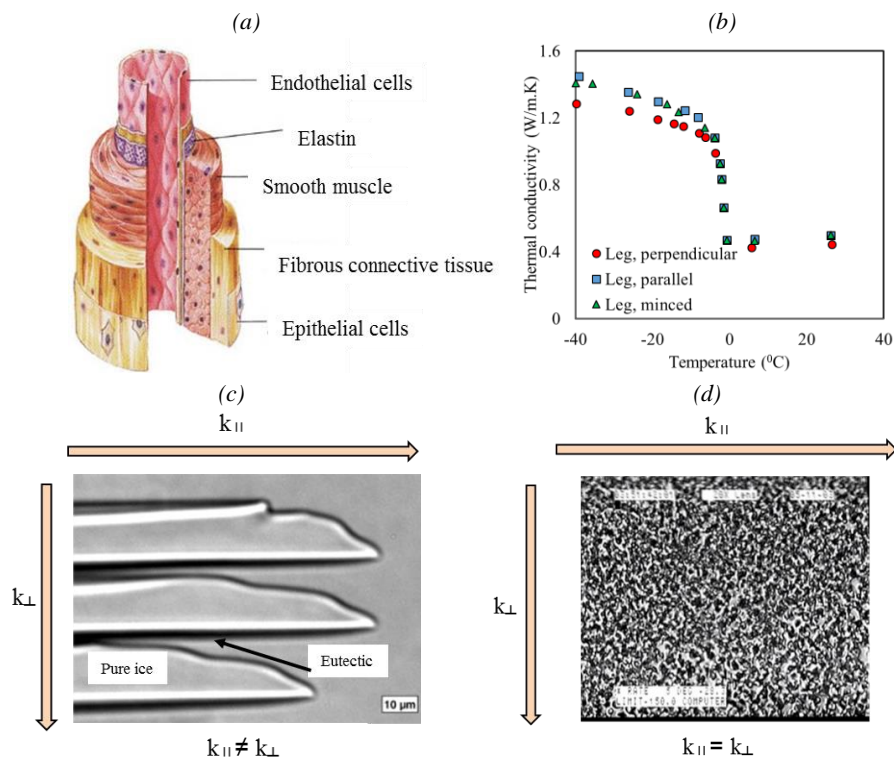
Figure 1.7. Microscale k measurement opportunities. *Example anisotropic, composite structures in microscale biomaterials (a) Anisotropy and radial composite structures in arteries with thickness of each layer <1 mm. (b) Measured k anisotropy in lamb leg muscle tissue. (c) Anisotropic ice crystal morphology due to directional freezing of isotonic saline solution vs. (d) Isotropic ice morphology in pre-nucleated 1X PBS+6M glycerol solution. Figures (a),(b),(c),(d) reprinted and redrawn from* [14, 183-184]. *Copyright 2010, 1989, and 1993 Elsevier, Wiley, and W.C. Brown*

in Fig. 1.8 to improve the understanding of thermal transport around nanoparticle surface at the nanoscale. Finally, a similar capability can be envisioned for TDTR for biological films of water, protein or polymers.

At low temperatures, nanoparticles are used in several instances for both cryopreservation and cryotherapy. In cryotherapy, nanoparticles (1-100 nm) can potentially be used as payloads to carry toxic drugs as a combinatorial treatment[189] and in some cases, molecular adjuvants that increase the efficacy of iceball for tumor destruction, reaching in some cases out entirely to the iceball edge[190]. For some applications of cryopreservation, nanoparticles are added to CPAs to improve their efficacy as cryopreservatives[191] or manipulating osmotic response of cell membranes to improve cryopreservation[192]. Recently, iron oxide nanoparticles are being used to uniformly thaw the biomaterials without cracking and crystallization thereby improving cryopreservation of larger biomaterials[193]. Due to low concentration of nanoparticles (<1% by volume), their effect on thermal conductivity of nanoparticle laden biomaterials is negligible. However, they can reduce perfusion (i.e. blood flow, Q_{bl}) in vivo[194]. On the other hand, cryo-nanosurgery uses a higher concentration of nanoparticles so as to directly increase the thermal conductivity and hence the efficacy of an ice ball[195]. As increasingly important biomedical applications open up at small length scales (<100 nm) and/or short time scales (<100 ns), there is a need to clearly understand the nanoscale heat transfer in nanoparticle-laden biomaterials.

1.4. Calorimetric Measurement Techniques

As a complement to the above thermal conductivity discussion, we will now transition to calorimetric measurement techniques of biomaterials. A commonly used technique is Differential scanning calorimetry (DSC) for measurement of latent heat and specific heat (c_p) at the microscale (e.g. mm sized tissue pieces or millions of cells in media). Though commonly used, these
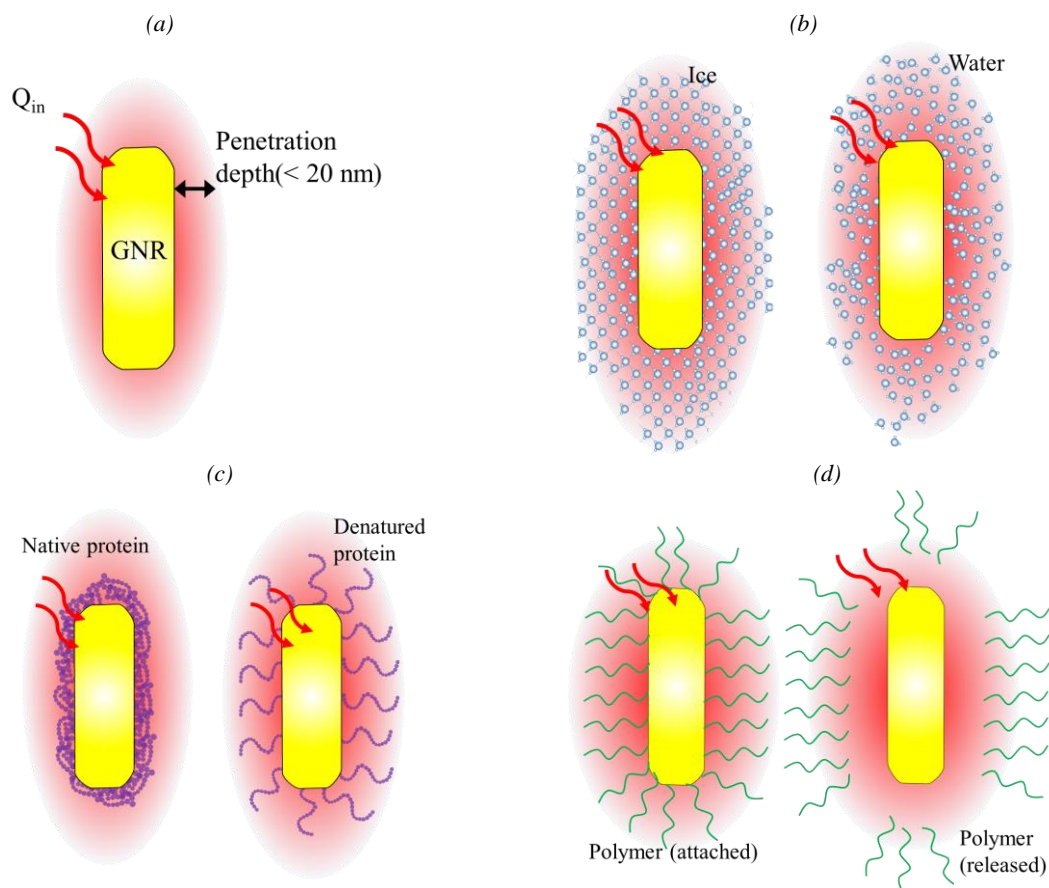
Figure 1.8. Example nanoscale thermal conductivity measurement opportunities. *(a) Schematic of TAM probing gold nanorod (GNR) surface up to 20 nm. (b) Heating of GNR melting ice to water[196]. Measured thermal conductivity will change from that of ice to water on heating. (c) Heating of protein coating resulting in denaturation surrounding the GNP surface[197]. Measured thermal conductivity will change from that of fully deployed native proteins to denatured proteins; (c) Measurement of molecular release event through monitoring of thermal conductivity at the surface[188].*

instruments have several limitations such as low temperature scanning rates (<750 ^{0}C/min) and large sample weight (> 1 mg). This has led to the development of Nanocalorimetry on a silicon-based membrane for small sample weight (as low as 10 ng), thereby allowing large heating rates (~10^7 ^{0}C/min). Nanocalorimetry can be ideal for applications at the cellular, sub-cellular and molecular levels, allowing a broad range of phase change behavior in biomedical applications to be measured.

1.4.1. Differential scanning calorimetry (DSC)

The first calorimeter was built by a French Scientist Antoine Lavoisier in 1780 to measure the heat production of a guinea pig[198]. In the last two centuries, calorimetry has come a long way from measurement of heat release/absorption of an animal to micro and nanoscale measurements of cells and macromolecules. Differential Scanning Calorimetry (DSC) is a type of calorimetry that is used to measure the enthalpy, specific heat capacity and latent heat of wide variety of materials with small sample mass (~3 to 100 mg) over wide temperature ranges (-180 ^{0}C to >750 ^{0}C). In the last five decades, it has been widely used for understanding the thermodynamics and kinetics of the phase change of water, protein and lipids in biomolecules as listed in Table 1.6. A typical DSC set-up consists of a furnace loaded with two pans or crucibles. One of these is filled with the sample, while the other is usually empty to subtract background heat flow from the crucible and other artifacts. The DSC measures the difference in heat flow between the sample and the reference pans during heating, cooling or at an isothermal temperature. The resulting differential heat flow, (mW) 'ϕ_{sample}', is plotted as a function of temperature (^{0}C) or time (s). Then, Δh ($\Delta H/m$) and c_p (Cp/m) can be determined using the following equations,

$$\Delta h = \frac{1}{m} \int_{T_1}^{T_2} \frac{d\phi_{sample}}{dt} . \frac{dt}{dT} dT \tag{1.5}$$

$$c_p = \frac{1}{m} \frac{d\phi_{sample}}{dt} . \frac{dt}{dT} \tag{1.6}$$
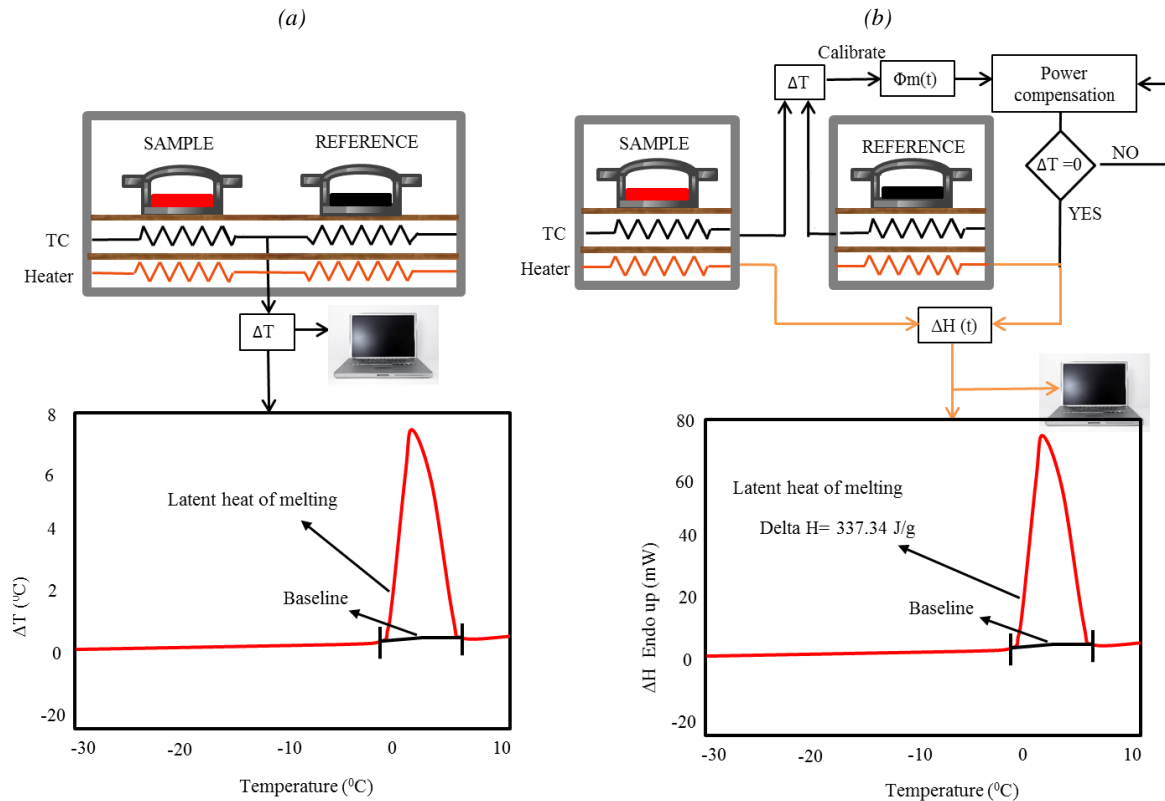
Figure 1.9. Differential Scanning Calorimetry. (a) Schematic of HF DSC. Inset showing a typical DTA thermogram during a first order phase change. (b) PC DSC with a second feedback loop. Inset showing a typical DSC thermogram during a first order phase change.

Based on heating technique, DSC can be divided into two basic types: the standard DSC with linear heating and the modulated DSC with modulated heating. The standard DSC allows the sample and the reference to be heated by a linear temperature program. There are two types of standard DSC: Heat flux DSC (HF DSC) and power compensated DSC. Heat flux DSC was developed by Privalov et al, in 1964[199]. In this type of DSC, the sample and the reference are heated in a single furnace and the temperatures are measured using thermocouples (Fig. 1.9 (a)). Difference in heat release/ absorption between the sample and the reference will result in a difference in temperature between the sample and the reference (ΔT)[200-202]. The main advantage of this type of design is the simplicity of construction. However, the sample and the reference being loaded in the same furnace makes it less accurate (2% vs 0.2% for Power compensated (PC) DSC) for calorimetric measurements and

Table 1.6. Representative measurements in biomolecules using DSC

Type	Sample	Measured Parameters	Size	Max. Scan rate	Rep. Ref
Proteins	Ribonuclease, lysozyme, chymotrypsin, cytochrome c and myoglobin	ΔH, $C_p(T)$, T_m	1.33 mL (conc – 0.05-0.5 %)	1 ^{0}C/min	101
	Proteins in AT-1 cells	$C_p^{ex}(T)$, T_m	40 µL (conc - 76 µg/µL)	50 ^{0}C/min	121, 205
Lipids	Dipalmitoyl phosphatidylcholine (DPPC) liposomes.	$C_p^{ex}(T)$, T_m	NA	10 ^{0}C/min	206
	Fatty tissues	$C_p(T)$, T_m	20 µL	1.3 ^{0}C/min	207

*$C_p(T)$- specific heat capacity, T_m- phase change temperature, ΔH- latent heat during phase change

achieve lower scan rates (<250 ^{0}C/min vs >500 ^{0}C/min than PC DSC). Power compensated DSC was developed by O' Neill et al (Fig. 1.9 (b))[203-204]. This technique has two identical furnaces: one for the sample and the other for reference. Each furnace has a heater and a platinum resistance temperature sensor. The furnaces are made of platinum iridium alloy. The main difference between HF DSC and PC DSC is the control loop. HF DSC supplies equal amounts of heat flow to both the sample and the reference and uses ΔT to determine ϕ_m (ϕ_s-ϕ_r). In contrast, the PF DSC supplies differential heat flow to the sample and the reference such that ΔT becomes 0 ^{0}C. Thus, the differential heat flow, ϕ_m is obtained directly, improving the accuracy and sensitivity.

M-DSC has the capability to simultaneously measure Cp and heat flow from a kinetically controlled process (e.g. phase change)[208]. It uses two simultaneous heating rates: a sinusoidal heating rate modulated over the linear heating rate. The linear component provides information of irreversible heat flow (e.g. crystallization) similar to that of standard DSC, while the modulated component allows the reversible heat flow measurement of the sample (e.g. C_p). One application of M-DSC is to measure specific heat capacity overlapping another kinetic process such as crystallization in a polymer (poly(ethylene terephthalate))[208].

In the past, certain calorimeters were designed to directly measure metabolic heat release in organisms and even cells. For instance, these calorimeters were used to study metabolism in mammalian sperm cells[209-210], T-lymphoma cells[211], blood mononuclear cells[212] and organisms such as Leishmania amazonensis parasites[213], thermotolerant Bacillus[214]. They have similar sensitivity (millijoule) to that of current DSCs.
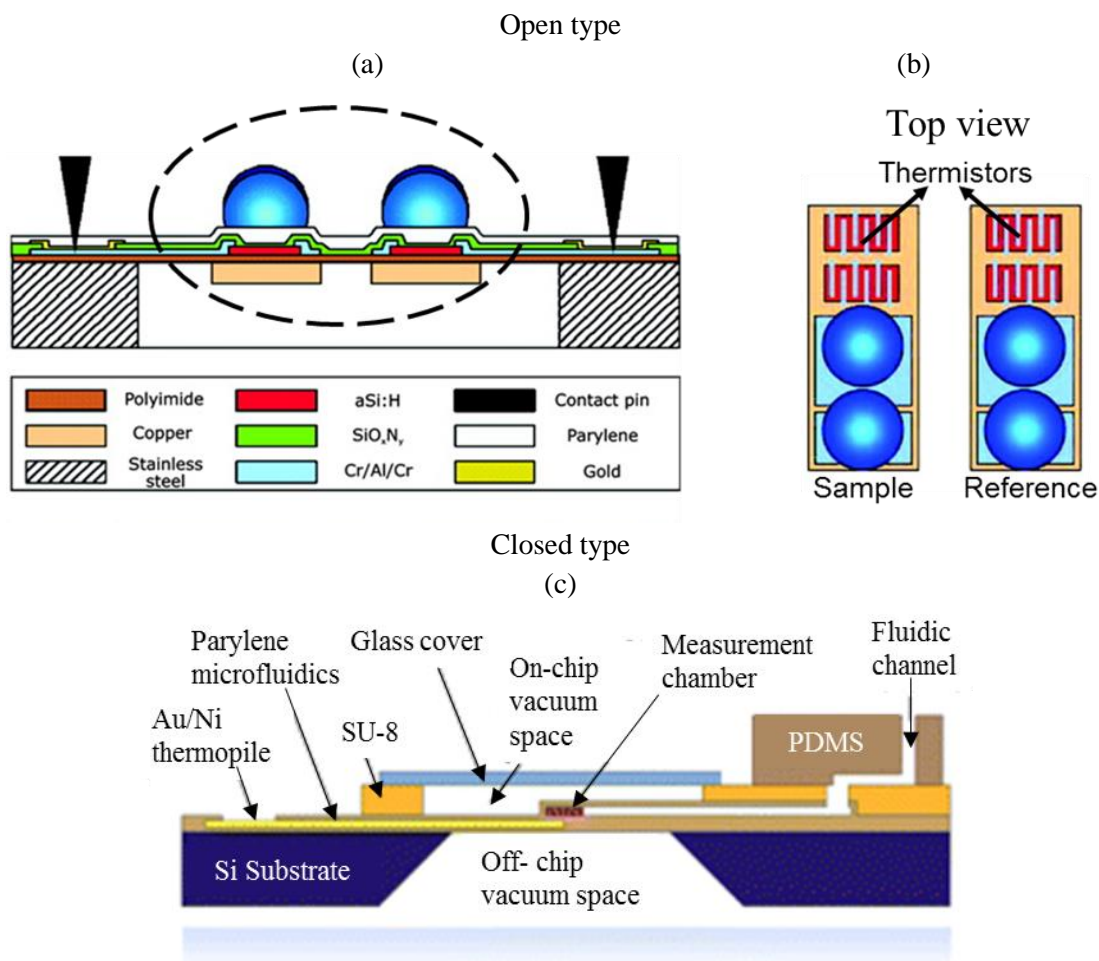
Figure 1.10. Nanocalorimetry. *(a) Cross-sectional schematics of the open type differential nanocalorimeter is shown. (b) Top view of the circled region in (a) is shown. The left side is the sample area and the right side is the reference area. The calorimeter studies the heat of reaction between two liquid materials (i.e. two blue circles on each side) merged using electrostatic merging and mixing mechanism. (c) Device schematic (cross-sectional view) of closed type parylene-polymer-based microfluidic absolute nanocalorimeters. The parylene membrane is suspended and thermally isolated by vacuum. Figures reprinted from [215], [30]. Copyright 2009 and 2004 National academy of Sciences of the United States*

1.4.2. Nanocalorimetry

Nanocalorimetry is a new type of calorimetry that was developed to work with samples that are three orders of magnitude smaller than those with a typical DSC (mass~ ng and down to picoliter volumes). These devices are typically highly responsive (μs- ms), sensitive (~1 nJ/K), and can achieve a high heating rate of ~10^7 ^{0}C/min. These devices allow unprecedented calorimetric measurements for biomaterials if properly protected from evaporation. The basic construction of the device depends on the sample, application and purpose of the experiment. A typical nanocalorimeter is constructed on a thin film silicon-based membrane (as shown in Fig. 1.10(a)). A heater line and a temperature sensor are microfabricated on top of the membrane in a chamber. The heater is excited by an electric current heating the sample, and the resulting temperature is measured by a temperature sensor with a resolution of the order of ~ μK to mK. The heating could be either continuous[14, 30, 65, 215-218] or modulated by an alternating current[219-222]. The sensitivity of this instrument depends on the thermal conductivity (k) and heat capacity (C_p) of the structural body as explained later.

There are several methods to measure temperature in a nanocalorimetric chamber. The most commonly used method is thermopile[65, 223-224]. The thermopile is really several thermocouples connected in series to improve temperature sensitivity (10μK), with the sensitivity being proportional to the number of thermocouples. Thermistors can also be used to measure temperature with similar sensitivity[215, 225]. The thermal time constant of typical thermistors (characteristic length scale ~mm) are, in most cases, approximately several seconds. For calorimetric applications, thermistor time constant have been reduced to <100ms by reducing the characteristic length of the thermistor element to <250 μm[226]. However, they need external electric power for operation. In other words, electric current should be passed through the thermistor to measure change in

33

resistance, which can produce Joule heating and interfere with the existing heat flow in the system[227]. Another commonly used temperature measurement is the resistance thermometer. The principle of operation is same as that of thermistors. However, the advantage is that they have lower resistance than thermistors, resulting in lower Joule heating. Platinum is an example material used for this purpose[228]. Both the resistance thermometer and thermistors need calibration that involve the assignment of temperatures to resistance of temperature sensors. For this purpose, the nanocalorimeters are isolated inside a furnace for several hours to bring the entire system to a steady state temperature while simultaneously measuring the resistance. However, for use at high temperatures (>600 K), the furnace-based calibration results in large thermal gradient within the calorimeter. This gradient can be as large as 40 K, introducing a significant error in calibration. So pyrometers have been used to identify the temperature at the sensor for calibration at high temperatures (573 K to 873 K)[229].

The sample can be fed to the chamber using micro-fluidics or syringe pumps depending on the chamber type. The chamber can be open or closed depending on the application. If the chamber is open, the sample is placed by micropipette or inkjet printing, although this approach suffers from parasitic heat loss and sample evaporation; thus, it is most suitable for solid materials (Table 1.7). If the chamber is closed with a layer on top as shown in Fig. 1.10 (b) (i.e. with PDMS), the sample is supplied by microfluidic channels. However, the added layers of materials comprising these channels increases the thermal mass of the system. Unfortunately, a high thermal mass ($k.C_p$) leads to high thermal time constant, resulting in lower sensitivity. This effect can be minimized by proper selection of materials with minimum heat capacity and thermal conductance. If the thermal mass is increased, the heat flow from the sample is absorbed by the material, thus reducing the sensitivity. Lee et al have developed a nanocalorimeter with a closed chamber using parylene with low thermal mass and vacuum separators to reduce thermal conductance and improve resolution by at least a

34

factor of magnitude compared to other closed type devices[30]. The calorimeter built from parylene

has a time constant of ~1.3 s[30], whereas the one built from higher thermal mass PMMA has a time

constant of ~12 s[65]. In another non biological example, the thermal mass of the nanocalorimeters

have been reduced by an alternate design, where the heaters and thermometers are integrated onto

a suspended beam of SiN_x[230-231] or NbN_x substrate[232] and temperature is measured using a resistance

thermometer[230, 233] or bi-material cantilever[231] (10-50 μK). These calorimeters have achieved an

impressive picowatt resolution (<1 pW) and millisecond time constant (<100 ms)[230-234]. Further,

these calorimeters use modulated heating scheme with high frequencies as they improve signal-

noise ratio by reducing 1/f noise caused by thermal drift[233]. A disadvantage of suspended

nanocalorimeters is their extremely sensitivity to small vibration, which require high vacuum (<10$^-$

^{4} Torr). Further, the sample loading onto these nanocalorimeters is currently only possible by direct

microfabrication of the sample onto the sensor. Thus, while these nanocalorimeters represent state-

of-the art sensitivity, their application to bioengineering problems remain uncertain and untried at

this point. Perhaps with the use of 3D printing and/or cryogenic preparations there will be an

opportunity to use these sensors, similar to previous cryo SEM or cryo TEM preparations, at low

pressures on frozen hydrated samples[235].

Several nanocalorimeters that have been developed in labs or commercially are listed in Table 1.7

Nanocalorimeters have been developed to operate over a wide temperature range (-100^{0}C to 700^0

C). Nanocalorimeters have been constructed to make both absolute[30, 65, 215] and differential heat

measurements[236]. In addition to the list in Table 1.7, Xensor Integration, a manufacturer has been

building nanocalorimeters chips for use at 800 ^{0}C, 1300 ^{0}C and in liquids. In fact, the Mettler Toledo

Flash DSC 1 uses the sensors from Xensor (www.xensor.nl).

1.4.3. Applications for multiscale calorimetric measurements

Nanocalorimeters require very small sample volumes and have fast response and high resolution. Further, they are expected to become even more sensitive with the improvement of their fluid-handling capability and temperature measurement. Currently, they are several major application areas opening up for nanocalorimetry: (a) cryobiology, (b) high-throughput calorimetry for the drug industry, (c) protein conformational studies, (d) label-free biochemical sensing, and (e) monitoring of cells.

i. Cryobiology

For cryopreservation, biomaterials freeze at low temperatures, damaging cells in several ways[9]. Hence, cryoprotective agents (CPAs) are added to biomaterials to avoid freezing the water content. One approach is to use high concentration CPA (>2M) to achieve vitrification at achievable cooling/warming rates (< 100 ^{0}C/min) in clinical settings. However, this approach is highly toxic and hence remains unsuccessful. On the other hand, low concentration CPAs (<2M) are minimally toxic but have been estimated to need ultrarapid cooling (~10^4 ^{0}C/min) and warming rates (> 10^4 ^{0}C/min) for successful vitrification. With recent developments in cryopreservation approaches, ultrarapid cooling rates (~10^4 ^{0}C/min) are achievable in microscale (<100 μm) biomaterials[237-240]. In fact, Jin et al have successfully cryopreserved mouse oocytes by achieving ultrarapid warming rates and CPAs at low molarity (2M)[241]. Further development of successful use of CPAs requires improved understanding and implementation of vitrification and warming in these small systems. One important uncertainty is the crystallization and vitrification behaviour of low concentration CPAs (<2M). For instance, the critical cooling rate – the minimum rate required to achieve vitrification – has never been measured for low concentration CPAs (<2M)[242]. Several estimates are available in literature, often contradicting each other by at least an order of magnitude. Thus,

we need an accurate, quantitative technique that can achieve high heating rates to understand the thermodynamics and kinetics of phase change events of low concentration CPAs. In fact, nanocalorimetry has been used at ultrafast heating rates to study glass transition and crystallization in polymers[71, 243-246], perhaps pointing the way for potential use in cryobiology.

ii. High-throughput calorimetry

An important advantage of nanocalorimeters is the ability to use them in a high throughput mode. This can be useful for quality control in the drug discovery industry, where enthalpy can give insight into ligand binding and the sample availability and measurement times are small. In principle, all nanocalorimeters can be operated in parallel to increase their measurement throughput. The main issue is fluid-handling. As previously mentioned, fluid delivery for open-chamber nanocalorimetry systems can lead to error from evaporation. One solution to this is to use large sample volumes (~250 nL) with electrostatic droplet merging techniques[70, 215]. One such device that does this consists of electrostatic drop merging, magnetic mixing with thermistor sensors, which enable high-throughput heat-of-reaction measurements (96 measurements in parallel) with 250 nL samples. For closed-chamber types, substantial heat loss and inaccuracy of the sample injection volume have been issues. In theory, the system could be multiplexed without much complication, but this has not been attempted as far as we know. However, Lerchner and his co-workers achieved high throughput in closed-type nanocalorimeter using segmented flow construction. In this case, the sample, usually a solid or aggregate, is carried by carrier fluids to the measurement chambers[247]. Interested readers are directed to a detailed review on this topic[248].

iii. Protein conformational studies

In the pharmaceutical industry, proteins are often studied to understand their stability against aggregation during lyophilization, shipping and storage[249-251]. Proteins undergo weak glass

transitions, which are difficult to measure using conventional DSC[252]. Thus, nanocalorimetry is critical in making these measurements with high sensitivity[253-254]. During nanoparticle-based hyperthermia, nanoparticles are often functionalized with protein receptors for increased stability to reach the target[255]. The conformational behavior of proteins attached to nanoparticles has not been extensively studied in the literature[186]. Nanocalorimeters can be particularly advantageous as the small sample volume requirement enables the measurement of a scarce sample, such as proteins produced by the subpopulation of a heterogeneous cell culture. Several groups have demonstrated the use of nanocalorimeters with 10-µg biological samples[228, 256-258]. For instance, Wang et al used a nanocalorimeter with 50 nW sensitivity to measure protein denaturation of small volumes (~1 µl) with proteins such as lysozyme at concentrations of ~3 to 20 mg/ml PBS solution (Fig. 1.11 (a, b)). This technique has also been used to measure hydration and dehydration of lipids which occur at millisecond time scales[67]. Fig. 1.11 (c) shows the heating of dehydrated DPPC for several cycles with the time interval being 300 ms between each cycle. The first cycle shows a peak at ~64.3 ^{0}C, which shows tightly held water release, indicating that it is impossible to achieve a truly dry state. The next cycles do not have a peak at low temperatures, indicating the dry state of lipids.

iv. Biochemical sensing

Nanocalorimeters can be used to sense heat of reaction in enzymes, antibodies, DNA, cells, and many other micro/nanoscale biomaterials. There are several ways to transport the biomolecules to the chamber. A simple technique is to supply both the substrate and the enzyme to the chamber, where they mix by diffusion[217, 259-260]. This method, however, requires rather large amounts of enzyme solution for detection (~10-20µL). Another way to transport a small sample is with microbeads. The enzymes can be immobilized on microbeads and loaded into a chamber or directly deposited in the chamber to detect substrates[216, 225, 261-262]. Similarly, antibodies or DNA can be used

for calorimetric sensing and DNA "thermosequencing"[263]. For instance, Ahmad et al used nanocalorimeters to detect biotin in the sample using a microbead coated with streptavidin receptor (Fig. 1.11 (d))[69]. The binding event produces a heat release enthalpy, ΔH of ~107 kJ/mol biotin (~438 nJ/ng biotin) for a volume flow rate (V) of 20 μL/min with a concentration (C_{biotin}) of 50 μmol/L. The heat rate from the reactions can be calculated as

$$P = V \cdot \Delta H \cdot C_{biotin} \qquad (1.7)$$

For this case, P is ~1.78 μW which is greater than the noise equivalent power (NEP) of the instrument at 20 nW. Owing to low NEP, the instrument can measure extremely small biotin concentrations of 1 μmol/L of phosphate buffer for a flow rate of 20 μL/min as per Eqn. (1.7). Thus, the signal- noise ratio and sensitivity of the thermopile (temperature sensor) largely determines the limit of detection. Further, microbeads also help improve the signal-noise ratio by having a larger surface area and localizing the heat generation in the chamber. This phenomenon increases the heat

Table 1.7. Representative list of nanocalorimeters both commercial and custom built at academic institutions (Reprinted and updated from the reference [243]. Copyright 2012 Wiley.)

Chamber type	Chamber volume (nL)	Sample delivery	Power resolution (nW)	Energy resolution (nJ)	Reference
Closed	3.5	Microfluidics	4.2	10	[30]
Closed	800	Syringe pump	50	5000	[216]
Closed	15	Syringe pump	300	10^5	[43, 217]
Closed	6000	Syringe pump	30	1000	[65]
Open	500	Electrostatic merging	50	750	[215]
Open	0.75	Micropipette	13	100	[218]
Open	0.05	Inkjet head	150	500	[264]
Open	50	Micropipette	22	132	[265]
Open	560 ng	Electrospray	NA	NA	[67]
Open	100 ng- 10 μg	Micropipette	<500	NA	[266] (Mettler Toledo- Flash DSC)

of reaction at the nanocalorimetric sensor above the limit of instrument detection. Thus, nanocalorimeters can provide real-time, label-free sensing for long-term use without sensor element fouling. In comparison, use of open type stagnant droplet arrangements provided limit of detection of 8μmol/L with a smaller sample volume of 250 nL whose noise equivalent power was 50 nW[215].

v. Monitoring of cells

Nanocalorimeters have been used for monitoring the metabolism of various cell types, such as bacteria[68, 267], mammalian cells[268-269] and single zebrafish embryos[65]. The monitoring of cellular metabolic changes as a form of released heat can give an important insight into the dynamics of the underlying biological processes. The microfluidic capability can provide a controllable environment for various cell types, and calorimetric measurement is label-free and nondestructive and can be used with other analysis methods. Such studies have shown the possibility of using nanocalorimeters to monitor the effect of stimuli such as antibiotics[68, 267] and hormones[268-269] on metabolic rate. For instance, Lerchner and his co-workers have investigated the susceptibility of methicillin-resistant Staphylococcus aureus (MRSA) to the use of antibiotic cefotoxin. Fig. 1.11 (e) shows the signal change, which represents the heat flow from the bacteria i.e., metabolism. As the antibiotics are growth inhibitors, the metabolic heat rate decreases if the bacteria is sensitive to the antibiotics. Also, the signal change from the *S. aures* bacteria on exposure to bacteriophage (a virus that infects and kills bacteria) was more than 90% whereas that of E. Coli, which is resistant to bacteriophage, did not change[68]. Thus, nanocalorimeters can be used to study the efficacy of antibiotics and bacteriophages against bacteria. Further, the growth of suspended bacteria[267] and biofilms[270] can also be observed and measured within nanocalorimeters. Thus, the nanocalorimeter has great potential as an analytical tool for measuring cellular metabolism.
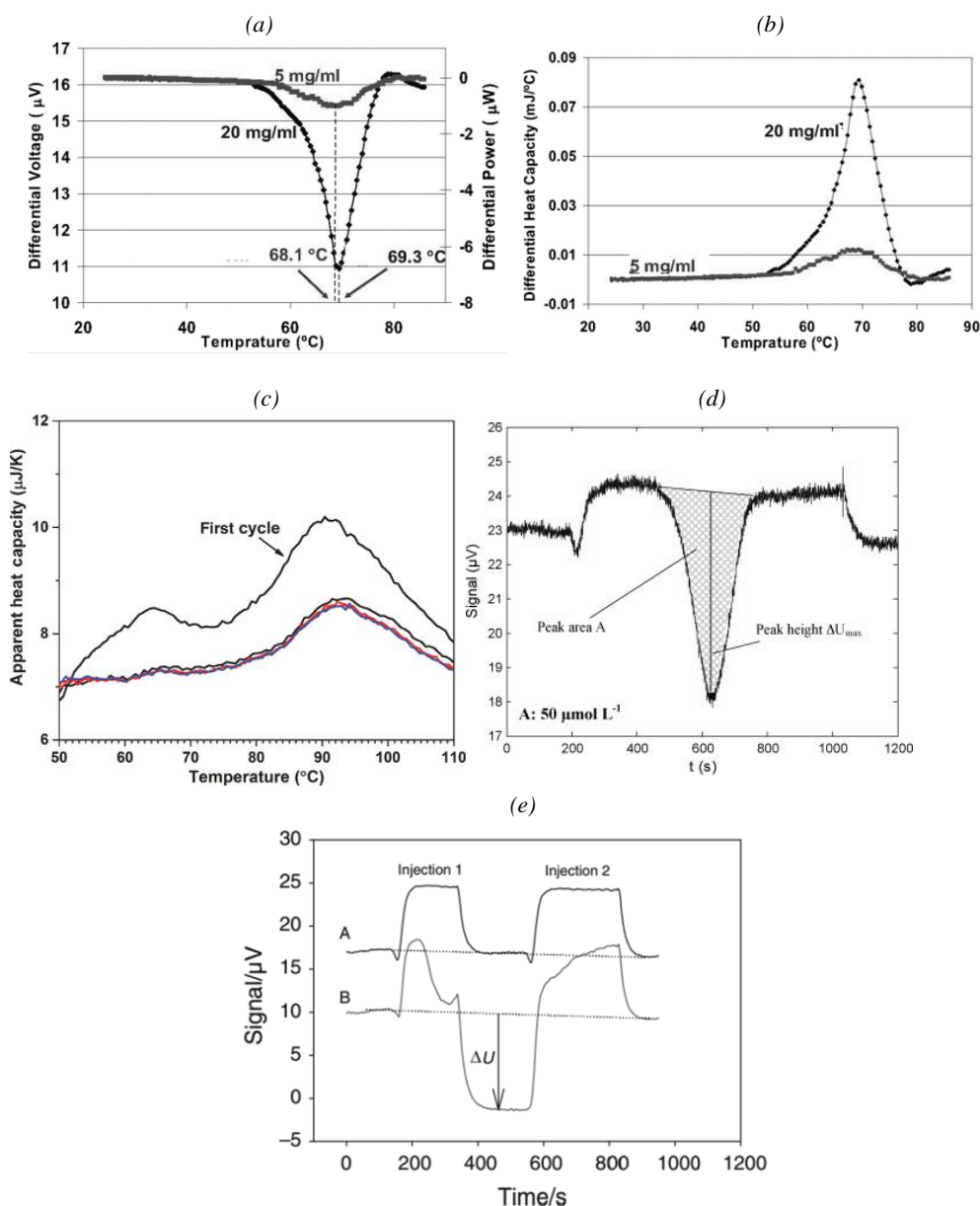
Figure 1.11. Examples of protein and lipid nano-calorimetric measurements. *(a) Denaturation of lysozyme (Concentrations: 20 mg/ml, 5 mg/mL; scanning rate: 5 ⁰C/min); (b) Calculated differential heat capacity versus chamber temperature. (c) Phase transition of DPPC in dry state in dry nitrogen, the interval time between cycles is 300 ms. (d) Peak area and Peak height from measuring binding effects between biotin (concentration - 50 μmolL⁻¹) and streptavidin receptor. (e) Metabolic heat release from a bacterial suspension with typical shapes of signals from zero measurements (A) and those with bacterial suspension (B). The signal shift ΔU is a measure of the metabolic heat rate. Figures reprinted from [236,67,68-69]. Copyright 2014, 2011, 2010, 2006 Wiley, Springer, Elsevier and IEEE*

1.5. Conclusion

Bioheat applications at the nanoscale and microscale are driving the need for thermal conductivity

and calorimetric measurement at new dimensional and temporal scales. In this review, we have

discussed new measurement tools and opportunities to make these measurements. . For instance, we first reviewed several thermal conductivity measurement techniques that can be adopted at multiple scales and thermal regimes. We then focused on calorimetric measurement of biomaterials such as DSC at the microscale (e.g. tissues and millions of cells in media) and nanocalorimetry at the nanoscale (e.g. cells and biomolecules). Together this serves as an overview of measurement of thermal conductivity, latent heat and specific heat in the cryogenic ($<$ -40 °C) and hyperthermic ($>$ 40^{0}C) regimes where water, protein and lipid phase changes occur correlate to injury. In short, these new thermal measurement tools and opportunities serve to increase our understanding and prediction of injury or preservation processes in bioheat transfer applications.

1.6. Specific Acknowledgements

2. *Thermal Properties of Porcine and Human Biological Systems*

This chapter appeared in the following publication:

Phatak, S., Natesan, H., Choi, J., Sweet, R., & Bischof, J. (2017). Thermal Properties of Porcine and Human Biological Systems. Handbook of Thermal Science and Engineering, Kulacki, F. (Eds.), Springer 1-26.

2.1. Introduction

Bioheat transfer, a key component in the field of thermal medicine, has traditionally been important to understand for the purpose of two main areas: thermal therapies and bio- or cryopreservation. Thermal therapy is the application of hot or cold temperatures to destroy undesirable tissues, such as tumors within the body[1, 20]. Cryopreservation is the preservation of biomaterials for a number of applications, such as organ transplantation, in vitro fertilization, and food preservation, through cooling systems to very low temperatures (<-80°C) to arrest biological activity[8]. Cryopreservation can be achieved by slow freezing where addition of cryoprotectants such as glycerol and Dimethyl sulfoxide (DMSO) avoids intracellular ice formation or by fast cooling techniques that result in vitrification or glass formation due to the presence of cryoprotectants. Successful organ banking through cryopreservation would increase the number of possible transplantations; currently 1 in 5 patients die due to lack of an availability of viable organs[5]. More information regarding these applications can be found in the references provided in Table 2.1. More recently, interest in the thermal properties of human tissues has increased for the purpose of the development of predictive models for training and assessment of skills related to thermally related interventions and conditions.

For all applications of bioheat transfer, the temperature excursions of the biomaterials can be correlated to the injury that may occur in the system[271]. Thus, thermal modeling is necessary to predict the thermal history and hence the injury, since it may not be always possible to measure temperature experimentally. Hence, analytical or numerical models become valuable in order to study the process. In cryopreservation, knowledge about thermal history and cooling rates will help in understanding the phases through which a particular system passes, i.e. liquid, crystal and glassy/vitreous states. The cooling and heating rates encountered in these systems can help define whether a system will pass through these various phases. Temperature gradients experienced due to fast cooling required for vitrification also affect stress development in the sample and can cause cracking. For more information on these topics, please see [10, 14, 272]. In the case of cryosurgery, thermal history again would be an indicator of destruction of the tissue or tumor in the biological system. Mechanisms believed to cause damage include direct cell injury, vascular injury and immunological injury. These injuries depend upon the cooling and thawing rates, the minimum end temperatures and the hold times at these temperatures. As an example, tumor destruction is associated with a minimum lethal temperature. A heat transfer model can help understand these temperature distributions and cooling and heating rates, so as to correlate with actual experimental results[273-274]. The interested reader is directed to [18-19, 275] for more details regarding the injury mechanisms associated with cryosurgery. During thermal therapy, heating results in water loss and protein denaturation. These events lead to reduction in the thermal conductivity and specific heat capacity of the system of interest. Thus, temperature dependent thermal properties are needed when used in a model, as these directly will affect the thermal histories. For more information regarding the effects of higher temperatures on thermal properties, please refer to [276].

Heat transfer in biological systems is a complex process influenced by a variety of mechanisms: for example, conduction within tissues; convection as well as perfusion due to blood circulation;

Table 2.1. Overview of common bioheat transfer applications

	Application	Temperature	Definition	Rep. ref.[*]
Biopreservation	Vitrification	<-140 °C	Preservation by attaining a glassy state	10-11
	Freezing	<-20 °C	Preservation by freezing in presence of cryoprotectants	9, 23, 26, 278
	Lyophilization/ Freeze Drying	<-20 °C	Preservation by drying after freezing	12-13, 26
	Hypothermic preservation	0 to 37 °C	Preservation at temperatures between 0 °C and 37 °C	16-17, 35
Biodestruction	Cryotherapy/ Cryoablation	<-20 °C	Destruction of tissue by freezing	18-19
	Mild hyperthermia	37 to 45 °C	As an adjuvant to sensitize tumors to radiation and chemotherapy	20, 42
	Thermal ablation	>50 °C	Destruction of tissue by heating	21, 279

*Representative reference. Table 2.1 has been reproduced from [279].

metabolic heat generation; heat exchange between different blood vessels and also thermoregulation effects including shivering; and vasodilation. An example is the classic Pennes' Bioheat Equation[39, 277],

$$\rho C_p \frac{\partial T}{\partial t} = \frac{\partial}{\partial x}\left(k \frac{\partial T}{\partial x}\right) + \dot{q}_m + \dot{q}_p \tag{2.1}$$

where $\rho, C_p, T, k \ and \ \dot{q}_m$ are the tissue density, specific heat capacity, temperature, thermal conductivity and metabolic heat generation per unit volume. Energy exchange between blood and tissue is denoted by the perfusion term $\dot{q}_p$ given as follows,

$$\dot{q}_p = \omega \rho_b C_{pb}(T_a - T) \tag{2.2}$$

45
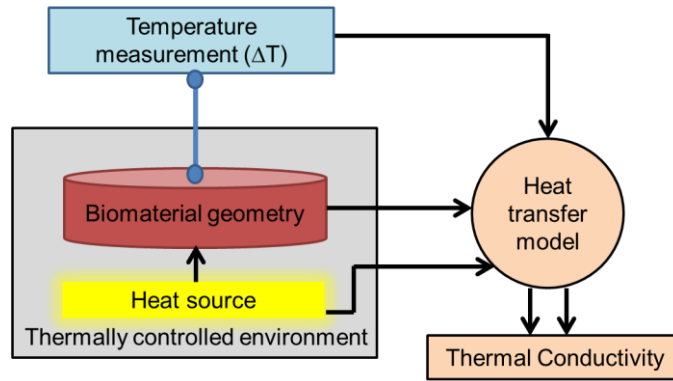
Figure 2.1. Schematic of most thermal conductivity measurement techniques. *Figure 2.1 has been reproduced from [15]. Copyright 2018 Wiley .*

where ρ_b and C_{pb} are blood density and specific heat capacity respectively, ω is the perfusion rate and T_a is the arterial blood temperature. As seen in the Pennes equation, the tissue thermal properties (i.e. density, specific heat capacity and thermal conductivity) need to be determined in order to obtain the thermal history of the system for the above-mentioned applications. In addition to Pennes equation, many other models have been formulated to study these processes. In order to formulate these heat transfer models, readers may refer to [280-282].

2.2. Thermal Properties

Thermal properties focused in this chapter include thermal conductivity and specific heat capacity. Following are brief discussions on their measurement techniques:

2.2.1. Thermal conductivity measurement

Thermal conductivity (k, W/m-K) is a material property, a measurement of its ability to conduct heat. It is influenced by composition (i.e. water, lipid, proteins, and added cryoprotectants), phase (i.e. liquid, crystalline and amorphous phases), and temperature. Some methods used to measure thermal conductivity of biomaterials have been given in Table 2.2. These measurements use either a known heat flux or a known temperature gradient as depicted in the Fig. 2.1. Thermal conductivity measurement techniques can be divided into two types: steady state and transient methods.

Table 2.2. Overview of 'k' measurement techniques

Technique	Heat Source	Temperature Measurement	Heat Transfer Model	Directionality	Rep. Ref.
Guarded Hot Plate Method	Thermal	Thermocouple (TC)	Steady state 1-D Longitudinal	Cross-plane	22
Thermal Comparator	Thermal	Probe (Effective TC)	Transient 1-D Cylindrical	Not sensitive	27-28
Radial Heat Flow Method	Thermal	Thermocouple (TC)	Steady state 1-D Cylindrical	In-plane	25
Heated Thermocouple Method	Electrical	Thermocouple (TC)	Transient 1-D Spherical	Not sensitive	29
Transient Hot Wire Method	Electrical	Thermocouple (TC)	Transient 1-D Cylindrical	Not sensitive	31
Chato's Probe	Electrical	Thermocouple (TC)	Transient 1-D Spherical	Not sensitive	37
Pulse Decay	Electrical (Single Pulse)	Thermocouple (TC)	Transient 1-D Spherical	Not sensitive	40-41, 283
3ω	Electrical	3rd Harmonic Voltage Response	Quasisteady 1-D Cylindrical	Radial (bulk samples); cross-plane (thin films)	45, 47

Table 2.2 has been reproduced from [15]. Copyright 2016 World Scientific

In the case of steady state methods, information about heat flux and temperature response from the sample is used in a heat transfer model in order to calculate thermal conductivity. Some drawbacks of these methods include long times (~ several hours depending on sample size) are needed to reach steady state and a proper "guarding" is needed to prevent heat losses, thus leading to a need for a 1-D heat transfer model. Another problem with these methods is that of contact resistance between the sample and energy source.
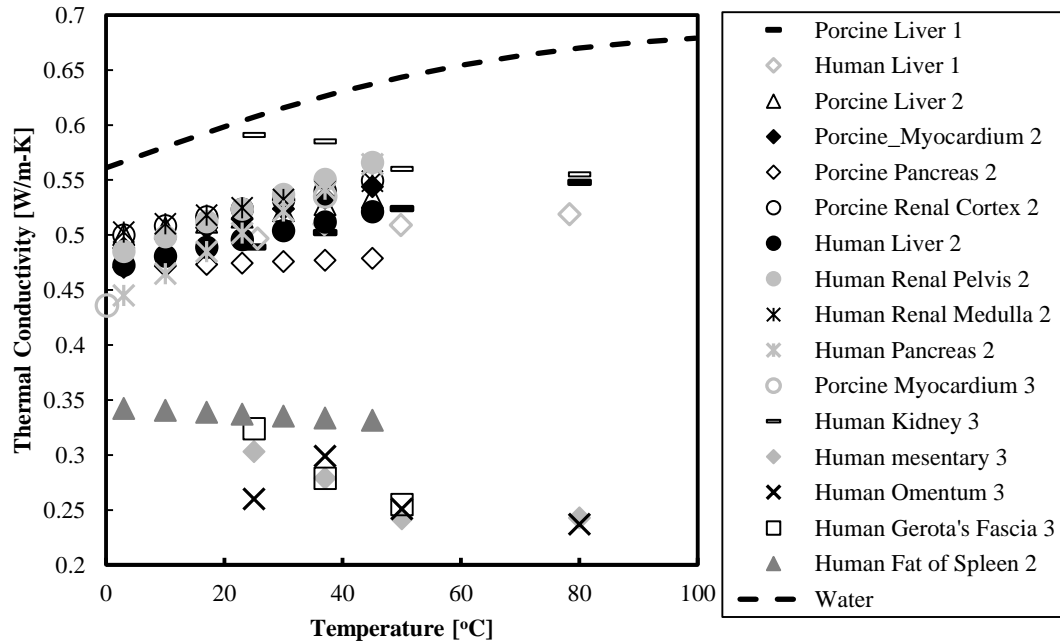
Figure 2.2. Thermal conductivity datasets in the suprazero range. *'1' refers to* [43], *'2' refers to* [41] *and '3' refers to Choi et al., unpublished listed in Tables 2.6, 2.7 and 2.8*

As compared to steady state techniques, transient methods can be performed quickly (< 1 minute). For these methods, a cylindrical or spherical probe can be inserted into the sample to supply heat as well as measure temperature simultaneously. Although faster than steady state methods, these techniques also suffer from the problem of contact resistance between the sample and probe. The heat flow thus needs to penetrate deeper into the sample leading to negligible contact resistance at long time scales of heating. This necessitates a size requirement of >10 mm thus restricting these techniques for use in thick samples. Also, being invasive, they may cause tissue damage.

Lastly, a recent method used for thermal conductivity is the 3ω method which belongs to a third category called as a "quasi-steady" technique. In this case a thin gold heater line is micro-fabricated on to a glass substrate. The measurement times for this method are in the range of tens of minutes and can handle sample sizes in the range 0.1 mm to 2 mm. These methods have been reviewed previously in the following references: [14, 284]
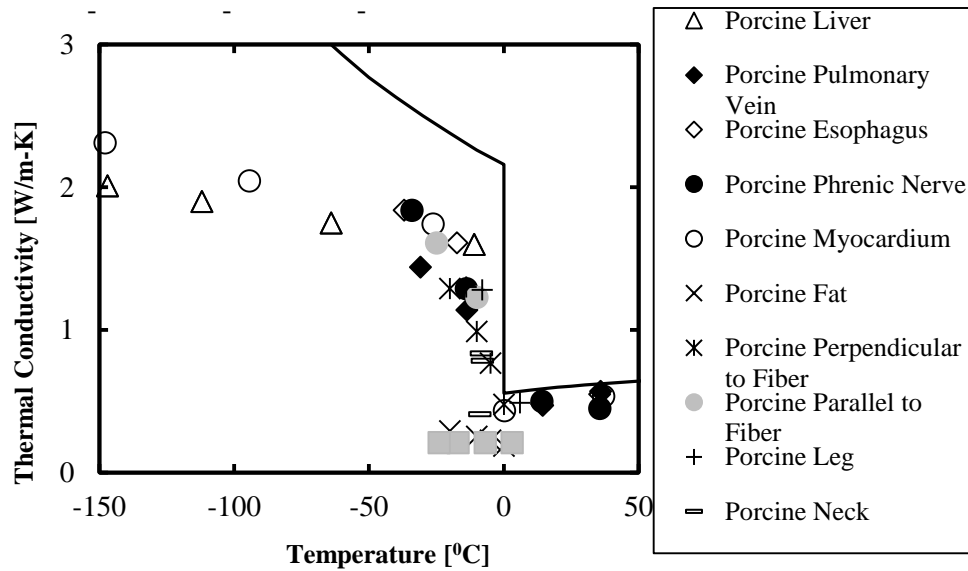
Figure 2.3. Thermal conductivity datasets in the sub-zero and cryogenic range (datasets have been listed in Tables 2.4 and 2.5).

2.2.2. Specific heat capacity measurement

Specific heat capacity (Cp, J/g-°C) is a material property that denotes the amount of heat that should be transferred to a material to raise its temperature by unit temperature (e.g. degree Celsius). In the case of biomaterials, it is important to measure their Cp as a function of temperature. For example, in a wide temperature range (say -150 °C to 20 °C), cryoprotectants pass through different states, such as liquid, ice and vitrified (amorphous), with each of these phases having a different Cp, thus necessitating temperature dependent properties. The most common technique used to measure Cp is differential scanning calorimetry (DSC). DSC is capable of measuring Cp as well as latent heat of relatively small sample sizes (~3-100 mg) over a wide temperature range of -180°C to 750°C[279]. The technique measures the difference in the heat flow rate to the sample and reference pans while maintaining the same temperature program[285]. The reference sample has known thermal properties. This difference in heat flow can then be plotted as function of temperature or time. Using this measured differential heat flow($\emptyset_{sample}$) , the Cp can then be calculated as follows:

$$C_p = \frac{1}{m}\frac{d\emptyset_{sample}}{dt} \cdot \frac{dt}{dT} \qquad (2.3)$$

In terms of the heating technique used, there are two types of conventional DSC viz. standard DSC with linear heating and modulated DSC (M-DSC) with modulated heating. In the case of standard DSC, the sample and reference are heated through a linear temperature program. There are two types of standard DSC viz. the heat flux (HF) DSC and the power compensated (PC) DSC. The HF DSC consists of a single furnace area in which the sample and reference pans are loaded and temperatures measured with thermocouples. The temperature difference between the sample and reference pans is then used to calculate the differential heat flow. For a PC DSC, there are two separate furnaces wherein the sample and reference pans are loaded separately. The principle of this DSC, as well as its differentiator from the HF DSC, is that the temperature difference between sample and reference pans is kept zero by increasing or decreasing the heat flow to the sample in the event of a transition (e.g. phase change from water to ice) in the sample. For reliable
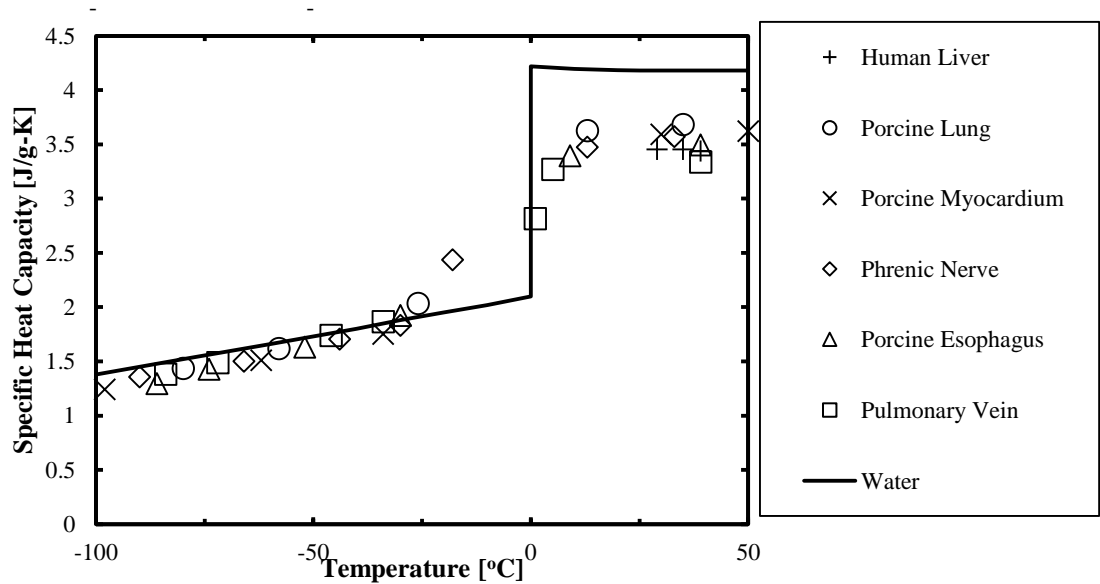
Figure 2.4. Specific heat capacity for biomaterials without cryoprotectants. (datasets have been listed in tables. 2.4, 2.5, and 2.6).

measurements, it is necessary to calibrate the DSC, which usually consists of three steps: baseline calibration (accounts for instrument discrepancies); temperature calibration (considers differences between measured and actual values of transition temperatures); and heat flow calibration (calculates a factor to correct differences between measured and actual heat flow rates). In the case of M-DSC, two simultaneous heating rates are used, i.e. a sinusoidal heating rate along with a linear heating rate. This DSC is capable of simultaneously measuring both the Cp of the sample as well as kinetic processes such as phase change[208, 286-287]. The linear rate provides information similar to the standard DSC whereas the sinusoidal rate is useful for measuring the Cp of the sample. The limitation of conventional DSC is the comparatively low scanning rates (<750°C/min) associated with it. For example, while studying vitrification (glass formation) of dilute cryoprotectants, a very high cooling rate is needed to vitrify the system without causing crystallization, and this cannot be attained in a conventional DSC. This limitation can be addressed by the development of
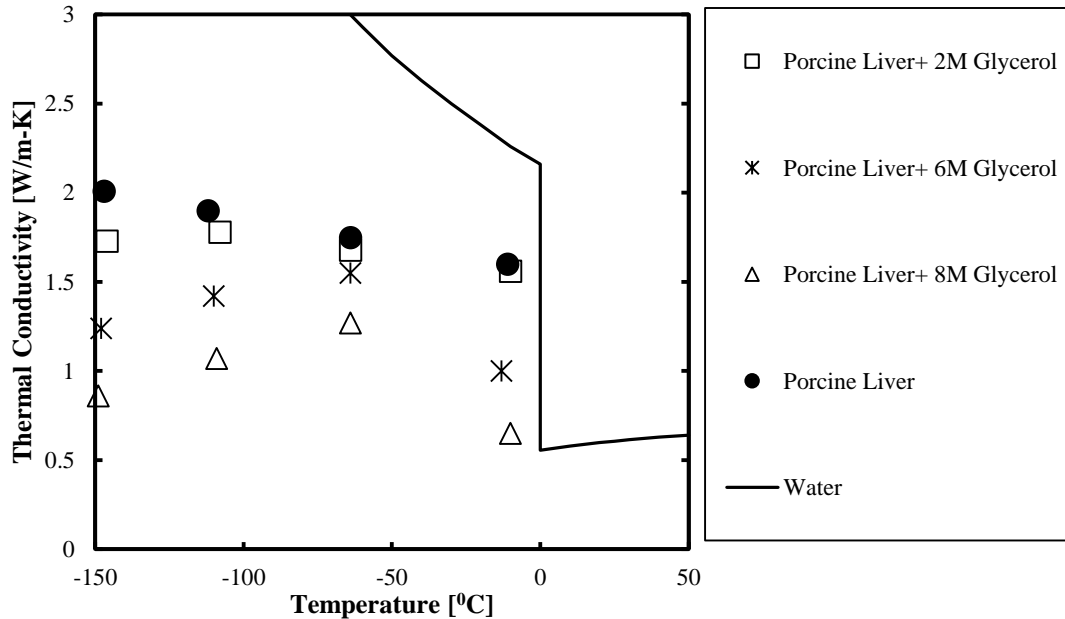
Figure 2.5. Thermal conductivity datasets for porcine liver with and without cryoprotectants. (datasets have been listed in tables 2.5 and 2.10). This figure has been reproduced from [62]. Copyright 2010 Elsevier

51

nanocalorimetry[67] on a silicon-based membrane that can work with a very small sample weight (~ 10 ng), which leads to the possibility of very high heating or cooling rates (~10^7 °C/min).

2.3 Factors That Affect Thermal Property Values

The focus of this chapter is on organizing literature data for thermal conductivity and specific heat capacity of human and porcine systems in the cryogenic, subzero and suprazero temperature ranges. All the data provided here has resulted from actual measurements presented in primary research papers. Apart from primary papers, there are some databases available such as the one by IT'IS Foundation associated with ETH Zurich[288]. In addition there are reviews on this topic such as[73, 289-290]. Blood perfusion results have not been taken into account in the data presented in this chapter. The interested reader may refer to[31, 284, 291-293] for details regarding perfusion associated measurements. Some factors that influence the thermal properties of biomaterials are discussed below:

2.3.1. High temperature effects (37 °C – 100 °C): Protein phase change and water loss

In the case of high temperatures, the values of thermal properties generally rise from 0 °C up to
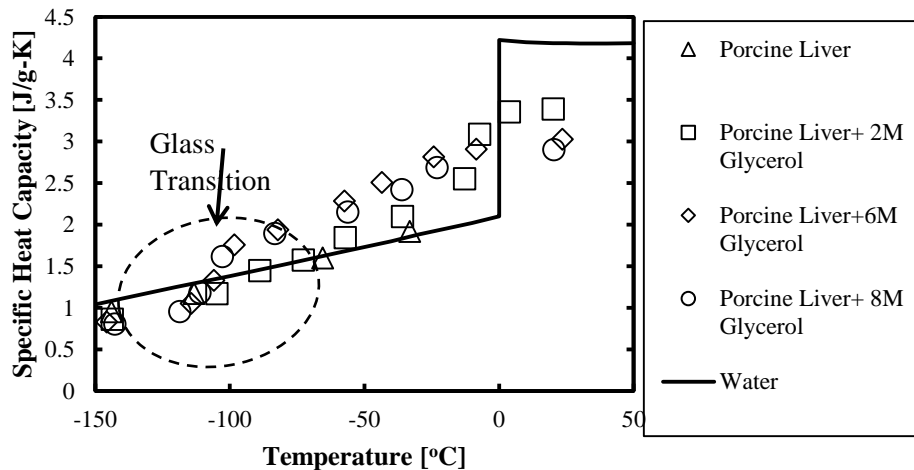
Figure 2.6. Specific heat capacity for porcine liver with and without cryoprotectants. (datasets have been listed in tables 2.5 and 2.10). This figure has been reproduced from [62]. Copyright Elsevier 2010

roughly 45 °C where protein denaturation and water loss can play a role. After 45 °C there is much

less data, although it would appear that water loss plays a more prominent role as compared to protein denaturation resulting in lower values of 'k' and 'Cp'. This drop in thermal conductivity can be seen in Fig. 2.2 above for human kidney, mesentery, omentum and gerota's fascia. The lower 'k' values for mesentery, gerota's fascia, omentum are due to a higher fat content in these systems. Similarly, human fat of spleen also exhibits lower 'k' values due to the presence of fat in the system. Protein denaturation occurs as a heat absorption event over a finite temperature range. The interested reader can refer to [31, 43, 294] for more details regarding these high temperature effects.

2.3.2. Low temperature effects (37 °C – -196 °C): Water phase change and cryoprotectant effects

Thermal properties of biomaterials at low temperatures are affected by two factors: phase change (water to ice) and the presence of cryoprotectants. Freezing or crystallization of water to ice results in an increase in thermal conductivity values at subzero temperatures as ice has a higher thermal conductivity compared to water. This general trend of increasing values of thermal conductivity can be observed in Fig. 2.3 above for various biomaterials. In contrast, specific heat capacity values
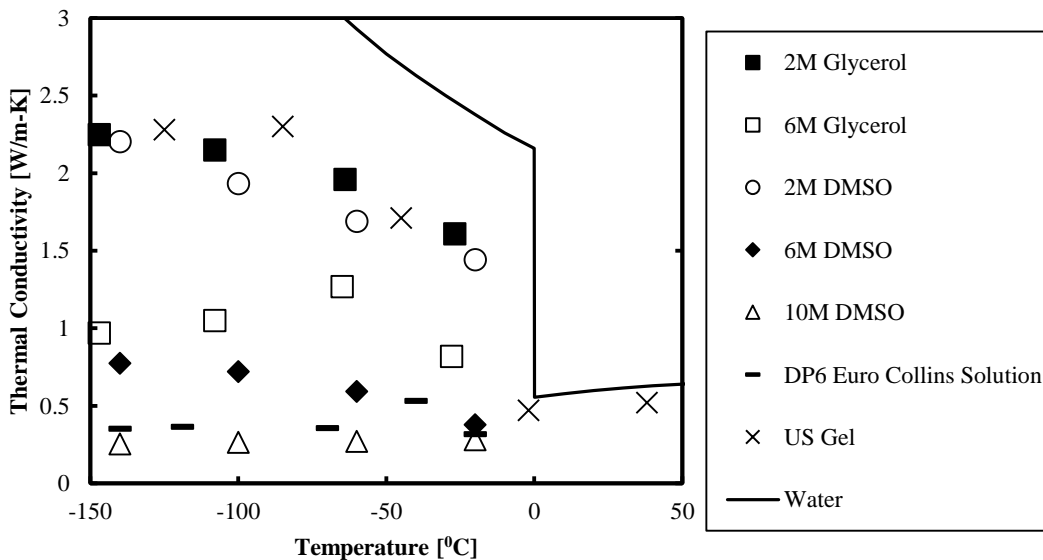
Figure 2.7. Thermal conductivity datasets for cryoprotectants *(datasets have been listed in table. 2.9)*

53

show lower values at subzero temperatures as ice has a lower specific heat capacity when compared to water. This general trend of decreasing values of specific heat capacity for various biomaterials can be observed in Fig. 2.4 below. The values of both thermal conductivity and specific heat capacity of most biomaterials are lower than those of water. The amount by which these values differ with respect to water depends upon the water content in these systems.

In addition to freezing effects, thermal properties of biomaterials are also affected by the presence of cryoprotectants. At lower temperatures (< -100°C), the systems experience glass transition, i.e. formation of a glassy or vitreous state due to cryoprotectants. Both thermal conductivity and specific heat capacity values are lowered due to this glass formation in the system. As seen in Fig. 2.5, thermal conductivity values for porcine liver treated with various concentrations of glycerol are lower as compared to porcine liver without any glycerol and continue to drop with higher concentrations of glycerol. The freezing or crystallization effects which tend to increase thermal
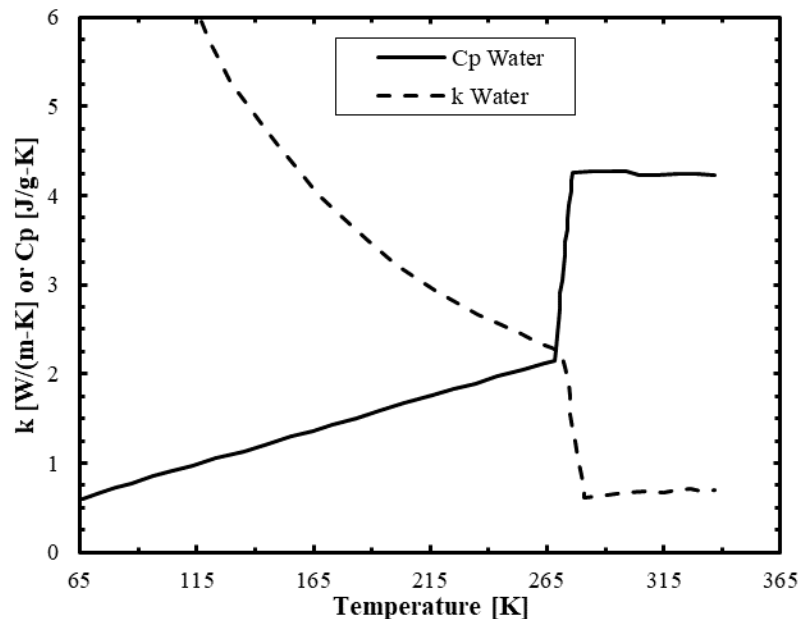
Figure 2.8. Thermal properties of water used for modeling case study*. This figure has been reproduced from [295] Copyright 2002 Association of Mechanical Engineers.*

conductivity are suppressed at lower temperatures in the presence of cryoprotectants which results in these lower thermal conductivity values.

In the case of specific heat capacity, as mentioned above, the values drop in the presence of cryoprotectants (-150 °C to -100 °C) due to the formation of the glassy or vitreous phase. Further, glass transition effects can be seen as a slight jump in the specific heat capacity values around -100 °C in Fig. 2.6. This jump results from the conversion of the glassy phase to a liquid phase. Beyond glass transition, the rise in values at higher temperatures is initially due to conversion of the glassy phase to a liquid phase as mentioned above and later due to melting of the ice present in the system to water knowing that the specific heat capacity of water is greater than ice as well as the glassy phase. Fig. 2.7 below consists of thermal conductivity datasets for a number of cryoprotectants that can be useful when performing heat transfer simulations for cryopreservation. In addition, data has also been provided for Ultra Sound Gel (US Gel) which can be used as tissue phantom in the absence of property data for the required biomaterial.
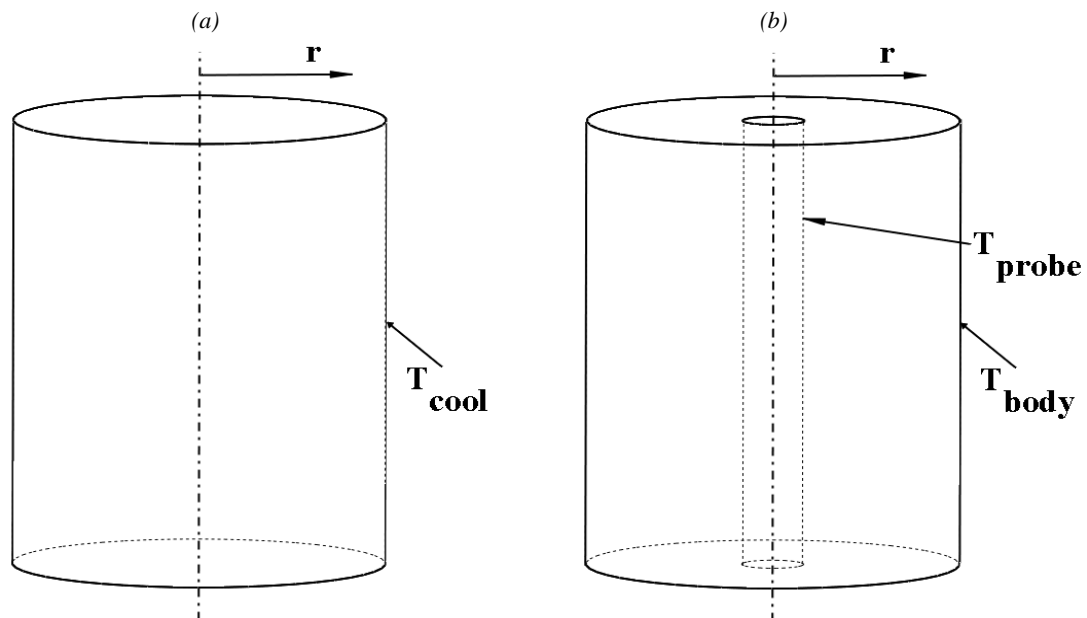
Figure 2.9. Geometry in cylindrical co-ordinates for (a) cryopreservation, (b) cryosurgery *Figure 2.9 has been reproduced from [295]. Copyright 2002 Association of Mechanical Engineers*

The general trends seen in Fig. 2.7 are same as those observed in the case of porcine liver treated with glycerol in Fig. 2.5. The thermal conductivity values increase at lower temperatures due to ice formation whereas the presence of the glassy phase due to cryoprotectants at temperatures < -100 °C results in lower or constant thermal conductivity values. Also, as the concentration of cryoprotectants increases, the thermal conductivity values are lowered as the ice formation is suppressed by the glassy phase. These trends can be seen in Fig. 2.7 for DMSO and glycerol. The interested reader is directed to [36, 44, 81] for more discussion regarding low temperature and cryoprotectants related 'k' and 'Cp' measurements.

2.4. Modeling Case Study

This section provides an example from [295] showing the importance of temperature dependent properties for numerical predictions of heat transfer applied for cryopreservation and cryosurgery. A numerical technique known as the Enthalpy method has been used to solve the heat transfer with phase change problem for cryopreservation and cryosurgery. The governing equation for this method[296] is given as follows:
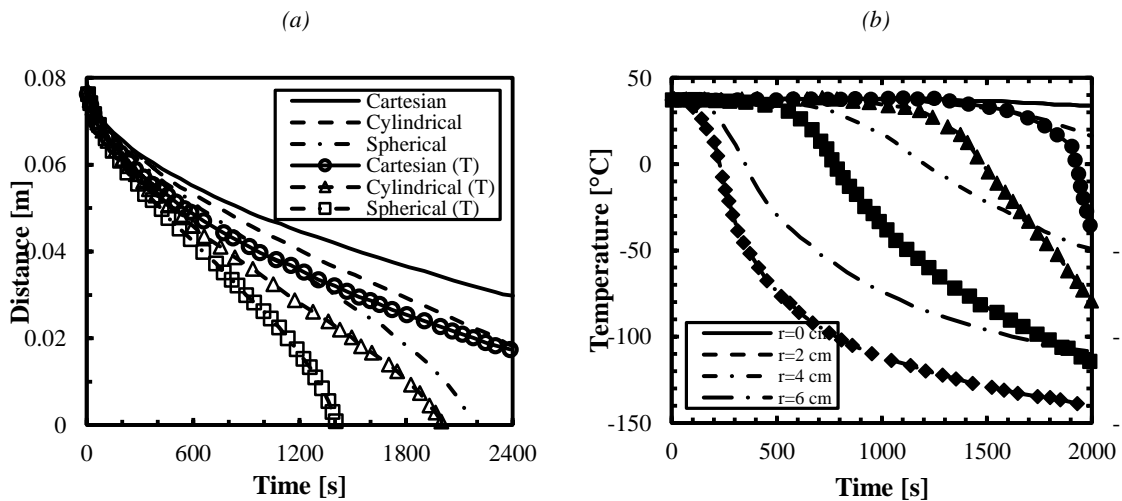
Figure 2.10. Numerical simulation for cryopreservation. (a) Phase front propagation (Lines with symbols denote temperature dependent properties) (b) Thermal history for a cylinder (Lines with symbols denote temperature dependent properties). Figures 2.10 (a) & b have been reproduced from [295]. Copyright 2002 Association of Mechanical Enigneers

56

Table 2.3. Organization of thermal property datasets

Table Number	Description
4 & 5	Porcine Systems at subzero temperatures I and II
6	Porcine Systems at suprazero temperatures
7 & 8	Human Systems at suprazero temperatures I and II
9	Cryoprotectants
10	Porcine liver treated with cryoprotectants

$$\rho \frac{\partial H(T)}{\partial t} = \nabla \cdot (k \nabla T) + g(T) \qquad (2.4)$$

where $\rho, H, T, t, k \ and \ g(T)$ are density, enthalpy, temperature, time, thermal conductivity and heat generation per unit volume.

Eqn. (2.4) is a modified version of the transient heat equation where enthalpy and temperature are dependent variables. In other techniques used for solving phase change, such as source tracking method, two equations are needed to solve for the frozen and unfrozen region. In addition, an energy balance equation is included to track the interface between these two regions. The advantage of the enthalpy method over such methods is that a single equation in terms of enthalpy is used to solve for both regions and thus no tracking equation is needed. In the case of pure materials like water, phase change happens at a single temperature whereas for biomaterials, phase change occurs over a temperature range called a mushy zone. The enthalpy method can be used to solve for both these materials.

For information regarding this method and its applicability to cryosurgery and cryopreservation, readers may refer to [14, 274, 297]. Constant as well as temperature dependent thermal properties of water have been used in these analyses.

The thermal properties of water used in this analysis are provided in Fig. 2.8[298]. As shown in Fig. 2.9, an important distinction between cryopreservation and cryosurgery is that they have opposite boundary conditions, i.e. cryopreservation involves cooling from outside to the center of the system where a symmetric boundary condition can be applied; whereas cryosurgery involves freezing from the center with a probe to the surface where a temperature boundary condition (human body temperature) is applied.

Cryopreservation involves cooling the system to temperatures < -80°C whereas cryosurgery freezes the system to a particular size so that unwanted tissue is killed. Following are the figures showing temperature history and phase front propagation for both applications. Each application considers a planar, cylindrical and spherical system for a thickness or diameter of 8 cm. For cryopreservation, an initial condition of body temperature (37 °C) is considered over the solution domain. A temperature boundary condition of -160°C is applied at the surface with a symmetric boundary condition at the center. As seen in Fig. 2.10, the phase front propagation is the fastest for the sphere and lowest for the Cartesian system. Further, the temperature dependent boundary conditions speed up the ice-zone propagation, which in turn affects the temperature history as shown below.
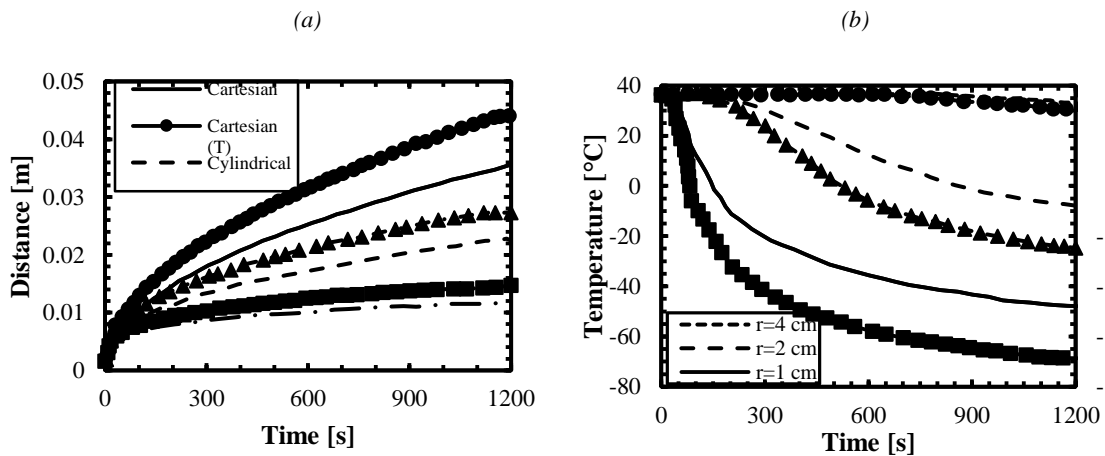
Figure 2.11. Numerical simulation for cryosurgery (a) Phase front propagation (lines with symbols denote temperature dependent properties) (b) Thermal history for a cylinder (lines with symbols denote temperature dependent properties). Figures 11 (a) & b have been reproduced from [295]. Copyright 2002 Association of Mechanical Engineers

In the case of cryosurgery, a temperature boundary condition of -160°C (applied by a cryoprobe) is considered at a radius of 1.5 mm for the radial systems or at one of the surfaces (0 mm) for the Cartesian system. The second boundary condition considers a domain large enough to assume semi-infinite conditions (assuming the system is at body temperature). The same thermal properties as cryopreservation are used in this analysis. As seen from the results in Fig. 2.11, the phase front propagates fastest for the Cartesian system and slowest for the sphere. As seen before, this propagation is faster when temperature dependent properties are used. The interested reader may refer to [295] for more information regarding this analysis.

Table 2.4. Thermal properties of porcine systems at sub-zero temperatures- i

System Type	Thermal Conductivity [W/mK]	Specific Heat Capacity [J/gK]	Reference
Pulmonary Vein	0.57(35.9°C)	3.34(39°C)	'k'— [103] 'Cp'— Unpublished, BHMT, UMN
	0.47(14.42°C)	3.27(5°C)	
	1.14(-13.77°C)	2.82(1°C)	
	1.44(-30.9°C)	1.87(-34°C)	
	—	1.74(-46°C)	
	—	1.49(-72°C)	
	—	1.38(-84°C)	
Esophagus	0.55(35.58°C)	3.49(39°C)	
	0.48(13.99°C)	3.39(9°C)	
	1.61(-17.43°C)	1.92(-30°C)	
	1.84(-36.95°C)	1.63(-52°C)	
	—	1.43(-74°C)	
	—	1.29(-86°C)	
Phrenic Nerve	0.45(35.53°C)	3.57(33°C)	
	0.5(14.01°C)	3.47(13°C)	
	1.29(-14.01°C)	2.44(-18°C)	
	1.84(-34.18°C)	1.83(-30°C)	
	—	1.7(-44°C)	
	—	1.5(-66°C)	
	—	1.35(-90°C)	

BHMT, UMN: Bioheat & Mass Transfer Lab, University of Minnesota
n: Number of repetitions

2.5. Thermal Properties Dataset Tables

Table 2.3 gives a summary of the organization of datasets for porcine and human systems. These

dataset tables 2.4-2.10 have been classified based on the type of system; i.e. porcine or human, the

Table 2.5. Thermal properties of porcine systems at sub-zero temperatures- ii

System Type	Thermal Conductivity [W/mK]	Specific Heat Capacity [J/gK]	Reference
Liver	1.6(-11°C)	1.92(-33.3°C)	62
	1.75(-64°C)	1.6(-65.6°C)	
	1.9(-112°C)	1.171(-113.3°C)	
	2.01(-147°C)	0.95(-144°C)	
Lung	—	3.68(35°C)	Unpublished, BHMT, UMN
	—	3.62(13°C)	
	—	2.04(-26°C)	
	—	1.62(-58°C)	
	—	1.44(-80°C)	
Myocardium (n =3 for 'k', n=8 for 'Cp')	0.5352(37°C)	3.62(50°C)	Unpublished, BHMT, UMN
	0.436(0.1°C)	3.59(30°C)	
	1.743(-26.25°C)	1.75(-34°C)	
	2.046(-94.45°C)	1.508(-62°C)	
	2.312(-147.9°C)	1.241(-98°C)	
Lean, parallel to fiber	1.43(-10°C)	—	299
	1.61(-25°C)	—	
	1.23(-10°C)	—	
	1.38(-25°C)	—	
Lean, perpendicular to fiber	0.478(0°C)	—	300
	0.767(-5°C)	—	
	0.99(-10°C)	—	
	1.29(-20°C)	—	
Lean, neck	0.783(-8°C)	—	37
	0.835(-8.4°C)	—	
	0.408(-9°C)	—	
Leg	0.49(6°C)	—	22
	1.28(-8°C)	—	
	1.3(-14°C)	—	
Fat	0.186(0°C)	—	{Cherneeva, 1956 #145}
	0.227(-5°C)	—	
	0.254(-10°C)	—	
	0.291(-20°C)	—	
Fat	0.36(-9.1°C)	—	37
	0.366(-10°C)	—	301
Exterior (93 % Fat)	0.21(+3 to -24°C)	—	299

BHMT, UMN: Bioheat & Mass Transfer Lab, University of Minnesota
n: Number of repetitions

temperature range considered; i.e. subzero or suprazero, thermal properties of cryoprotectants and effect of cryoprotectants on porcine liver.

For porcine liver in Table 2.6 from [43], specific heat data between 31°C-85°C is not directly added as there is an endothermic heat release associated with protein denaturation in that range. The specific heat capacity available in that range is apparent specific heat and not sensible specific heat capacity. The interested reader may refer to [43] for more details. The thermal conductivity measurements for porcine and human systems from [41] were carried out at temperatures 3, 10, 17, 23, 37 and 45 °C. Linear regression fit constants were provided to be used in the following formula to calculate thermal conductivity:

$$k = k_0 + k_1 T \qquad (2.5)$$

Where $k_0 \left[\frac{W}{mK}\right]$ and $k_1 \left[\frac{W}{mK^2}\right]$ are regression fit constants and T is the temperature in °C.

Thermal conductivity values have been calculated using the above formula for temperatures 10, 23, 37 and 45 °C.

Table 2.6 Thermal properties of porcine systems at supra-zero temperatures

System Type	Thermal Conductivity [W/mK]	Specific Heat Capacity [J/gK]	Reference
Liver	0.5061(10°C)	—	41
	0.5165(23°C)	—	
	0.5277(37°C)	—	
	0.5341(45°C)	—	
Lung	0.2561(10°C)	—	
	0.2849(23°C)	—	
	0.3159(37°C)	—	
	0.3336(45°C)	—	
Myocardium	0.4974(10°C)	—	
	0.5148(23°C)	—	
	0.5334(37°C)	—	
	0.5441(45°C)	—	
Pancreas	0.4719(10°C)	—	
	0.4745(23°C)	—	
	0.4772(37°C)	—	
	0.4787(45°C)	—	
Renal Cortex	0.5085(10°C)	—	
	0.5237(23°C)	—	
	0.5402(37°C)	—	
	0.5496(45°C)	—	
Spleen	0.499(10°C)		
	0.5154(23°C)		
	0.5332(37°C)		
	0.5433(45°C)		
Liver	0.4889(25°C)	3.4802(23°C)	43
	0.5021(37°C)	3.4992(31°C)	
	0.5239(50°C)	3.5864(85°C)	
	0.5479(80°C)	—	
Subcutaneous Fat	0.15-0.17 (30-48°C)	—	302
Skeletal Muscle	0.43-0.51 (30-48°C)	—	

Table 2.7. Thermal properties of human systems at supra-zero temperatures i

System Type	Thermal Conductivity [W/mK]	Specific Heat Capacity [J/gK]	Reference
Renal Pelvis	0.4987(10°C)	—	
	0.5237(23°C)	—	
	0.5507(37°C)	—	
	0.566(45°C)	—	
Renal Medulla	0.5104(10°C)	—	
	0.5247(23°C)	—	
	0.5402(37°C)	—	
	0.549(45°C)	—	
Renal Cortex	0.5118(10°C)	—	
	0.5285(23°C)	—	
	0.5466(37°C)	—	
	0.5569(45°C)	—	
Myocardium	0.5045(10°C)	—	
	0.52(23°C)	—	
	0.5367(37°C)	—	
	0.5463(45°C)	—	
Pancreas	0.4649(10°C)	—	
	0.5019(23°C)	—	
	0.5417(37°C)	—	
	0.5645(45°C)	—	[41]
Lung	0.4189(10°C)	—	
	0.4341(23°C)	—	
	0.4506(37°C)	—	
	0.46(45°C)	—	
Liver	0.4808(10°C)	—	
	0.4959(23°C)	—	
	0.5122(37°C)	—	
	0.5214(45°C)	—	
Spleen	0.5043(10°C)	—	
	0.5212(23°C)	—	
	0.5394(37°C)	—	
	0.5498(45°C)	—	
Cerebral Cortex	0.5083(10°C)	—	
	0.5121(23°C)	—	
	0.5163(37°C)	—	
	0.5186(45°C)	—	
Fat of Spleen	0.3406(10°C)	—	
	0.3373(23°C)	—	
	0.3337(37°C)	—	
	0.3317(45°C)	—	
Liver	0.497(25.6°C)	3.4535(29°C)	
	0.51(36.9°C)	3.452(35°C)	[43]
	0.509(49.8°C)	3.4368(39°C)	
	0.519(78.3°C)	—	

BHMT, UMN: Bioheat & Mass Transfer Lab, University of Minnesota

n: Number of repetitions

Table 2.8. Thermal properties of human systems at supra-zero temperatures ii

System Type		Thermal Conductivity [W/mK]	Specific Heat Capacity [J/gK]	Reference
Kidney (n≥5)		0.591(25°C)	—	Unpublished, BHMT, UMN
		0.585(37°C)	—	
		0.56(50°C)	—	
		0.555(80°C)		
Liver		0.467-0.527(37°C)	—	303
Lung		0.302-0.55(37°C)	—	
Pancreas		0.294-0.588(37°C)	—	
Kidney		0.513-0.564(37°C)	—	
Heart		0.492-0.562(37°C)	—	
Spleen		0.448-0.544(37°C)	—	
Stomach		0.489-0.565(37°C)	—	
Skeletal Muscle		0.449-0.546(37°C)	—	
Adrenal Gland		0.363-0.458(37°C)	—	
Colon		0.556(37°C)	—	
Brain (white-gray)		0.503-0.576(37°C)	—	
Thyroid		0.526-0.533(37°C)	—	
Breast		0.499(37°C)	—	
Bone (rib)		0.373-0.496(37°C)	—	
Skin (Without SF)		0.258-0.272(37°C)	—	
Fat		0.2-0.246(37°C)	—	
Skin	1.6 mm	0.498(37°C)	—	
Fat	4.8 mm	0.268(37°C) (surface of fat)	—	
Fat	6.4 mm	0.248(37°C) (intermediate fat)	—	
Fat	9.8 mm	0.219(37°C) (deeper fat)	—	
Mesentery (n≥13)		0.303(25°C)	—	Unpublished, BHMT, UMN
		0.279(37°C)	—	
		0.242(50°C)	—	
		0.243(80°C)	—	
Omentum (n≥8)		0.26(25°C)	—	
		0.299(37°C)	—	
		0.251(50°C)	—	
		0.237(80°C)	—	
Gerota's Fascia (n≥2)		0.324(25°C)	—	
		0.279(37°C)	—	
		0.255(50°C)	—	
		0.178(80°C)	—	

BHMT, UMN: Bioheat & Mass Transfer Lab, University of Minnesota

SF: Subcutaneous Fat

n: Number of repetitions

Table 2.9. Thermal properties of cryoprotectants

System Type	Thermal Conductivity [W/mK]	Specific Heat Capacity [J/gK]	Reference
US Gel (Tissue Phantom)	0.52(38°C)	3.7(39°C)	274
	0.47(-2°C)	3.84(10°C)	
	1.71(-45°C)	2.06(-50°C)	
	2.3(-85°C)	1.45(-100°C)	
	2.28(-125°C)	0.94(-149°C)	
2M Glycerol Solution	1.61(-27°C)	3.781(-5°C)	14
	1.96(-64°C)	1.712(-73°C)	
	2.15(-108°C)	1.206(-110°C)	
	2.25(-147°C)	0.903(-148°C)	
6M Glycerol Solution	0.82(-28°C)	2.984(-20°C)	
	1.27(-65°C)	1.996(-73°C)	
	1.05(-108°C)	1.114(-110°C)	
	0.97(-147°C)	0.834(-148°C)	
2M DMSO Solution	1.443(-20°C)	—	35
	1.69(-60°C)	—	
	1.933(-100°C)	—	
	2.203(-140°C)	—	
6M DMSO Solution	0.378(-20°C)	—	
	0.592(-60°C)	—	
	0.721(-100°C)	—	
	0.773(-140°C)	—	
10M DMSO Solution	0.28(-20°C)	—	
	0.27(-60°C)	—	
	0.264(-100°C)	—	
	0.253(-140°C)	—	
DP6 in EC Solution (cryoprotectant)	0.317(-20°C)	—	36
	0.53(-40°C)	—	
	0.356(-70°C)	—	
	0.35(-140°C)	—	

Table 2.10. Thermal properties of porcine liver treated with cryoprotectants

System Type	Thermal Conductivity [W/mK]	Specific Heat Capacity [J/gK]	Reference
Porcine Liver, treated with 1X PBS + 2M Glycerol	1.56(-10°C)	3.39(20°C)	
	1.68(-64°C)	3.36(3.7°C)	
	1.78(-108°C)	3.09(-7.3°C)	
	1.73(-146°C)	2.55(-13°C)	
	—	2.1(-36°C)	
	—	1.85(-57.2°C)	
	—	1.58(-72.8°C)	
	—	1.45(-89°C)	
	—	1.17(-104.9°C)	
	—	0.8638(-143.8°C)	
Porcine Liver, treated with 1X PBS + 6M Glycerol	1.0(-13°C)	3.03(23.5°C)	62
	1.55(-64°C)	2.91(-8.5°C)	
	1.42(-110°C)	2.81(-24.3°C)	
	1.24(-148°C)	2.51(-43.6°C)	
	—	2.28(-57.4°C)	
	—	1.94(-82.2°C)	
	—	1.76(-98.3°C)	
	—	1.33(-106°C)	
	—	1.05(-114.4°C)	
	—	0.83(-145.8°C)	
Porcine Liver, treated with 1X PBS + 8M Glycerol	0.65(-10°C)	2.91(20.3°C)	
	1.27(-64°C)	2.69(-23.2°C)	
	1.07(-109°C)	2.42(-36.2°C)	
	0.86(-149°C)	2.15(-56.2°C)	
	—	1.9(-83.4°C)	
	—	1.62(-103°C)	
	—	2.51(-43.6°C)	
	—	1.19(-111.2°C)	
	—	0.96(-118.7°C)	
	—	0.81(-142.8°C)	

2.6. Conclusion

The goal of this review was to compile thermal conductivity and specific heat capacity values of human and porcine systems in the subzero and supra-zero temperature ranges for the purposes of aiding the development of accurate models of conditions and pathologic treatments involving bio-heat transfer mechanisms. As seen in tables 2.4-2.10 listed above, extensive datasets were available for thermal conductivity in both temperature ranges for porcine systems. However, limited data is available for both thermal conductivity and specific heat capacity for human systems in the subzero

temperature range. Another area where there is limited data available is the effect of cryoprotectants on biomaterials. As was seen in Figs. 2.5 and 2.6 for porcine liver, thermal properties of biomaterials are affected by the presence of cryoprotectants due to the presence of a vitreous or amorphous phase in addition to crystallization. Future thermal property measurements can be conducted by incorporating these changes to get a more accurate behavior to be applied in a model. As seen in the modeling case studies section, the importance of temperature dependent properties versus constant properties is reflected from the significant differences in the thermal histories for planar, cylindrical and spherical systems using water properties. Similar analyses can be performed by considering thermal properties of other biomaterials presented in this chapter.

2.7. Specific Acknowledgements

3. A Micro-Thermal Sensor for Focal Therapy Applications

The following chapter appeared in publication:

Natesan, H., & Bischof, J. C. (2017). Multiscale thermal property measurements for biomedical applications. ACS Biomaterials Science & Engineering, 3(11), 2669-2691.

3.1. Introduction

Focal energy based therapies have a long use in the treatment of cancer, cardiovascular and neural disease[1, 19, 271]. As the technique evolves, there are increasingly thin and complex tissue anatomies where focal therapies and freezing are being applied that require sub mm monitoring accuracy to avoid debilitating side effects. For instance, cryogenic approaches to treatment of atrial fibrillation are increasingly being used in the pulmonary vein (PV) which is only $1 - 2$ mm thick[304-307]. This treatment in thin PV often suffers from over and under-freezing suggesting a need for better monitoring. Unfortunately, traditional clinical imaging has difficulty monitoring at or below the mm scale, which is of the order of thickness of the PV itself. For this reason it is not surprising that in a pilot computed tomography (CT) study, we were unable to visualize the PV or the freezing process within it[308]. So, despite the past successes of clinical image guidance for cryoablation in cm sized tissues[309-311], clinical imaging alone lacks the spatial resolution to successfully monitor freezing in the PV or other thin tissue structures (1-2 mm thick).

Thus, there is an urgent need to monitor tissue contact, thickness and freeze completion during treatment which relatively low-resolution clinical imaging cannot provide at the millimeter to sub millimeter scale. Here we provide evidence that a future solution could involve a micro- thermal sensor based on the "3ω" technique of thermal conductivity measurement (Fig. 3.1)[47]. The sensor comprises a thin metallic heater line, typically made of gold, and deposited on a flat glass substrate

(for additional experimental details, see the Methods section below). By application of alternating electric current to the heater line, thermal waves can be produced which penetrate to a depth (PD) that is inversely proportional to the square root of the electrical current frequency, $\omega^{(1/2)}$. From the output signal of the sensor, the average thermal conductivity 'k' of the volume traversed by the thermal wave could be obtained. This technique has been commonly used to measure thermal conductivity of inorganic materials[90,312-314]. Recently, it has been modified to measure 'k' of biological tissues[45] and even cells[105]. The current article presents proof of principle data to show the ability of the sensor to give thermal conductivity for treatment planning and then extends the sensor use for other measurements relevant for monitoring. For instance, we use the sensor to make the first measurements of 'k' of pulmonary vein and the surrounding phrenic nerve and esophageal tissue to prove its ability for use with these thin (< 3 mm) cardiac tissues. Next, we modify the sensor use to demonstrate contact with tissue vs fluid (i.e. water), fluid flow conditions, tissue thickness 'τ', and freeze completion in fluid or tissue systems. This was achieved by integrating the sensor onto an idealized probe surface (i.e. a flat glass substrate) and testing through in vitro experiments. In future, with proper characterization and calibration, the sensor could potentially be integrated onto flexible and stretchable probe surfaces for *in vivo* use (e.g. cryoballoons and cryoprobes)[315-318].

3.2. Methods

3.2.1. 'Supported' 3ω technique

Fig. 3.1 shows the basic concept of the supported 3ω method[45]. A periodic electrical current (~ 40 mA rms) of angular frequency 'ω' is passed through the heater, $I = I_0 \sin \omega t$, between the leads I+ and I-. This causes Joule heating with a 2nd harmonic component, $Q_{AC} = Q_0 \sin 2\omega t$. Thus, the heater strip acts like a periodic line heat source producing thermal waves as

69

shown in Fig. 3.1 (b, d). The exact analytical solution to this conduction problem is well known[45, 47, 319]. Thermal waves propagate and decay radially away from the heater and PD can be calculated using Eqn. (3.1)

$$PD = \sqrt{\frac{D}{(2\omega).(2\pi)}}$$
(3.1)

where D - thermal diffusivity (m^2/s), 2ω- frequency of Joule heating (Hz). The temperature rise of the heater strip due to Joule heating is inversely proportional to the effective 'k' of the system, oscillates at 2ω, and is typically kept smaller than 1 K rms. Subsequently, the temperature oscillation causes the heater's electrical resistance 'R' to also fluctuate at 2ω. Finally, when multiplied by the 1ω current, this 2ω resistance fluctuation causes a
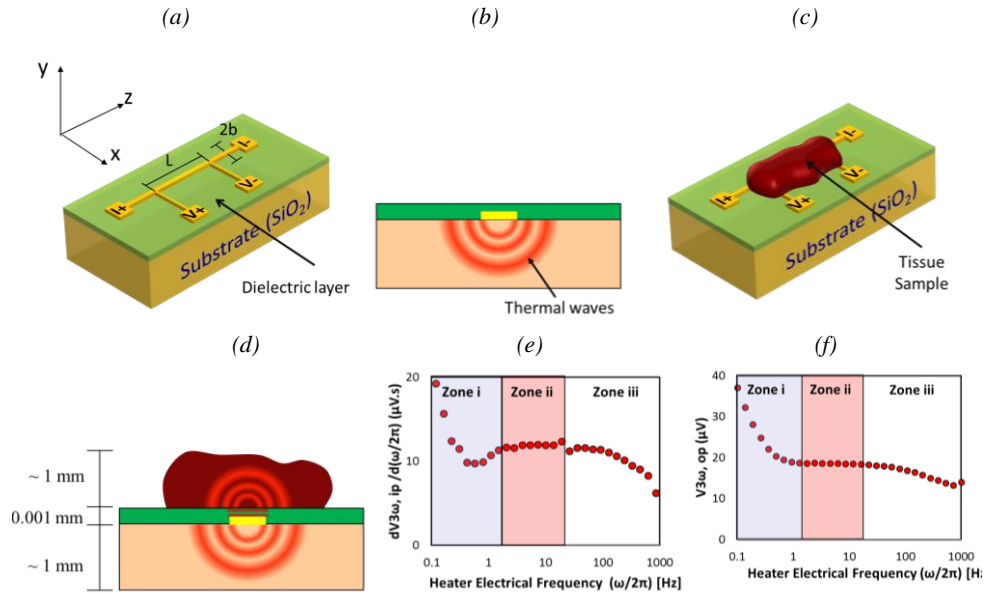
Figure 3.1 Concept of the supported 3ω method to measure thermal conductivity, 'k' of thin (>0.1 mm) tissues. (a) Supported 3ω sensor comprises a metal heater line with typical dimensions of b = 30 to 80 μm wide, L= 1.5 to 2.5 mm long, ~200 nm thick, microfabricated onto a glass substrate and coated with a dielectric layer[45]. (b) Side view (xy plane) of the sensor showing calibration to determine k_{sub}. (c) Tissue is placed on top of the sensor to measure its k. (d) Side view (xy plane) showing thermal waves penetrating into the tissue and the substrate. (e, f) Data from measuring k of ~1 mm thick frozen agargel at -25 ^{0}C with air as a backside boundary condition of the sample. (e) Third harmonic voltage slope ($dV_{3\omega, ip}$ /dω) and (f) $V_{3\omega, op}$ as a function of frequency of driving current 'ω'; ip is the "in phase" component of the signal, and op is the "out of phase" component. Zones (i) and (iii) refer to the frequency range where the assumptions of Eqns (3.3) and (3.4) are not satisfied. Zone (ii) refers to the range where the assumptions of semi-infinite solid and 1D heat source are satisfied.

70

component of voltage across the heater to oscillate at the 3rd harmonic. Thus, the resulting

3ω voltage (~10s to 100s of μV), measured between the leads V+ and V- using a lock in

amplifier, results in k_{total}, which contains information about the known 'k' of the substrate,

'k_{sub}', and the unknown 'k' of the sample, 'k_{sample}'. A lock in amplifier is needed to extract

3ω signals of low magnitude from the noisy environment. To determine k_{sample} of a

biological tissue, the sample is placed on top of the sensor as in Fig. 3.1 (c, d). The effective

thermal conductivity, 'k_{total}', measured from the 3ω voltage, satisfies Eqn. (3.2) (< 1 %

error)[45] with k_{sub} known from calibration,

$$k_{total} = k_{sample} + k_{sub} \tag{3.2}$$

Next is the determination of 'k_{total}' from the 3ω voltage, which comprises two components

- in phase and out of phase. k_{total} can be determined from either of these components as

shown in Eqns. (3.3) and (3.4).

$$k_{total} = \frac{\alpha R^2 I^3}{4\pi L} \left(\frac{d \ln \omega}{d V_{3\omega,ip}} \right) \tag{3.3}$$

$$k_{total} = \frac{\alpha R^2 I^3}{8 L V_{3\omega,op}} \tag{3.4}$$

where α - temperature coefficient of resistance (1/^{0}C), L- Length of the heater line (m), $V_{3\omega,ip}$ - in-phase component, and $V_{3\omega,op}$ - the out of phase component of the 3ω output voltage

(V). Eqns. (3.3) and (3.4) can only be applied in a certain frequency range where their

assumptions are satisfied.[47] The first assumption is that the substrate and the sample are

semi-infinite, (τ_{sub}/PD > 5 and τ_{sample}/PD > 5 for 1% error)[91], which bounds the frequency

($\propto 1/$ PD^2) in the lower limit. The next assumption is that the heater is a one dimensional

cylindrical heat source (PD/b > 5 for 1% error)[91] bounding the frequency in the upper limit. For instance, a representative sensor (L= 2 mm, b=30 μm) was used to measure the 'k' of 1 mm thick frozen agargel at -25 ^{0}C. In this case, PD should be between 0.08 mm (PD/b > 5) to 0.2 mm (τ_{sample}/PD>5), which corresponds to a frequency 'ω' range of 2 to 20 Hz (D_{ice} /(2•PD^2) from Eqn. (3.1)). The raw data in Fig. 3.1 (e) shows that $V_{3\omega, ip}$ is linearly proportional to ln (ω) in zone (ii), thus satisfying the assumptions of Eqn. (3.3). The varying slope in the zone (i) indicates that the assumption of semi-infinite solid is violated, while the variation in zone (iii) indicates that the assumption of 1D heat source is violated. Similarly, $V_{3\omega, op}$ is independent of frequency in zone (ii), thus satisfying the same assumptions in Eqn. (3.4). Thus, the average slope value ($dV_{3\omega, ip}$/dω) and the average $V_{3\omega, op}$ in zone (ii) is used in Eqns. (3.3) and (3.4). For traditional 3ω k measurements, the k determined from ($dV_{3\omega, ip}$/dω) is the value commonly reported in the literature[47, 320] as the slope is independent of contact resistance between the heater line and the sample.[312] Importantly, both $V_{3\omega, op}$ and $V_{3\omega, ip}$ can be used to sense contact, thickness, and phase change. However, $V_{3\omega, ip}$ requires multiple frequencies for thickness measurement and thus longer times making it less attractive for our intended use (See SI).

3.2.2. Thermal conductivity measurement of thin cardiac tissues

The construction of the sensor is explained in SI 1. Porcine PV, esophagus and phrenic nerve were obtained from sacrificed animals from other IACUC approved studies, immersed in phosphate buffered saline (PBS) and stored in a 4 ^{0}C refrigerator[62]. During measurement, the tissue was sliced into approximately 2 mm long samples and placed on the heater line. To avoid dehydration and/or evaporation of water content in the tissue, the sample was encapsulated on the sides and at the top by agar gel (0.5 % by weight agarose powder

dissolved in water at 65 ^{0}C and solidified overnight in a 4 ^{0}C refrigerator). The sample- agar gel complex is then covered by a plastic wrap to isolate the sample from evaporative cooling and sublimation which interfere with a consistent and correct measurement[45]. Importantly, in this system, water evaporation or ice sublimation from the tissue was negligible (weight change< 5%) during the measurement in Fig. 3.2. Finally, all measurements were made within 24 hours after tissue host sacrifice to avoid significant changes in water content[43].

3.2.3. Sensing contact versus flow

Our experimental setup consists of a supported 3ω sensor (L=2.5 mm, b=50 μm) and a variable speed peristaltic pump (Cole-Parmer Masterflex®). A velocity range of 10 to 60 cm/s was chosen to mimic blood velocity in cardiac vessels. For sensing tissue contact, PV was manually placed on top of the sensor, thereby blocking the water flow. The sensor recorded the $V_{3\omega, op}$ ($\propto 1/k$) at fixed frequency of 10.1 Hz (constant PD) and input RMS current of 30 mA. A lock-in time constant of 1 s was selected as a compromise between measurement noise and time response of the measurement system. The chosen frequency is a typical value used to measure 'k' of biological tissues (> 0.1 mm thick) with temperature above 0^0C (see zone (ii) of Fig. 3.1 (e, f)).

3.2.4. Sensing tissue thickness

Agargel (0.5% weight of agarose in water) was placed on the sensor (L=2 mm, b=30 μm) and immediately frozen to -25 ^{0}C in a cryofreezer (Planer Kryo 10 Series III). Next, for an input RMS current of 20 mA, $V_{3\omega, op}$ was recorded as a function of frequency at a fixed temperature of -25 ^{0}C on the sensor surface. First, the backside boundary condition was changed to be thermally insulated (plastic, k~ 0.2 W/m.K) vs isothermal (Copper, k~385 W/m.K) at -25 ^{0}C for constant sample thickness (~0.5 mm). Next, the thickness of frozen

73

agargel was changed from ~0.48 mm to ~1.98 mm while keeping the backside boundary condition as air (k_{air}~ 0.02 W/m.K) at -55 ^{0}C[321].

3.2.5. Sensing phase change

Deionized water was pipetted onto the sensor (L=1.5 mm, b= 80 µm). The dielectric layer caused the water to bead instead of spread, with the water droplet having an approximate spherical diameter of 2 mm. The temperature was lowered from 20 ^{0}C to -10 ^{0}C, allowing the water droplet to completely freeze into ice. After allowing the freezing event to complete, and the voltage to

(a)

(b)   *(c)*
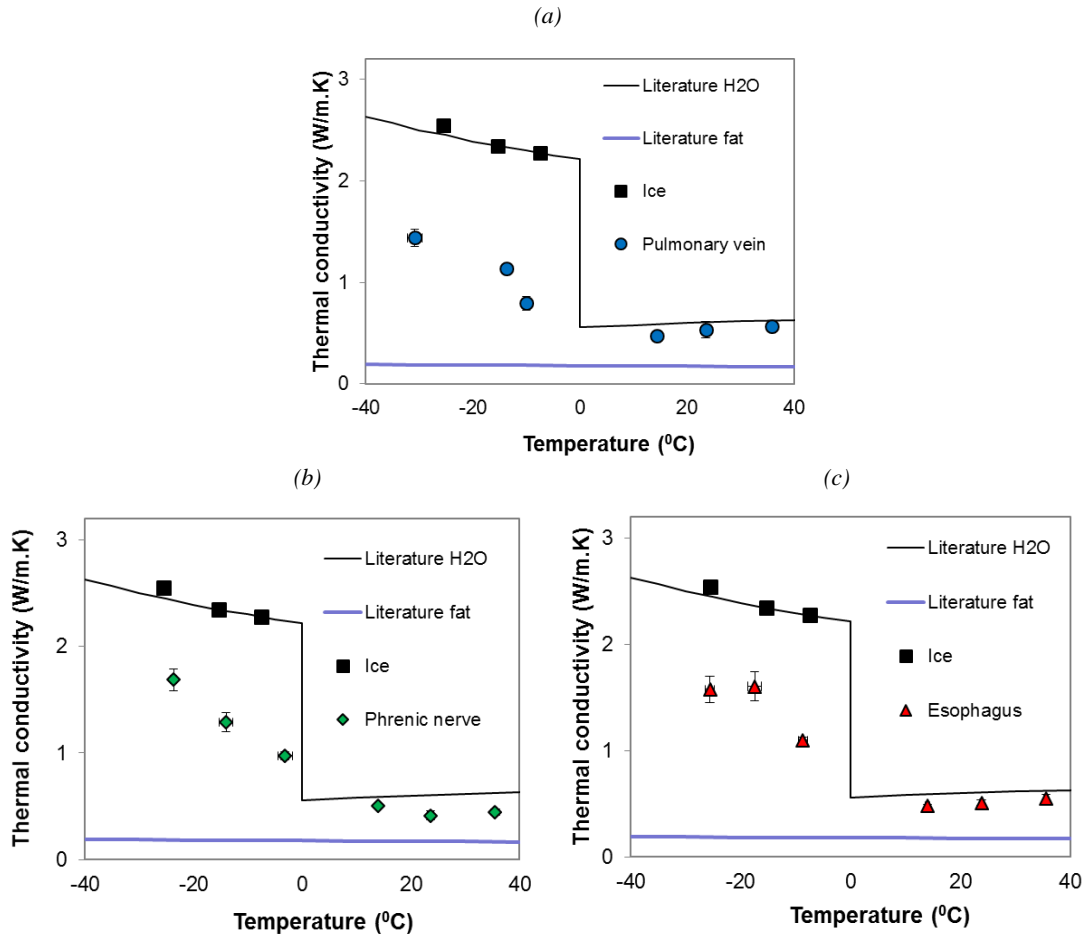
Figure 3.2 Supported 3ω measurements of porcine PV, phrenic nerve and esophagus. *Measurements are the average ± standard deviation of N = 5 samples and validated using ice measurements (black points). The difference in k between frozen and unfrozen tissue is roughly a factor of 2. The black and yellow trend-line data are k values of water, ice and fat from literature[121]*

stabilize, the temperature was increased back to 20 ^{0}C. Completion of freezing and thawing events were verified by visual inspection during the experiment. A measurement frequency of 1.03 Hz was used, having PD in deionized water of 0.46 mm with a lock-in time constant of 1 s. This experimental procedure was repeated on a mouse liver sample (thickness~3 mm) to confirm the behavior in biological tissues.

3.3. Results

3.3.1. Thermal conductivity measurement of thin cardiac tissue
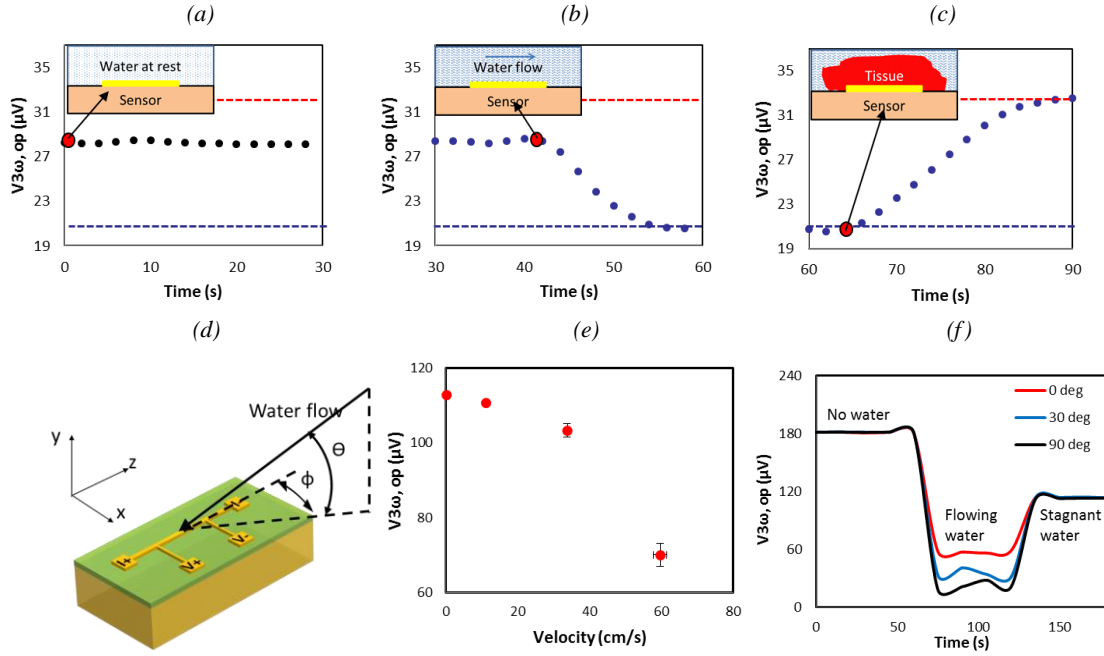
Figure 3.3 The measurement of flow vs. tissue contact by 3ω sensor. *Plots in (a-c) show three cases with the schematic inset (x-y plane) for the events: (a) water at rest; (b) water flowing; and (c) tissue in contact with 3ω sensor. Red dots represent the beginning of these events. In all cases the resulting V $_{3ω, op}$ measured from a representative experiment is shown on the y-axis in µV showing that the signal of flowing water < water at rest < bio-tissue using dashed lines of data as visual guides. In the bottom row (d – f), graphics in (d) show a water flowing past the sensor at an azimuthal angle 'φ' and polar angle 'Ө'. Further, (e) shows V $_{3ω, op}$ correlates with flow rate for φ=90 ^{0}, Ө=0 ^{0}, while (f) shows V $_{3ω, op}$ correlates with a variable 'φ', under fixed 'Ө' of 0 ^{0} and flow rate of 20 cm/s (with some oscillations between 60 s and 120 s due to transient behavior of the pump). Data in (e) and (f) were obtained with a different input current of 30 mA. Data in (e) is the average ± standard deviation of N=5 samples. Horizontal error bars are less than 5%.*

Fig. 3.2 shows the first k measurement of porcine pulmonary vein, phrenic nerve, and esophagus by 3ω sensors with typical dimensions of heater line length, L= 1.5 to 2.5 mm and width, b= 30 to 80 μm. The protocol for sample handling is explained in Methods section. During phase change the k increases by roughly a factor of 2 in all tissues upon freezing due to ice formation. This will be important for measurement of the onset and completion of freezing as will be explained later.

3.3.2. Sensing contact

Fig. 3.3 (a-c) shows the schematic of the experimental water flow vs. tissue contact setup and the corresponding change in the 3ω out of phase output voltage, $V_{3\omega, op}$ from the sensor (L=2.5 mm, b=50 μm). A constant $V_{3\omega, op}$ is obtained for stagnant water (0 to 42 s). As water flows (from 42 s), $V_{3\omega, op}$ drops due to convective heat loss at the heater line. After placing a piece of pulmonary vein (1 mm thick) on top of the sensor at 64 s, it blocks the water flow and thereby increases the $V_{3\omega, op}$ to the highest value of all cases. These results demonstrate that we can sense tissue contact vs. flow. Furthermore, the sensor can measure increases in flow rate directly from $V_{3\omega, op}$ as shown in Fig. 3.3 (e). An added benefit is that the signal change can be measured as a function of azimuthal angle (ϕ) of the flow, where the signal is maximum for $\phi = 90^0$ to the sensor. These effects can be explained by laminar convective flow over a flat plate as described in Supplementary Information (SI 3.4).

3.3.3. Sensing tissue thickness

Two experiments were conducted using a 3ω sensor (L=2 mm, b=30μm). For the case of varying backside boundary condition and fixed sample thickness (Fig. 3.4 (a)), at low frequencies (zone (i)), $V_{3\omega, op}$ increases for insulated condition and vice versa for fixed temperature condition. In the next experiment (Fig. 3.4 (b)), the backside boundary condition was air at -55 ^{0}C, closely approximating an adiabatic boundary. Fig. 3.4 (b) shows

76
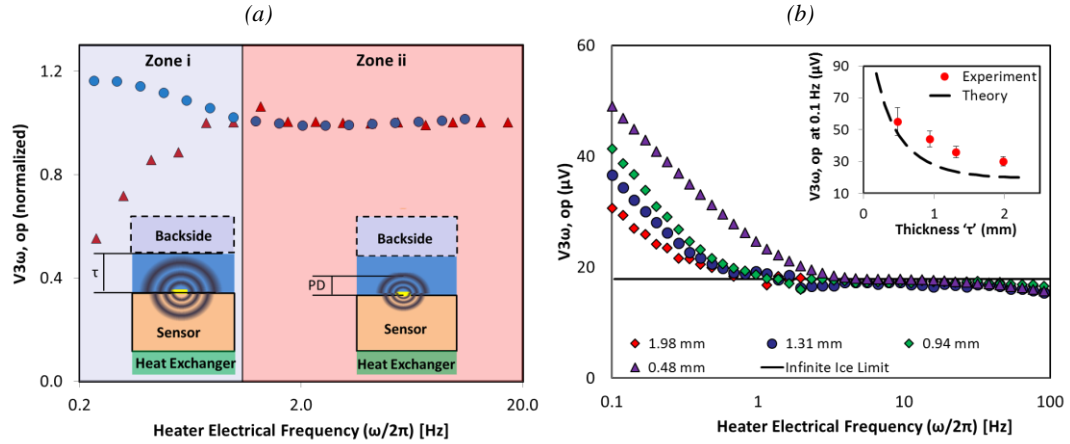
Figure 3.4 The measurement of thickness by 3ω sensor. *(a) Plot shows a representative experiment of $V_{3\omega, op}$ shown in y-axis, where at low frequencies in zone (i), it depends on backside boundary for fixed sample thickness ($\tau \approx 0.5$ mm). Blue circle data represents the case where backside of the sample is low k plastic (quasi-adiabatic) and red triangle data represents the case where backside is high k copper at fixed temperature (quasi-isothermal). Inset schematic shows the comparison between PD and τ for zones (i) and (ii). (b) Plot shows a representative experiment where $V_{3\omega, op}$ at low frequencies in zone (i) depends on sample thickness for a fixed backside boundary condition of air. Ice of known thickness (as noted inside figure) is placed on the surface of the sensor at -25^0C. Backside boundary condition is air at -55^0C. Inset shows plot of $V_{3\omega, op}$ at 0.1 Hz vs thickness of the sample 'τ'. Data is the average $\pm$ standard deviation of N=3 samples.*

$V_{3\omega, op}$ to be independent of thickness in the zone (ii) where the frequency is high enough for the thermal penetration depth (PD) to be within the sample. Below a characteristic frequency (zone (i)), the measurements become very sensitive to the backside boundary condition, leading to an abrupt increase in $V_{3\omega, op}$ as a function of the thickness. This thickness dependence can also be appreciated by plotting $V_{3\omega, op}$ at a single low frequency such as 0.1 Hz as shown in Fig. 3.4 (b-inset). The PD of thermal waves can be calculated by PD=$(D/2.\omega)^{0.5}$, where D is thermal diffusivity (m^2/s)). At 0.1 Hz, the PD into the frozen agargel is ~1 mm. A comparison of an idealized theoretical calculation[45, 91] with the experiment shows that the experimental measurements are consistent with the model trends, and suggest that with proper calibration can be used to measure thickness.

3.3.4. Sensing phase change

Two freezing trials were conducted, one with water (Fig. 3.5 (a)), and one with mouse liver (Fig. 3.5 (b)) using a 3ω sensor (L=1.5 mm, b=80 μm). Both trials show the same overall pattern, with a region of stable $V_{3\omega, op}$ at the beginning of the trial, corresponding to when the water droplet is completely liquid. The temperature of the stage below the sensor was changed to -10 ^{0}C at ~120 s (~150 s for mouse liver), after which there is a drop in $V_{3\omega, op}$. This is followed by a region of stable voltage as the droplet is completely frozen from 120 s to 340 s (150 s to 550 s for mouse liver). This stable region has a lower $V_{3\omega, op}$ value than the region corresponding to unfrozen water (Fig. 3.5 (a)) or tissue (Fig. 3.5 (b)). This is due to the higher *k* of ice / frozen tissue than water / thawed tissue (Fig. 3.2). After 340 s (~550 s for mouse liver), the temperature stage is changed to a set point of 20 ^{0}C, followed by a region of changing voltage. The graph ends with a third stable region, corresponding again to unfrozen water / tissue. The voltages at the beginning and the end of the above data match closely (to within 3%), showing that water $V_{3\omega, op}$ measurements are repeatable. In both cases, the stabilized voltages between the unfrozen water and solid ice differ by at least 35%. The measurement noise, taken as the standard deviation of $V_{3\omega, op}$ of frozen liver between 400 and 500 s in Fig. 3.5 (b), is ~ 0.1 μV which is an order of magnitude smaller than the signal change due to freezing / thawing (i.e., ~ 5 μV) . Furthermore, a theoretical prediction of the behavior of $V_{3\omega, op}$ during a forced change in 'k' of a water droplet at 0 ^{0}C shows a similar trend showing the ability to sense phase change (Fig. 3.5 (c)). The thickness of ice (τ_{ice}), which is characterized by normalized ice thickness (τ_{ice}/τ_{total}), grows from the surface below and the ice–water interface is represented by an isotherm of 0 ^{0}C. It is important to note that the theoretical prediction of change in $V_{3\omega, op}$ is based only on change in '*k*' and the model does not account for the effect of exothermic heat release during freezing.

3.4. Discussion

In this work we demonstrate the ability of supported 3ω sensors to run in both traditional (steady-state) and a new dynamic mode to measure both thermal properties (traditional use) as well as tissue contact, thickness and phase change relevant to the monitoring of focal therapy in thin tissues. The new "supported 3ω" approach (Fig. 3.1), which is a variant of traditional 3ω technique[46-47] can measure 'k' within thin tissues (as low as 0.1 mm)[45] and even cells[45, 105]. For the first time, this study uses this approach to measure the thermal conductivity of thin cardiac tissues (< 2 mm) such as porcine pulmonary vein, esophagus and phrenic nerve for focal therapy treatment planning (Fig. 3.2). These properties will be necessary to thermally model focal therapies (i.e. treatment planning) within the pulmonary vein and surrounding tissues and are currently not available in the literature[14]. In addition, we show a new use of the sensor based on $V_{3\omega, op}$ to detect tissue contact, thickness and phase change. Importantly, $V_{3\omega, ip}$ can also be used to sense contact, thickness, and phase change although requiring multiple frequencies and thus longer times which make it unattractive for a focal therapy application (See SI).
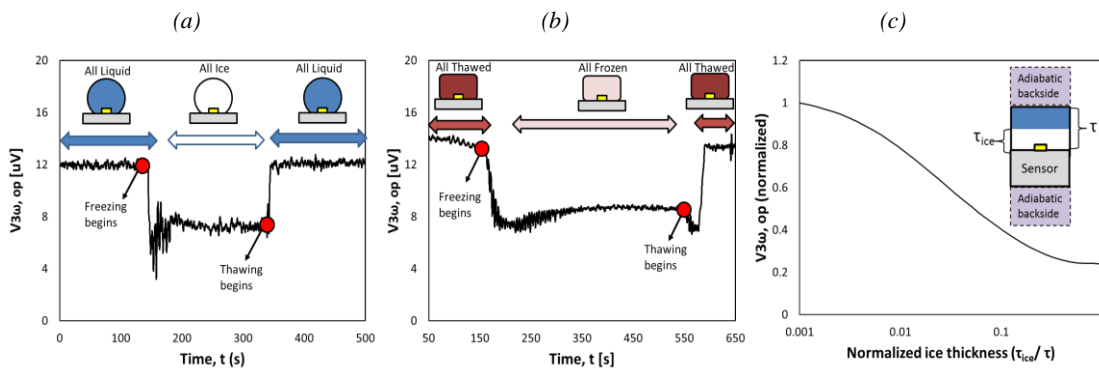
Figure 3.5 The measurement of phase change onset, completion and thaw by the 3ω sensor. *Representative experiments of freezing (a) water drop and (b) mouse liver freezing is from bottom to top. $V_{3\omega, op}$ was measured as a function of time at constant PD (i.e. frequency-1.03 Hz). In (a) water was cooled from below at ~120 s and thawed at ~340 s. In (b) mouse liver was cooled from below at ~ 150 s and thawed at ~550 s. (c) Theoretical prediction of behavior of $V_{3\omega, op}$ at 1 Hz, as a function of normalized thickness of ice as freeze front propagates from below during cooling. Inset schematics are not drawn to scale.*

79

Fig. 3.3 shows the new ability of the sensor to detect contact with tissue vs fluid (i.e. water) with different 'k'. The response time is typically ~15 s as shown in Fig. 3.3(a-c). Further, by calibrating the reduction in $V_{3\omega, op}$ one can also sense different fluid flow rates (as shown in Fig. 3.3 (e)). Once in contact with the tissue, the sensor can be used to measure the thickness of the pulmonary vein (or other thin luminal structure in contact). Thickness measurements exploit the low frequency (PD ≈ sample thickness) regime in zone (i) of Figs. 3.1 (e, f) and 3.4 (a). Thus, the frequency of the electric current can be reduced such that the PD of the thermal wave is comparable to the thickness of the sample. At this point, the signal becomes sensitive to the backside boundary condition as shown in Fig. 3.4 (a) zone (i). Fig. 3.4 (b) inset shows that $V_{3\omega, op}$ increases with thickness at lower frequencies, showing an increased sensitivity to the backside boundary condition (in this case air) as PD increases. However, there is a discrepancy in magnitude between the theory[45, 91] and experiment despite a similar trend. This difference could be attributed to the complex construction of the sensor (i.e. multi-layered geometry) as compared to the theoretical model. In the experiments, the sensor has a second glass substrate (~1 mm thick) as a physical support, attached with polyimide adhesive (~100 μm thick). Furthermore, the sensor is placed on top of a temperature control stage (~ 2 mm from the heater line). In addition, there are copper wires and epoxy bonds connecting the heater line to the electronics. This complicates the thermal model, especially at lower frequencies where the relatively long time constants allow deeper PD from this multi-layered sensor geometry. In contrast, theory assumes a simpler, more idealized sensor geometry as depicted in Figs. 3.1 (a-d) and 3.4 (a- inset). Despite these differences, a consistent trend between the theory and the experiment provides a qualitative proof that the sensor can measure thickness, and absolute agreement can be explored further in the future.

Table SI.3.1. Comparison of thermal conductivity measurement techniques

Measurement Characteristics	Current techniques*	Traditional 3ω	Supported 3ω
Can measure sizes < 1 mm	✗	✓	✓
Compensates for Parasitic Heat Loss	✗	✓	✓
Compensates for Contact Resistance	✗	✓ (only for in –phase)	✓ (only for in –phase)
Use in Biomaterials	✓	✗	✓
Reuse possible	✓	✗	✓
Avoids Microfabrication	✓	✗ (necessary for every sample)	✗ (necessary for one sensor only)

*The 'Current Techniques' refers to a representative sample of techniques (Guarded Hot plate, Embedded Thermistor, Cut bar) (Reproduced from Lubner et al IMECE 2012 with Copyright (2012) Permission from ASME)[176]

Next, the sensor can be used to sense the phase change in the tissue (Fig. 3.5). During freezing, the change in 'k_{sample}' between frozen and thawed tissue (Fig. 3.2) leads to a change in the $V_{3\omega, op}$, and an inverse behavior during thawing. In addition, theoretical predictions in Fig. 3.5 (c) show that $V_{3\omega, op}$ is a function of ice thickness as the ice front propagates away from the sensor.

An important aspect of sensing is the need to minimize measurement time, which increases as sensor frequency decreases (i.e., PD increases). Thus, the sensor would require long electronic time constants, especially for several mm thickness measurements to obtain a stable signal. The longest electronic time constant used in this article is 10 s at ~0.1 Hz. In comparison, cryotherapy of PV typically lasts ~120 s[304] and clinical imaging techniques have temporal resolution of < 1 s[307, 322-330]. Further reduction in the time of measurement and possibly multiplexing at a variety of frequencies remain interesting and important future improvements for this measurement.

3.5. Specific Acknowledgements

SI 3.1. Supplementary Information: Construction of the Supported 3ω Sensor

The advantage of supported 3ω sensors is summarized in Table SI.3.1. Using standard photolithography and liftoff microfabrication techniques, a gold heater line, with typical dimensions of 30 μm wide, 1 to 3 mm long, and 200 nm thick is deposited on a glass substrate (1 mm thick amorphous SiO_2). A 5 nm thick Chromium adhesion layer holds the gold heater line and glass together. The heater lines are connected to the signal processing unit and a lock in amplifier (SR 830, SRS, Sunnyvale CA) using copper wires. As the soft, hydrated biological tissue is weakly electrically conducting, a thin dielectric film is incorporated between the heater and the sample to prevent electrical cross-talk, after connecting the wires to the heater line. This was achieved by dissolving polystyrene pellets in toluene at a concentration of 15 mg/mL. A few drops of the solution were dropped directly on top of the sensor, which was then held vertical to allow excess solution to run off. The toluene evaporates in 5 to 10 seconds leaving a thin continuous layer (~ 1μm) of polystyrene dielectric layer (Fig. 3.1 (a, b)).

SI 3.2. Supplementary Information: Theory behind Flow Rate Measurement

The theory behind flow rate measurement is that the electrical power input to the heater is lost as heat by conduction to the substrate below and convection to the flowing water above the sensor as given by Eqn. (SI.3.1).

(a)

(b)

(c)   *(d)*
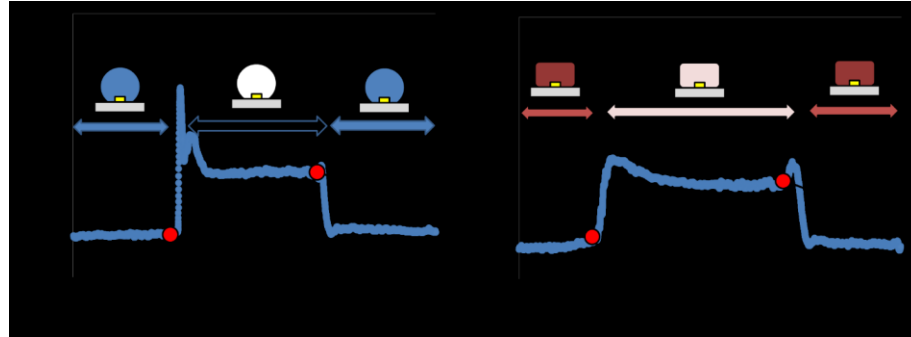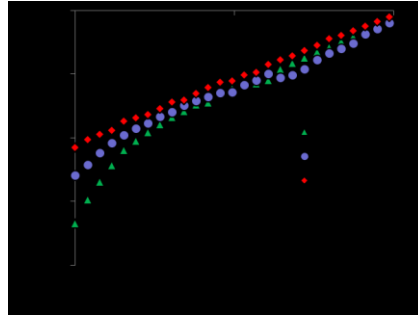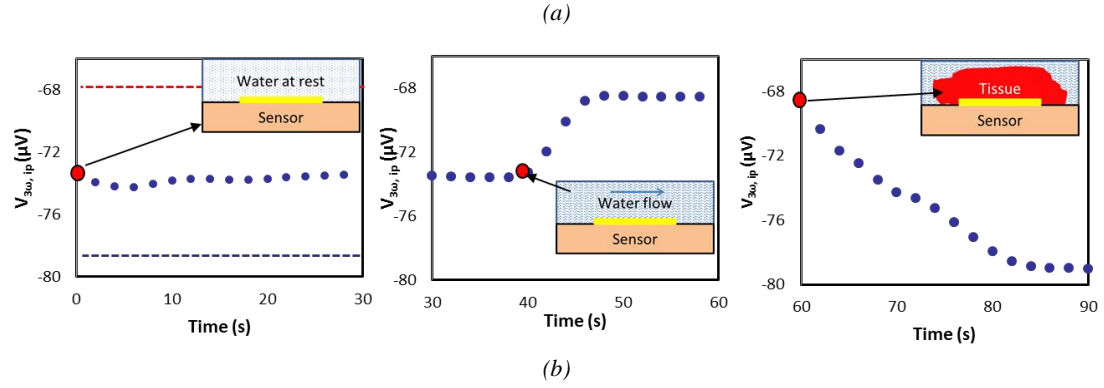
Figure SI.3.1. Use of in phase 3ω signal (V₃ω, ip) to sense (a) contact, (b) thickness and (c) phase change. *(a)*
Sensing contact.Plots in (a) show three cases with the schematic inset (x-y plane) for the events, water at rest,
water flowing, and tissue in contact with 3ω sensor. Red dots represent the beginning of these events. (b) Sensing
thickness: Plot shows that $V_{3\omega, op}$ at low frequencies (<~0.5 Hz) depends on sample thickness for a fixed backside
boundary condition of air. Ice of known thickness is placed on the surface of the sensor at -25⁰C. Backside
boundary condition is air at -55⁰C. (c, d) Sensing Phase change: Representative experiments of freezing water
drop and mouse liver freezing is from bottom to top. $V_{3\omega, op}$ was measured as a function of time at constant PD
(i.e. frequency-1.03 Hz). Water was cooled from below at ~120 s and thawed at ~340 s. Mouse liver was cooled
from below at ~ 150 s and thawed at ~550 s.

$$Q = I^2 R = h_{conv} A \left(T_{hl} - T_f \right) + G_{cond} \left(T_{hl} - T_\infty \right) \tag{SI.3.1}$$

where Q is Joule heating power input to the heater line (W), h_{conv} is convective heat transfer

coefficient (W/m².K), G_{cond} is thermal conductance of the substrate (W/K), A is footprint area (L x

b) of the heater line (m^2), T$_{hl}$ is temperature of the heater line (K), T$_f$ is temperature of the fluid (K), and T$_\infty$ is ambient environment temperature (K). The variables in Eqn. (S1.3.1) can in general be complex and time-dependent. If current 'I' and the substrate thermal conductance 'G$_{cond}$' are maintained constant, then changes in convective heat loss (h$_{conv}$) arising from changing the flow will result in changes in the temperature at the heater (T$_{hl}$). This will be reflected as changes in 'R', and thus V$_{3\omega, op}$. Thus, the sensor can be used to sense flow rate in a similar fashion to other past approaches such as hot wire anemometry[331-332].

SI 3.2.1. Dependence of 3ω signal on flow direction

Fig. 3.3 (f) shows the signal change depends on the azimuthal angle (ϕ) of the flow direction. These effects could be explained by laminar convective flow over a flat plate with an unheated starting length, as shown in the Eqn. (SI.3.2)[333]

$$h_{conv} = \frac{\overline{Nu}_x k_{water}}{x} = \overline{Nu}_x \Big|_{\xi=0} \frac{k_{water}}{x - \zeta} \left[1 - \left(\frac{\zeta}{x} \right)^{\frac{3}{4}} \right]^{\frac{2}{3}} \qquad (SI.3.2)$$

where 'x' is the total distance travelled by water on the substrate. 'ζ' is the unheated starting length, referring to the distance travelled by water over unheated glass substrate and 'x-ζ' can be referred as the heated length. In the case of the sensor, heated length is a function of flow angle 'φ'. For φ=0^0, the heated length will be 'L', i.e., the thermal boundary layer will develop over the length of the heater line 'L'. In contrast, for φ=90^0, the heated length 'x' is the width of the heater line 'b' plus the thermal penetration depth (PD). It is known from Eqn. (SI.3.2) and the boundary layer theory that the average convection coefficient (h$_{conv}$) will decrease with increase in boundary layer thickness[333]. As (b+PD)<<L,

84

thermal boundary layer thickness will be small across the heater line. Thus, h_{conv} will be higher for the case $\varphi=90^0$, thus explaining the behavior in Fig. 3.3 (f).

SI 3.3. Supplementary Information: Use of In-phase 3ω Signal ($V_{3\omega, Ip}$) to Sense Contact, Thickness and Phase Change

Fig. S1.3.1 shows the use of $V_{3\omega, ip}$ to sense contact, thickness and phase change. The sensor is run in "dynamic" mode (i.e. at a single frequency as a function of time) to sense contact (Fig. S1. 3.1 (a) and phase change (Fig. SI.3.1 (c)). The sensitivity and response time is similar to that of out-phase signal discussed in the main paper. However, for thickness measurement (Fig. S1.3.1 (b)), the backside boundary is sensed at a lower frequency (~0.5 Hz) for in phase signal. In comparison, the backside boundary is sensed at a higher frequency (~0.7 Hz) for out of phase signal. Thus, out of phase signal has the potential for faster measurement.

4. A Micro-Thermal Sensor for Cryoablation Balloons

The following chapter is submitted for publication:

Natesan, H., Tian, L., Rogers, J., & Bischof, J. In submission to Journal for Biomechanical Engineering

4.1 Introduction

Thermal therapy is used to treat a variety of cardiovascular and cancer disease[1, 19, 271]. A major challenge with this therapy is delivering a precise and controlled thermal destruction to the target tissue while preventing damage to adjacent critical structures. Thermal therapy techniques such as radiofrequency (RF) and microwave (MW) depend on the ability of the probe to electrically couple to the tissue, which allows the probe to be monitored by electrical impedance measurements at the probe surface to indicate if the tissue has become too dehydrated for efficient electrical conduction (i.e. Joule heating) and/or dielectric heating[334]. While this can be useful in terms of modifying the probe conditions, it does not directly relate to the amount of tissue treated. On the other hand, cryoablation, which destroys tissue by freezing, can use imaging modalities such as ultrasound[328-330, 335-336], computed tomography[308, 337-338] and magnetic resonance imaging[322, 324-327] to visualize the entire cm scale frozen treatment zone. Unfortunately, this monitoring becomes ineffective when the characteristic size of the tissue approaches the limits of clinical imaging in thin issues (mm thick). Thus, there is an unmet need to efficiently monitor balloon-based therapies in thin vascular structures such as the PV for treatment of atrial AF affects millions of people every year. If left untreated, AF can contribute to the progression of further cardiovascular disease, stroke and even death. While some drugs can help control atrial fibrillation, they have side effects, and their efficacy is not uniform and often diminishes over time. Thus, the use of focal and especially thermal

interventions to electrically isolate the pulmonary vein (PV) thereby avoiding drugs is considered a milestone advancement in the treatment of AF[304, 339]. Specifically, thermal and cryoablation for PV isolation has been used for more than 20 years and has become a standard of care for drug-refractory paroxysmal atrial fibrillation[305, 339-345]. However, these treatments suffer from an inability to image or monitor the thermal therapy, leading to cases of over- and under-treatment. Indeed, over-treatment can lead to hemoptysis, esophageal freezing or phrenic nerve palsy[343, 346-347], and under-treatment requires repeat treatments[348-349]. Thus, as imaging cannot work on these thin mm-sized tissues, alternatives are urgently needed to improve monitoring of balloon-based thermal and focal therapy.

Monitoring at the surface of the probes can be achieved in a rudimentary way with thermocouples[350] or more robustly using thermal conductivity changes with micro-sensors based on the 3ω technique[47] modified for thin biological systems[45]. Fig. 4.1 (a, left) shows our original published embodiment of a 3ω sensor deposited on a flat substrate. This 3ω sensor can sense tissue or fluid contact, flow, mm-scale tissue thickness, and the initiation and completion of freezing , and it can be used to measure thermal conductivity (k) of thin (< 2 mm) biological tissues[45, 103]. It uses a sensor made up of a long, thin gold heater line (3 mm X 20 μm X 100 nm) deposited on a glass substrate. The biological tissue of interest is placed on top of the sensor such that it covers the heater line. An alternating current of frequency 'ω' excites the heater line, producing temperature oscillations of frequency '2ω' that propagate into the sample and the substrate over a thermal penetration depth, PD= $(\alpha/2\omega)^{0.5}$, where α is thermal diffusivity (m^2/s) and ω is the frequency of the applied electric current (radians). The resulting third harmonic voltage across the heater line '3ω' contains information about the temperature oscillations at the heater line. The temperature oscillations at the heater line can be used to calculate thermal conductivity of the sample with knowledge of the thermal and electrical properties of the sensor[47].

However, as cryoablation and other focal therapy in the PV is generally performed with balloons, there is a further need to integrate 3ω sensors onto balloons to perform the same sensing and monitoring functions. Recent advancements in flexible electronics now allow multiple types of

(a)

(b) *(c)*
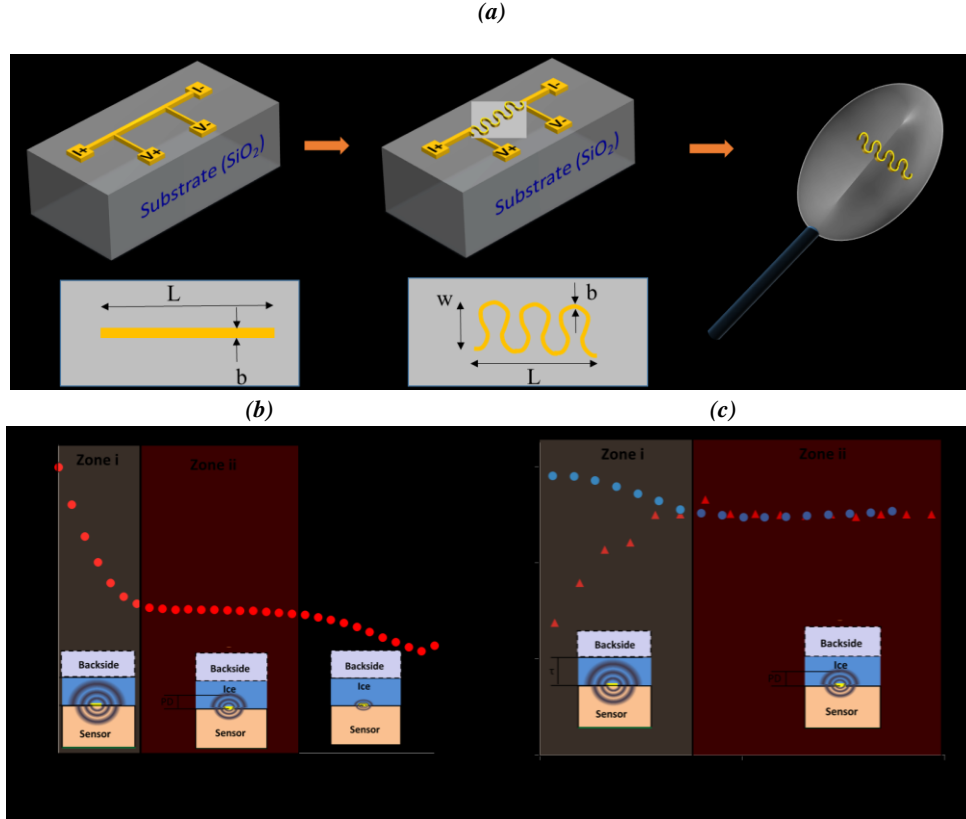
***Figure 4.1. Development of micro-thermal 3ω sensors for monitoring balloon cryoablation in pulmonary vein** (PV).(a) Development of a micro-thermal sensor starting from a linear sensor (L= 2 mm, b= 20 μm) on a flat substrate, to a serpentine sensor (L=0.5 mm, b= 5 μm, w= 180 μm). Finally, the serpentine sensor was integrated onto a balloon for focal therapy applications. (b) Historical data for a linear sensor shows $V_{3\omega, op}$ as a function of heater electrical frequency (ω/(2π)) where the sample is ice and the backside boundary is air. Zone i refers to the frequency range where PD ~t_{sample} . Zone iii refers to the range where PD ~t_{heater}; Zone ii refers to the range where $V_{3\omega, op}$ is neither affected by the heater line (PD>>t_{heater}) nor the backside boundary condition (PD<< t_{sample}). Inset schematic shows the comparison between PD and sample thickness, τ , for Zones i, ii, and iii. (c) Historical data for a linear sensor shows $V_{3\omega, op}$ (y-axis) at low frequencies in Zone i depends on a backside boundary for fixed sample thickness (τ ≈ 0.5 mm). Blue circle data represent the case where a backside of the sample is low k plastic (quasi-adiabatic), and red triangle data represents the case where the backside is high k copper at fixed temperature (quasi-isothermal). Inset schematic shows the comparison between PD and τ for Zones i and ii. Copyright pending for Fig. 4.1(b) and (c) from [103].*

sensors including 3ω sensors to be attached to flexible, stretchable substrates[315-318, 351-352]. The current collaborative effort now integrates 3ω sensors directly onto a balloon for monitoring thermal therapy. Example designs that integrate electronic sensors onto balloons[317-318, 352] and

human skin[316] have already been published. In the current work, we modify the linear 3ω sensor design from a thin straight line to a serpentine shape to enable its integration onto a flexible, stretchable balloon as shown in Fig. 4.1 (a). The serpentine shape minimizes local strains during inflation and deflation of the balloon as previously reported for other sensors[316-318, 351-352]. Hence, the modified sensor is first numerically analyzed using Finite Element Modeling on a flat substrate to determine the ability to differentiate between ice, water and fat. Further, the sensor was investigated for its ability to sense thickness and phase change for ice and water respectively. Next, these results were confirmed experimentally to sense tissue contact, thickness and phase change. Finally, we microfabricated the sensor onto a flexible, stretchable balloon using transfer printing techniques (Fig. 4.1 (a))[317]. The sensor on a balloon was then tested to sense contact, thickness and phase change for possible cryotherapy (or other thermal therapy) application.

4.2 Methods

4.2.1. Numerical characterization of the serpentine 3ω sensor on a flat substrate

i. Principle of 3ω sensor

The historical operation of the linear 3ω sensor is shown in Figs 1 (b) and (c). Fig. 4.1 (b) shows an instance where the sensor was used to measure the thickness of ice (1 mm thick) with air as a backside boundary condition. The plot shows the output signal (i.e., third harmonic voltage ($V_{3\omega, op}$)) across the heater line measured as a function of frequency. The frequency range is divided into three zones (see inset): Zone i refers to the lower frequency range where PD ~ t_{sample} (sample thickness) while Zone iii refers to the frequency range where PD ~ $t_{heater\ line}$ (thickness of the heater line). Zone ii refers to a specific frequency range where $t_{heater\ line} >> PD << t_{sample}$. This frequency range is characterized by a constant $V_{3\omega,\ op\ avg}$, which is inversely proportional to effective thermal

conductivity of the region in the sample and the substrate traversed by the temperature oscillations k_{total} (W/m.k). In fact, it can be determined as shown in Eqn. (4.1):

$$k_{total} = \frac{\alpha R^2 I^3}{8 L V_{3\omega,op\ avg.}},$$ (4.1)

Where R and L are the resistance [Ω] and length of the heater line [L] respectively; I is the electric current applied across the heater line [A]; and $V_{3\omega,\ op\ avg.}$ is the resulting average third harmonic out-of-phase voltage [V] measured from Zone ii of the frequency sweep. Finally, the thermal conductivity of the sample can be determined from k_{total} using Eqn. (4.2)[45] if thermal conductivity of the substrate k_{sub} is known beforehand from calibration:

$$k_{total} = k_{sample} + k_{sub}$$ (4.2)

An important feature of the 3ω sensor is that the frequency-dependent measurement enables sub-surface sensing of k_{sample} based on the behavior of $V_{3\omega,\ op}$ in Zone ii. In Zone i, where PD~t_{sample}, the behavior of $V_{3\omega,\ op}$ becomes dependent, not only on k_{sample} but also on t_{sample}, and the backside boundary condition of the sample[320]. This is shown using a representative experiment where the sensor measured ice of 0.5 mm thickness with a varying backside boundary of quasi-thermal copper vs. quasi-adiabatic plastic (see Fig. 4.1 (c)). Results for thicker ice (0.5- 2mm) with quasi-adiabatic air as backside boundary conditions is shown in a previously reported work[103]. Using these principles, the 3ω sensor on flat and balloon substrates has been used to sense contact with fluid vs. tissue, thickness and freezing phase change.

ii. Numerical model of 3ω sensor

Mishra et al. developed a 2-D axisymmetric finite element model of a thin and infinitely long heater line on a flat substrate[353]. We extend this model here into 3D for the heater line that is serpentine, but still attached like the linear line onto a flat substrate. A commercially available COMSOL

90

package (Version 5.0) was used to simulate the sensor as a quasi-steady model with the governing equation as shown below,

$$k \left[\frac{\partial^2 T}{\partial x^2} + \frac{\partial^2 T}{\partial y^2} + \frac{\partial^2 T}{\partial z^2} \right] + P' e^{i2\omega t} \delta(x, y, z) = CT \qquad (4.3)$$

where P', T and C refer to the heater line power per unit length [W/m], average temperature oscillations in the heater line [K], and volumetric heat capacity of the surrounding medium (substrate/ sample) [J/m^3/K] respectively. The partial differential equation (PDE) in Eqn. (4.3) is set up using coefficient form PDE module. Contact resistance between the heater line and the substrate were assumed to be negligible[45]. The heater line was modeled as a heat source at the surface of the heater line i.e., negligible thickness. The thickness is neglected as the PD (~10 μm at 100 Hz for water at 22^0C) >> heater line thickness (<100 nm) for frequencies of interest in biologically relevant materials. The model was validated with closed form analytical solution for linear sensor and also with experimental data for a serpentine heater line on a glass substrate as shown in SI 4.1. Specifically, a gold serpentine sensor of dimensions b = 5 μm, w = 180 μm, and L = 0.5 mm is modeled on a flat glass substrate of (length= 5 mm, width= 5 mm, thickness=1 mm). The backside boundary condition for the experiment was air i.e., quasi- adiabatic which would approximate the interior of an inflated balloon.

Using the numerical model, we first investigated the ability of the sensor to identify ice (k=2.45 W/m.K, α=1.33E-6 m^2/s), water (k=0.6 W/m.K, α=1.43E-7 m^2/s) and fat (k=0.2 W/m.K, α=1.39E-7 m^2/s) at a frequency of 2 Hz, which is in the mid frequency range of Zone ii for all the three samples. The heater line was modeled to be on a 2 mm thick glass substrate (k= 1.26 W/m.K; α=6.6E-7 m^2/s) and in contact with the sample of 2 mm thickness. Contact resistance between the substrate, the heater line and the sample were assumed to be negligible. The backside of the sample

91

and the substrate were assumed to be under adiabatic conditions. The heater electrical power applied to the heater line was assumed to be 5 mW, which is approximately equal to the heater input power for the serpentine sensor used in this paper for an input current of ~10 mA. Next, the ability of the serpentine sensor to measure thickness was investigated. For thickness, the sensor was modeled to be in contact with ice with water or fat as backside boundary conditions in the thickness range of 0.5- 2 mm range. The resulting $V_{3\omega, op}$ is determined at 0.1 Hz and plotted as a function of thickness of the sample. The frequency of 0.1 Hz is chosen as the PD (~0.33 mm in fat, ~0.34 mm in water, ~1.03 mm in ice) is comparable to the thickness of 0.5 – 2 mm for PV and lies in Zone i (low frequency range).

Finally, we investigated the ability of the sensor to sense phase change from water to ice. This is achieved by first modeling the serpentine sensor to be in contact with water with an adiabatic backside boundary condition. Next, $V_{3\omega, op}$ at 2 Hz is determined and plotted as a function of t_{ice}/t_{water} by changing the thickness of ice (i.e. ice front is advancing next to the sensor). The frequency of 2 Hz is chosen as the PD is ~0.074 mm for fat, ~0.075 mm for water, 0.23 mm for ice, which is an order of magnitude less than the thickness of 2 mm that we wish to sense within PV and lies in Zone ii of both ice and water.

4.2.2. Micro-thermal sensing using the serpentine sensor on a flat substrate

i. Construction of the serpentine sensor

A gold serpentine shaped heater line (L=0.5 mm, b=5 μm, w= 180 μm, t= 80 nm) is patterned onto a 1 mm thick silica glass (amorphous SiO_2) substrate using standard photolithography and lift off techniques. A chromium layer (~5 nm thick) is used as an adhesion to bond gold line onto glass substrate. A polystyrene dielectric layer (~1 μm thick) is deposited on top of the heater line. The process is detailed elsewhere[103]. The glass substrate is attached on top of another silica glass

substrate (1 mm thick). The heater lines are connected to the signal processing unit using copper wires.

ii. Data acquisition from the 3ω sensor

The sensor is excited with an alternating current produced at a fixed frequency by a custom voltage to current circuit. This input current is driven by the reference output of a lock-in amplifier (SR 830, Stanford Research Systems). The frequency of the input current can be controlled using the lock-in amplifier. The output signal from the sensor comprises a 1ω and a 3ω component, which is separated using a multiplying digital-to-analog converter. The lock-in amplifier was then used to record the $V_{1\omega}$ and $V_{3\omega}$ signal. The amplifier can be adjusted for optimum time constant (response time) and voltage sensitivity in the output signal.

iii. Sensing contact

Our experimental setup consists of a supported 3ω sensor with a serpentine-shaped heater line (L=0.5 mm, b=5 μm, w= 180 μm, t= 80 nm), a piece of tissue and a variable speed peristaltic pump (Cole-Parmer Masterflex®) used to control flow over the sensor. To verify our ability to sense probe contact, we used the sensor to differentiate between tissue contact and flow conditions. Here the tissue was a mouse liver immersed in phosphate buffer solution and stored in a $4\,^0C$ refrigerator. All biological tissues were used for experiments within 24 hours of harvesting animals used for other purposes. For sensing water flow, the peristaltic pump was used to control water flow over the sensor at a certain speed. For sensing tissue contact, the mouse liver was manually placed on top of the sensor, thereby blocking the water flow. The sensor recorded the $V_{3\omega,\ op}$ at a fixed frequency of 10.1 Hz (constant PD) and input RMS current of 10 mA. A lock-in time constant of 3 s was selected as a compromise between measurement noise and time response of the measurement system. The chosen frequency is a typical value for which PD (~0.034 mm for mouse

liver) $\ll t_{sample}$ (~2 mm).

iv. Sensing tissue thickness

Agargel (0.5% weight of agarose in water) was placed on the sensor and immediately frozen to - 25 ^{0}C using a cooler enclosed in a cryofreezer (Planer Kryo 10 Series III). For an input RMS current of 10 mA, $V_{3\omega, op}$ was recorded as a function of frequency (from 0.1 to 10 Hz) at a fixed temperature of -25 ^{0}C on the sensor surface. The experiment was repeated for a different thickness (n = 3) of frozen agargel (i.e., changed from ~0.5 mm to ~1.9 mm) while keeping the backside boundary condition as air (k_{air}~ 0.02 W/m.K) at -55 ^{0}C [321]. The thermal convection effects of air can be assumed negligible as the convection heat loss is <1% of the conduction heat flow from the heater line if convection coefficient is assumed to be <25 $W/m^2.K$[320].

v. Sensing phase change

A 3 mm thick, several cm long mouse liver slice was placed on the sensor. The temperature was lowered from 20 ^{0}C to -10 ^{0}C, allowing the tissue sample to become frozen. After allowing the freezing event to complete and the voltage to stabilize, the temperature was increased back to 20 ^{0}C. Completion of freezing and thawing events were verified by visual inspection during the experiment. An alternating current with an RMS of 10 mA at a frequency of 10.1 Hz, which is in the Zone ii of the frequency sweep was applied across the sensor and the results were recorded with a lock-in time constant of 3 s.

4.2.3. Micro-thermal sensing using serpentine sensors on a balloon substrate

i. Integration of serpentine 3ω sensor onto a balloon

The 3ω sensors were deposited on flexible balloons[316-318, 352]. Specifically, the 3ω sensors and associated interconnects/contacts were microfabricated on silicon wafers using conventional

microfabrication techniques. An initial sacrificial layer of poly(methyl methacrylate) spun onto the wafer allowed eventual release of the entire 3ω device from the wafer. Elastomeric transfer printing techniques were then used to transfer the device from the wafer to a balloon surface. The device contains gold lines, deposited by electron-beam evaporation and interconnects by photolithography, fully encapsulated in thin layers of polyimide (spin cast). Careful design of the polyimide geometries provided the required mechanical robustness (to withstand the pressure of the balloon) as well as encapsulation from surrounding fluids as previously described for other flexible electronic constructs[315-318].

ii. Sensing contact

The following experiments were conducted using a 3ω sensor of serpentine shaped heater line (L=0.5 mm, b=5 μm) integrated onto a balloon. To verify our ability to sense probe contact, we used a sensor integrated onto a balloon to differentiate between contact with agargel and air. The balloon was positioned a few mm away from the agargel (2 mm thick), which in turn was placed on a copper plate at room temperature (~22 ^{0}C). The sensor recorded the $V_{3\omega, op}$ at a fixed frequency of 11.1 Hz (constant PD) and input RMS current of 6 mA. A lock-in time constant of 3 s was selected as a compromise between measurement noise and time response of the measurement system. The chosen frequency is a typical value for which PD (~0.032 mm for agargel) << t_{sample} (Zone ii) as the purpose is to sense the tissue that is in immediate contact with the sensor. The balloon was moved so that the sensor came in contact with the agargel.

iii. Sensing tissue thickness

A copper plate was positioned inside a cryofreezer (Planer Kryo 10 Series III) equilibrated to -25 ^{0}C. Agargel (0.5% weight of agarose in water) was placed on the copper plate (5 mm thick) at -25 ^{0}C and immediately frozen. Next, for an input RMS current of 6 mA, $V_{3\omega, op}$ was recorded at 0.1 Hz

95

at a fixed temperature of -25 ^{0}C on the sensor surface. Here, the chosen frequency is a typical value for which PD ~ t_{sample} as the purpose is to sense the backside of the sample in contact with the sensor. The experiment was repeated for different thickness of frozen agargel (i.e., changed from ~0.5 mm to ~2.0 mm) while keeping the backside boundary condition as copper (k_{copper} ~386 W/m.K)[333].

iv. Sensing phase change

A 3 mm thick sample of agargel was placed on the copper plate at 20 ^{0}C. The sensor on the balloon was brought in contact with the top surface of the agargel. The temperature of the copper plate was lowered from 20 ^{0}C to -25 ^{0}C, freezing the agargel sample. After the cooling process is complete and followed by voltage stabilization, the temperature was increased back to 20 ^{0}C. An alternating current with an RMS of 6 mA at a frequency of 11.1 Hz, which is in the Zone ii of the frequency sweep was applied across the sensor.

4.3. Results and Discussion

4.3.1. Numerical characterization of serpentine 3ω sensors on a flat substrate

The 3ω sensors had to be modified from a linear into a serpentine shape for deposition onto a balloon substrate. However, the serpentine shape changes the behavior of sensor output signal, $V_{3\omega,op}$ as a function of frequency. So, a numerical model as shown in Fig. 4.2 (a) was created to confirm

(a)

(b)

(c)

(d)
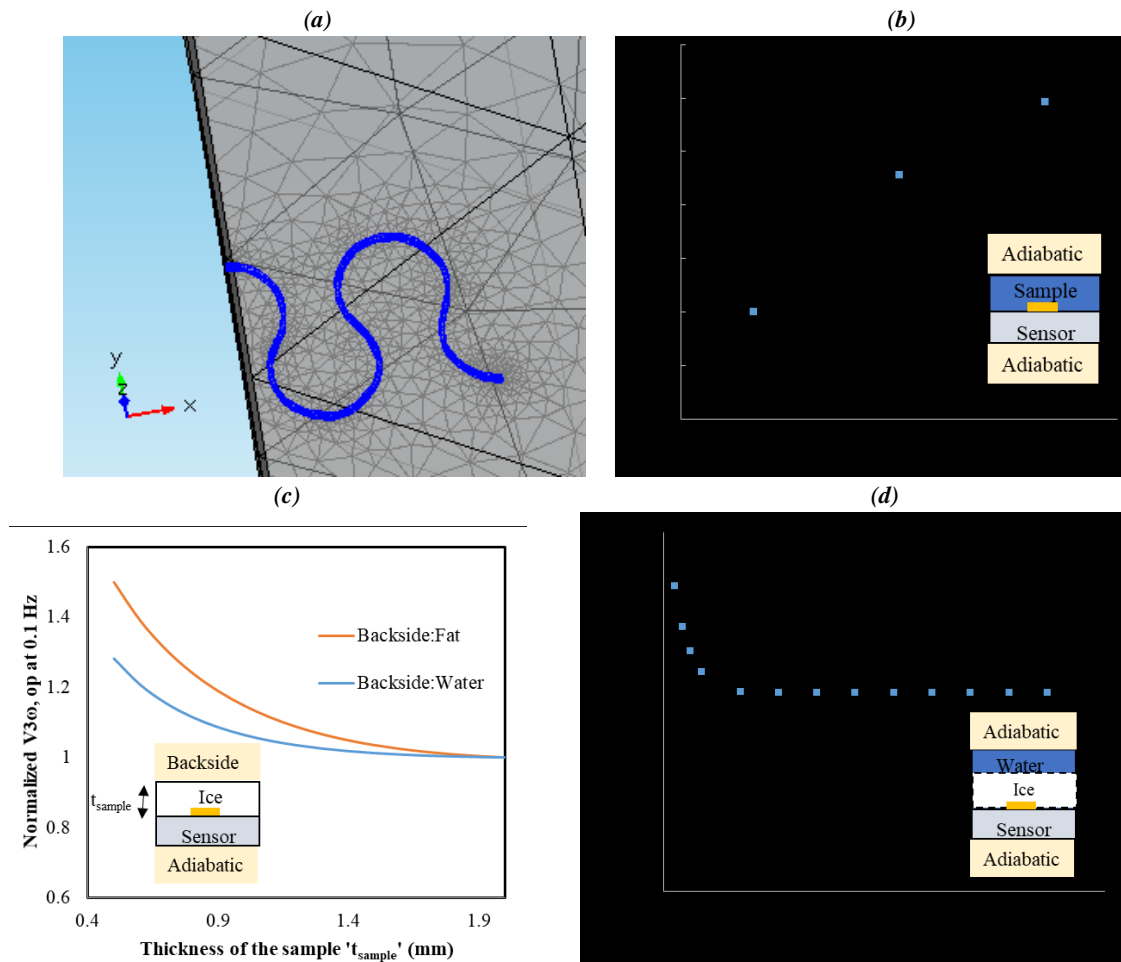
Figure 4.2 Finite element analysis of the serpentine sensor (L=0.5 mm, b= 5 µm, w= 180 µm) on a flat substrate. *(a) 3D numerical discretization of the serpentine sensor on a flat 2 mm thick glass substrate. (b) Measurement predictions of $V_{3\omega,op}$ at 2 Hz for different samples of ice, water and fat in contact with the sensor. $V_{3\omega,op}$ is normalized to the values of ice (c) Measurement predictions of $V_{3\omega,op}$ at 0.1 Hz for varying sample thickness of ice with water or fat on the backside. $V_{3\omega,op}$ for each configuration is normalized to the values for samples at 2 mm thickness (d) Measurement predictions of $V_{3\omega,op}$ at 2 Hz for varying thickness of ice as ice front moves from the sensor. $V_{3\omega,op}$ is normalized to the PD in ice*

the ability of the serpentine shaped sensor for micro-thermal sensing. First, the ability of the sensor

to differentiate between biologically relevant materials such as fat, water and ice is shown in Fig.

4.2 (b). Here, $V_{3\omega, op}$ is determined for cases where the sample was in contact with fat, water and

ice. $V_{3\omega, op}$ was normalized with $V_{3\omega, op}$ obtained for ice (k=2.45 W/m.K). The value increases to

~2.3 for water with k=0.6 W/m.K and ~3.0 for fat with k=0.2 W/m.K. The reason $V_{3\omega, op}$ increases

Figure 4.3 Micro-thermal sensing using a serpentine shaped sensor (L= 0.5 mm, b= 5 μm, w= 180 μm, t= 100 nm) on a flat substrate. (a) Serpentine-shaped sensor on a flat glass substrate (b) (Contact) Experimental measurement of water vs. tissue contact; $V_{3\omega,op}$ is measured at ω of 10.1 Hz. (c) (Thickness) Experimental measurement of $V_{3\omega,op}$ at 0.1 Hz for different thickness of frozen agargel at -25 ^{0}C (AVG ± STDEV of N = 3). Black line shows the results from the numerical model. The backside boundary conditions are air and modeled as adiabatic conditions. $V_{3\omega,op}$ is normalized to tis value for 0.5 mm thick sample. Inset shows experimental measurement of $V_{3\omega,op}$ as a function of frequency for different sample thickness. (d) (Phase Change) Experimental measurement of $V_{3\omega,op}$ during mouse liver freezing at 10.1 Hz and normalized to its initial value at 0 s. Cooling begins at ~30 s and thawing begins at ~140 s.

with drop in thermal conductivity could be explained by Eqns. (4.1) and (4.2). For the same sensor (substrate and heater line geometry) and input electrical current, $V_{3\omega, op}$ measured at a frequency in Zone ii i.e. 2 Hz, is inversely proportional to thermal conductivity. Thus, if the sensor and input current remain the same, the sensor can be used to sense contact with different materials through $V_{3\omega, op}$.

Next, the ability of the sensor to sense thickness of materials such as water and ice with different boundary conditions was modeled as shown in Fig. 4.2 (c). Here, $V_{3\omega, op}$ is normalized for each case with the value determined at 2 mm. For the case with ice as sample and fat as backside, normalized $V_{3\omega, op}$ increases to ~1.03 for 1.5 mm thick sample, ~1.15 for 1 mm thick sample, and finally ~1.50 for 0.5 mm thick sample. In contrast, for the case with water as backside boundary, the normalized $V_{3\omega, op}$ increases to ~1.01 for 1.5 mm thick sample, ~1.06 for 1 mm thick sample, and finally ~1.28 for 0.5 mm thick sample. If the noise in the signal is less than 1%, the sensor can be reliably used to sense thickness even up to 2 mm for ice with fat as backside boundary.

Finally, the ability of the sensor to track ice thickness in water is shown in Fig. 4.2 (d). Here, the sensor is modeled to be in contact with water while an ice front moves away from the sensor. It has to be noted that latent heat was neglected for these simulations. $V_{3\omega, op}$ is determined at 2 Hz as it is in Zone ii and scales with t_{sample} and is independent of backside boundary conditions. $V_{3\omega, op}$ is normalized to the PD in ice. As the thickness ratio (t_{ice}/PD) increases to 1.73, normalized $V_{3\omega, op}$ decreases to ~1 beyond which there is a plateau in the signal. This sharp drop in the signal is due to the fact that the thermal conductivity of ice is at 2.45 W/m.K, which is ~4 times that of water at 0.6 W/m.K thereby confirming the ability of the sensor to measure a phase change event.

While the sensor operates as desired, the original ability of the 3ω sensor to measure k_{sample} of materials such as ice, water and fat using $V_{3\omega,op}$ in Eqn. (4.1) will be degraded. More specifically,

99

the current form factor of the serpentine shaped heater line introduces errors while using Eqn. (4.1) as it was originally derived for linear sensors. The error can be minimized by changing the form factor as explained in SI 4.2, however, thermal conductivity errors with the current form factor to measure ice can be as high as 115%. Alternatively, Finite Element Analysis can be used to back calculate thermal conductivity if sufficient output third harmonic voltage is available as a function of frequency for comparison[351].

As the sensor would eventually be integrated onto a balloon substrate, the effect of size of the balloon (i.e., radius of curvature) on the sensor performance was investigated in SI.4.2. The error in $V_{3\omega, op}$ over a wide frequency range of 0.1 to 1000 Hz and k_{sample} is found to be negligible for the
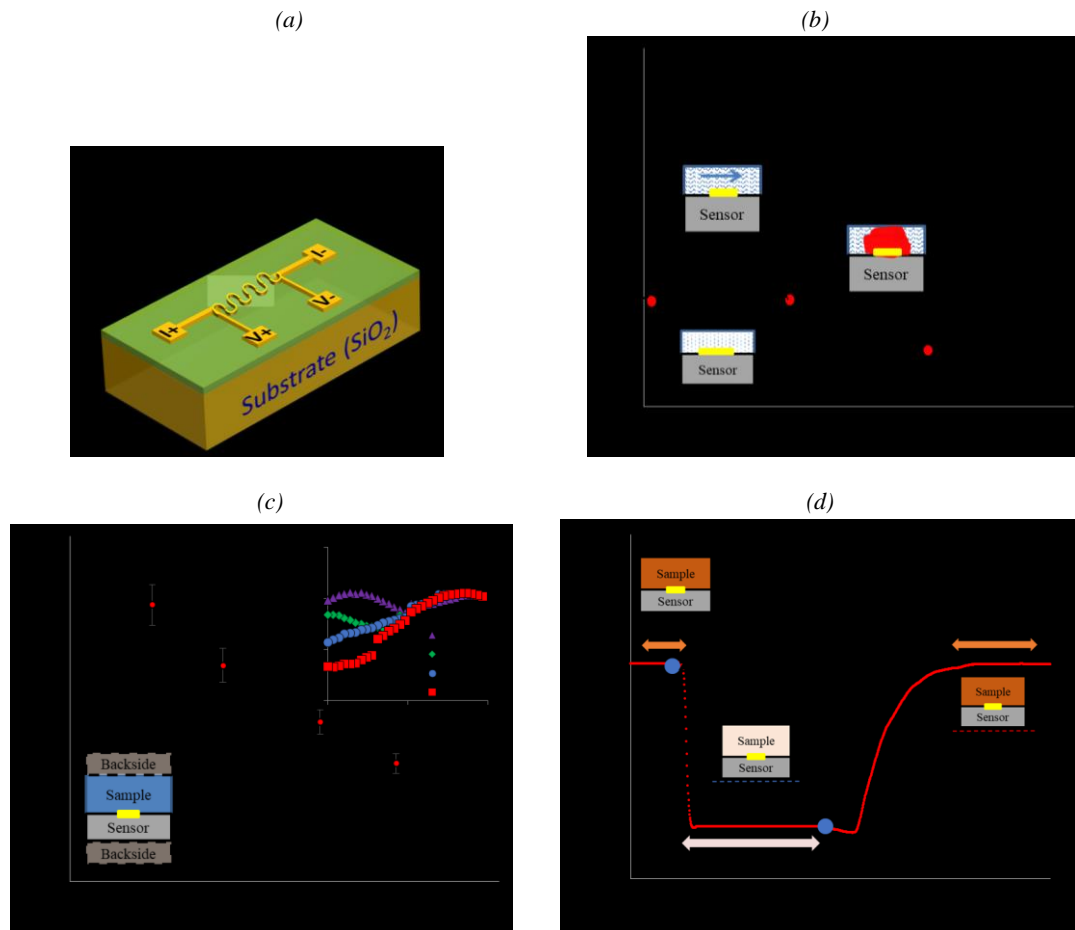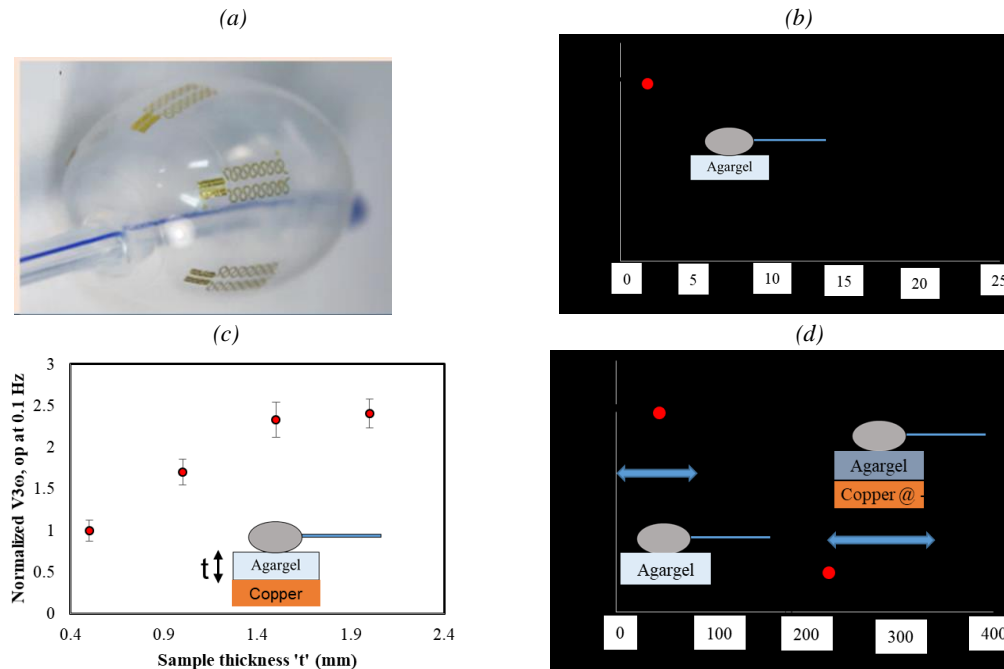

***Figure 4.4. Micro-thermal sensing using serpentine shaped sensor (L= 0.5 mm, b= 5 µm, w= 180 µm, t= 100 nm) on a balloon substrate.** (a) 3ω sensor deposited on a balloon (b) (Contact) Experimental measurement of $V_{3\omega,op}$ as a function of time at 11.1 Hz heater electrical frequency. The sensor is brought in contact with agargel at ~2 s and $V_{3\omega,op}$ is normalized to its initial value recorded in air (c) (Thickness) Experimental measurement of $V_{3\omega,op}$ as a function of sample thickness 'd' measured at ω of 0.1 Hz (AVG ± STDEV of N = 3). $V_{3\omega,op}$ is normalized to tis value for 0.5 mm thick sample (d) (Phase Change) Experimental measurement of $V_{3\omega,op}$ at 11.1 Hz and normalized to its initial value when the sensor is in contact with agargel. Cooling begins at ~90 s and ends at ~240 s.*

current application, where the heater line on the balloon will bend around a radius equal to the ostium of the pulmonary vein (~4 to 6 mm)[354].

4.3.2. Micro-thermal sensing using the serpentine sensor on a flat substrate

After construction of the serpentine 3ω sensor on a flat, glass substrate as shown in Fig. 4.3 (a) a number of specific experimental measurements were undertaken. First, we used the sensor to differentiate between tissue contact and flow conditions as shown in Fig. 4.3 (b). Here the 3ω voltage ($V_{3\omega, op}$) is shown to be constant as the water is at rest and then rises at ~28 s due to flow and concomitant convective heat loss. At 50 s, the plot shows that placing a piece of low k tissue (1 mm thick mouse liver) on top of the sensor replaces water flow with tissue contact thereby increasing $V_{3\omega, op}$ to the highest value of all cases. Fig. 4.3 (c) shows $V_{3\omega, op}$ at 0.1 Hz as a function of sample thickness normalized to its value for 0.5 mm thick sample. The black line represents the results from numerical modeling of the sensor in contact with frozen agargel. The inset figure shows normalized $V_{3\omega, op}$ as a function of frequency for varying sample thickness. At high frequencies, the thermal penetration depth (PD = $(\alpha/2\omega)^{0.5}$) is small and stays within the sample as depicted in the inset. However, at lower frequencies, the penetration depth can increase to become comparable to the sample thickness. More specifically, the $V_{3\omega, op}$ response at 0.1 Hz decreases with increasing thickness (0.5 to 2 mm). Finally, the ability to sense phase change was verified by monitoring $V_{3\omega, op}$ during freezing and thawing of a mouse liver placed on top of the sensor as shown in Fig. 4.3 (d). The temperature of the stage below the sensor was changed to -25 ^{0}C at ~30 s, after which there was a drop in $V_{3\omega, op}$. This drop corresponds to the jump in k for biological tissues on freezing and is followed by a stable region where the sample is completely frozen. After ~140 s, the temperature of the stage is set to 15 ^{0}C, resulting in increase in $V_{3\omega, op}$.

4.3.3. Integration of serpentine 3ω sensor onto a balloon

Linear 3ω sensors (Fig. 4.1 (a)) have been used to sense contact with tissue vs water, thickness and phase change[103]. However, this linear heater line sensor cannot be integrated onto a flexible, stretchable substrate such as a cryoballoon as it fractures under the large deformations needed to inflate the balloon. Hence, we modified the heater line into a serpentine shape that allows in- and out-of-plane buckling motion under large deformations. Such 3ω sensors have been previously developed to measure thermal conductivity on the surface of human skin[351]. The sensors shown in Fig. 4.4 (a) involve a small Au heater with b= 5 μm, width w= 180 μm, and length L= 0.5 mm and a similarly shaped pair of PI encapsulation layers with widths of 20 µm. An overall layout in the form of a filamentary serpentine structure provides elastic stretchability of 54% and 71% in the horizontal and vertical directions, respectively, as computed by numerical analysis with a threshold for Au plastic deformation of 0.3%[351]

4.3.4. Micro-thermal sensing using serpentine sensors on a balloon substrate

In Fig. 4.4 (a), the serpentine sensor is deployed on a balloon to sense contact, thickness and phase change. Fig. 4.4 (b) shows 3ω voltage at rest and then the response at ~ 2 s when it is brought in contact with agargel (0.5% weight of agarose in water) which results in an immediate drop in $V_{3\omega, op}$ due to high k for agargel vs. air. Next, to verify our ability to measure thickness, we prepared several samples of thin frozen agargel of varying thickness and recorded the 3ω signal at 0.1 Hz (Fig. 4.4 (c)). $V_{3\omega, op}$ at 0.1 Hz (which has a PD ~ 2 mm in ice) increases as a function of thickness (0.5 to 2 mm). In contrast, $V_{3\omega, op}$ at 0.1 Hz decreased with increase with thickness for the flat substrate. This difference is due to the fact that the backside boundary condition for the balloon experiments is highly conductive copper plate while that of flat substrate experiments is highly insulating air (k= 0.02 W/m.K). Finally, we used the sensor to monitor freezing of agargel through

102

its effect on the 3ω voltage as shown in Fig. 4.4 (d). $V_{3\omega,\,op}$ is normalized with respect to its initial value where the agargel is not frozen. Here the temperature of the copper plate below the sample was changed to -25 ^{0}C at ~90 s after which there was a drop in $V_{3\omega,\,op}$. This drop corresponds to the jump in k for agargel on freezing and is followed by a region where the sample is completely frozen.

4.4 Summary

In summary, we have shown how to modify a linear 3ω sensor for use on a balloon using a serpentine heater line and flexible electronic approaches (Fig. 4.1). First, we numerically studied the behavior of the serpentine sensor on a flat substrate for different materials of varying thickness (Fig. 4.2). Then, we explored the error introduced by curvature of the substrate (SI 4.2). Next, we

Table 4.1. Summary of measurement parameters used to record 3ω signal ($V_{3\omega,\,op}$) from the 3ω sensor using a lock-in amplifier

Characteristics of the sensor		Linear sensor on flat substrate	Serpentine sensor on flat substrate	Serpentine sensor on balloon
Data discused		Figure 3.2 and 3.3 from [103]	Figure 4.3	Figure 4.4
Size of the heater line		L= 2 mm, b= 20 μm, t= 100 nm	L= 0.5 mm, b= 5 μm, w= 180 μm, t= 100 nm	L= 0.5 mm, b= 5 μm, w= 180 μm, t= 100 nm
Substrate		Glass (~1 mm thick)	Glass (~1 mm thick)	Polyurethane balloon (~0.1 mm thick)
Contact	**Measurement**	Water vs. Mouse liver tissue	Water vs. Mouse liver tissue	Air vs. Agargel
	Response time^	1 second	3 seconds	3 seconds
Thickness	**Measurement**	Agargel: 0.5 – 2.0 mm thick	Agargel: 0.5 – 1.9 mm thick	Agargel: 0.5 – 2.0 mm thick
	Waiting time^^	15 minutes	15 minutes	15 minutes
Phase	**Measurement**	Freezing and thawing of mouse liver and agargel	Freezing and thawing of mouse liver	Freezing and thawing of agargel
	Response time^	1 second	3 seconds	3 seconds

^Response time (RT) refers to the time constant used for the lock-in amplifier during the measurement. ^^Waiting time refers to the time waited before voltage stabilization (<1% noise), which was ~30*RT

show experimental measurements of serpentine sensors on flat substrates for sensing contact, thickness and phase change within thin biological tissues at the limit of resolution of clinical imaging, 0.5 – 2 mm (Fig. 4.3). Finally, we demonstrate experimental proof of principle that we can integrate the sensor onto a balloon and make similar measurements (Fig. 4.4). A summary of these experimental results is tabulated in Table 4.1. The response time refers to the parameter used by the lock-in amplifier during the measurement. The response time for contact and phase change measurement is on the order of 1-3 seconds, while the waiting time for thickness measurement was 15 minutes. As thickness measurements were made at a low frequency of 0.1 Hz, a long waiting time was necessary to acquire a reliable signal. In future, the frequency of measurement could be optimized in order to reduce the sampling time.

In addition to improving balloon-based thermal or focal treatment in PV as envisioned here, the new thin, flexible sensor could be used on other probes or balloons for monitoring thermal (heat or cold) focal therapy in peripheral artery disease, renal or hepatic artery treatments (hypertension and diabetes) in the future. Conceivably these sensors can also be used on balloons using a non-thermal ablation technique (such as irreversible electroporation) for accurate placement of electrodes to achieve a desired ablation zone[355-356].

4.5. Specific Acknowledgements

SI 4.1. Supplementary Information: Validation of the Numerical Model

The numerical model was first validated through comparison with a closed form analytical solution for a linear sensor(L=50 mm, b= 30 μm) on a flat substrate (k= 1 W/m.K, α=1E-6 m^2/s)[91]. The deviation of $V_{3\omega, op}$ of the FEM model from the analytical model is calculated as a function of frequency and plotted as shown in Fig. SI.4.1 (a). It can be seen that the error decreases with increase in frequency and is in general less than 2%.

Next, the numerical model for serpentine sensors is validated through comparison with experimental measurement of the serpentine sensor on glass substrate. Using the numerical model, temperature rise is determined as a function of frequency specifically at 4 values of 0.1, 1, 10, 100 Hz. $V_{3\omega, op}$ is determined from the temperature rise using the Eqn. (SI.4.1)[46, 312]

$$V_{3\omega,op} = -\frac{1}{2} * \alpha_T * I * R * Img(T) \qquad (SI.4.1)$$

where α_T- temperature coefficient of resistance (/^{0}C), I- electrical input current (A), R- electrical resistance (Ω), Img(T)- imaginary part of the complex temperature response determined from the numerical model (^{0}C). For an input current of ~10 mA, $V_{3\omega, op}$ is determined for varying thermal conductivity (k) and thermal diffusivity (α) of the substrate at four frequencies of 0.1 Hz, ~1 HZ, ~10 Hz, ~100 Hz and the resulting RMS deviation of the data from the model is calculated from Eqn. (SI.4.2) for each case and plotted as shown in Fig. SI.4.1 (b).

$$Error\ (\%) = \left[\frac{1}{4}\Sigma\left(\frac{V_{3\omega,op,calc}-V_{3\omega,op,measured}}{V_{3\omega,op,measured}}\right)^2\right]^{0.5} \qquad (SI.4.2)$$

The error is found to be minimal for k= 1.26±0.1 W/m.K, α=6.6E-7±0.5E-7 m^2/s (N=3), which is close to the values in literature[47].

(a)   *(b)*
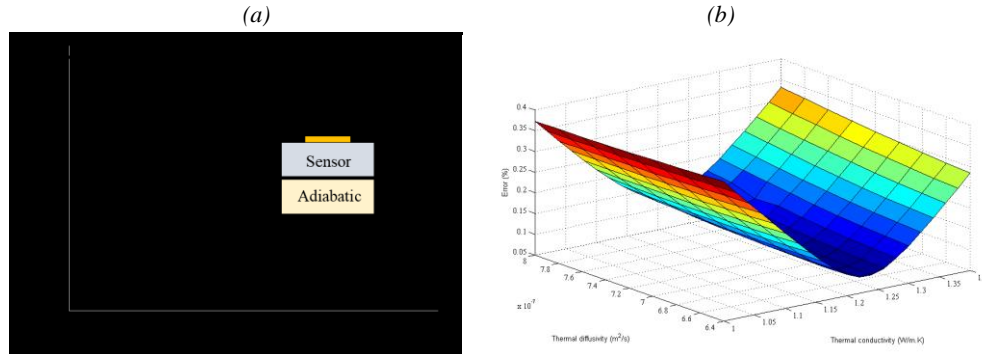
Figure SI.4.1. Validation of the numerical model. *(a) (Theoretical validation) Plot of error in imaginary part of the complex temperature rise (Img (T)) determined from the numerical model in comparison with the closed form analytical solution. A linear sensor (L=50 mm, b=30μm) is modeled to be on a glass substrate (k= 1 W/m.K, α=1E-6 m²/s) and subjected to an input power of 5 W. (b) (Experimental validation) 3D plot of error in calculating $V_{3\omega,\ op}$ as a function of k and α. A serpentine sensor (L=0.5 mm, b= 5 μm, w= 180 μm) is modeled to be on a flat glass substrate (2 mm thick). The error is found to be minimal at % for k=1.26± 0.1 W/m.K , α=6.6E-7±0.5E-7 m²/s*

SI 4.2. Supplementary Information: Error in Thermal Conductivity of Serpentine Sensors

In order to determine the error, a numerical model of the curved sensor was developed using COMSOL to numerically determine $V_{3\omega,\ op}$ as a function of frequency. Substituting the value in Eqns. 4.1 and 4.2, numerically calculated thermal conductivity k_{calc} was determined and can be compared to the thermal conductivity used in the model k_{actual} to assess error. Then, the error can be determined from using Eqn. (SI.4.3),

$$k_{error}\ (\%) = 100 * \left(\frac{k_{calc} - k_{actual}}{k_{actual}}\right) \tag{SI.4.3}$$

First, the effect of form factor of the serpentine sensor on the k_{error} of the serpentine sensor on a flat substrate is investigated. The form factor was changed by changing the aspect ratio of the heater line. This was achieved by keeping the dimensions of the sensor such as L= 3 mm, b= 20 μm, t= 100 nm as constants while changing w. The heater line was modeled to be on a glass substrate (2 mm thick) and in contact with ice (2 mm thick). The backside boundary conditions of the sample and the substrate were assumed to be adiabatic. Fig. SI.4.2 (a) shows that the error decreases with increase in the aspect ratio (AR) of the heater line (L/w).

106
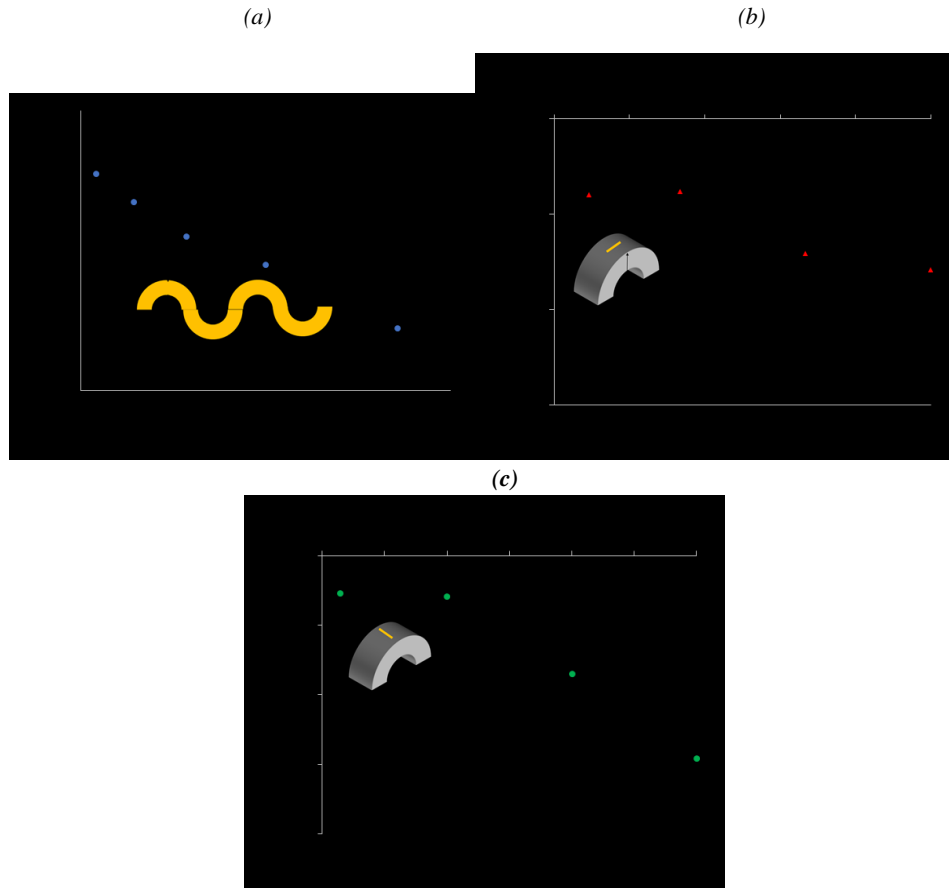
Figure SI.4.2. Finite element analysis of the effect of heater line and substrate geometry on the error in thermal conductivity. (a)Plot of k_{error} as a function of AR of the heater line (L= 3 mm, w= variable, b= 20 µm, t= 100 nm). AR= inf represents the case where w=0 and hence a linear heater line (b) Plot of k_{error} for a linear sensor on a varying radius of the curved substrate (L= 3 mm, w=0 µm, b= 20 µm, t= 100 nm) with the sensor parallel to the substrate. Inset shows the parallel orientation of the sensor. (c) Plot of k_{error} for a linear sensor on a varying radius of the curved substrate (L= 3 mm, w=0 µm, b= 20 µm, t= 100 nm) with the sensor perpendicular to the substrate. The results are for two orientations of the linear sensor. Inset shows the perpendicular orientation of the sensor. The curvature of the substrate introduces negligible error.

Next, we investigated the effect of size of the balloon i.e., substrate curvature on the performance of the sensor. This is achieved by determined error from Eqn. (SI.4.3) in measuring thermal conductivity of ice for a linear sensor (L= 3 mm, b= 20 µm, t= 100 nm) on a curved substrate and compared with that of the flat substrate. The reason for using a linear sensor for this particular case is to simplify the numerical model and focus only on the effect of substrate curvature on the behavior of the sensor. Further, the backside boundary condition is assumed adiabatic for both cases. The error is determined as a function of the radius of the substrate (4 mm to 6 mm) as the

radius of PV ostium is the similar range. Fig. SI.4.2 (b, c) shows that there would be negligible error introduced by the balloon substrate.

5. Conclusion and Future Research Directions

5.1 Conclusion

Bioheat applications at the microscale and nanoscale are driving the need for thermal conductivity and calorimetric measurement at new dimensional and temporal scales. In the first chapter, we have discussed new measurement tools and opportunities to make these measurements. This review serves as an overview of measurement of thermal conductivity, latent heat and specific heat in the cryogenic (< -40 °C) and hyperthermic (> 40^0C) regimes where water, protein and lipid phase changes occur correlate to injury. In the second chapter, we have compiled thermal conductivity and specific heat capacity values of human and porcine systems in the subzero and supra-zero temperature ranges for the purposes of aiding the development of accurate models of conditions and pathologic treatments involving bio-heat transfer mechanisms. In the third chapter, we have used a new micro-thermal sensor based on 3ω technique to determine thermal conductivity of thin cardiac tissues such as pulmonary vein, phrenic nerve and esophagus. Further, we performed proof of concept experiments to sense tissue contact, thickness and freezing phase change. These measurements could potentially be used for monitoring cryoablation of pulmonary vein for treatment of atrial fibrillation. In the fourth chapter, we have we have shown how to modify a linear 3ω sensor for use on a balloon using a serpentine heater line and flexible electronic approaches. First, we numerically studied the behavior of the serpentine sensor on a flat substrate for different materials of varying thickness. Then, we explored the error introduced by curvature of the substrate. Next, we show experimental measurements of serpentine sensors on flat substrates for sensing contact, thickness and phase change within thin biological tissues at the limit of resolution of clinical imaging, 0.5 – 2 mm. Finally, we demonstrate experimental proof of principle that we can integrate the sensor onto a balloon and make similar measurements.

5.2. Future Research Direction: Perform Ex Vivo Testing of the 3ω Sensor in Porcine Heart Lung Block

Ex vivo testing of the balloons with sensors will be undertaken in a porcine heart lung block which is sufficiently close to human to warrant careful ex vivo study.

5.2.1. Experimental approach

The sensor implemented balloons will be manufactured as in Chapter 4 and tested *ex vivo* on porcine heart- lung blocks each containing four pulmonary vein (PV). To mimic extreme conditions, 2 of the PVs in each heart lung block will be studied while being manipulated in air, and then the other 2 while immersed in a 37 °C water bath with or without flow. Flow will be induced through PV by a peristaltic pump to mimic blood flow during balloon seating. While no *in vivo* studies are proposed, valuable data and iteration with ex vivo tissue will allow our electrophysiologist to help us redesign the sensor array for later *in vivo* study. For each PV experiment, we will measure: (1) balloon seating, (2) PV thickness, (3) presence of adjacent tissues beyond PV, (4) initiation and completion of phase change.

5.2.2. Expected outcome

We expect that the sensors in contact and properly seated (visually) in the PV will read a reproducible thermal conductivity that is higher than air, and lower than water. Further, we will use the sensor to predict the thickness of the PV (confirmation with Thickness gauge) and we will use this to guide the time of freezing during cryoablation. The intramural freezing completion will be corroborated visually, and by direct temperature measurement from outside the PV.

6. Bibliography

1.   Chu, K. F.; Dupuy, D. E., Thermal ablation of tumours: biological mechanisms and advances in therapy. *Nat Rev Cancer* **2014,** *14* (3), 199-208.

2.   Piccini, J. P.; Daubert, J. P., Cryoablation of atrial fibrillation. *J Interv Card Electrophysiol* **2011,** *32* (3), 233-242.

3.   Thomas, G.; Shishehbor, M. H.; Bravo, E. L.; Nally, J. V., Renal denervation to treat resistant hypertension: Guarded optimism. *Cleveland Clinic Journal of Medicine* **2012,** *79* (7), 501-510.

4.   Gallagher, J. J.; Anderson, R. W.; Kasell, J.; Rice, J. R.; Pritchett, E. L.; Gault, H. J.; Harrison, L.; Wallace, A. G., Cryoablation of drug-resistant ventricular tachycardia in a patient with a variant of scleroderma. *Circulation* **1978,** *57* (1), 190-197.

5.   Lewis, J. K.; Bischof, J. C.; Braslavsky, I.; Brockbank, K. G. M.; Fahy, G. M.; Fuller, B. J.; Rabin, Y.; Tocchio, A.; Woods, E. J.; Wowk, B. G.; Acker, J. P.; Giwa, S., The Grand Challenges of Organ Banking: Proceedings from the first global summit on complex tissue cryopreservation. *Cryobiology* **2016,** *72* (2), 169-182.

6.   OPTN: Organ Procurement and Transplantation Network - OPTN. https://optn.transplant.hrsa.gov/

files/192/optn.transplant.hrsa.gov.html.

7.   Saving Lives and Giving Hope by Reducing the Organ Waiting List. https://www.whitehouse.gov/blog/2016/06/13/saving-lives-and-giving-hope-reducing-organ-waiting-list

files/195/saving-lives-and-giving-hope-reducing-organ-waiting-list.html.

8.   Karlsson, J. O. M.; Toner, M., Long-term storage of tissues by cryopreservation: critical issues. *Biomaterials* **1996,** *17* (3), 243-256.

9.   Mazur, P., Freezing of living cells: mechanisms and implications. *The American journal of physiology* **1984,** *247* (3 Pt 1), C125-142.

10.   Fahy, G. M.; MacFarlane, D. R.; Angell, C. A.; Meryman, H. T., Vitrification as an approach to cryopreservation. *Cryobiology* **1984,** *21*, 407-426.

11.   Song, Y. C.; Khirabadi, B. S.; Lightfoot, F.; Brockbank, K. G. M.; Taylor, M. J., Vitreous cryopreservation maintains the function of vascular grafts. *Nature Biotechnology* **2000,** *18*, 296-299.

12.   Carpenter, J. F.; Pikal, M. J.; Chang, B. S.; Randolph, T. W., Rational Design of Stable Lyophilized Protein Formulations: Some Practical Advice. *Pharmaceutical Research* **1997,** *14* (8), 969-975.

13.   Crowe, J. H.; Hoekstra, F. A.; Crowe, L. M., Anhydrobiosis. *Annual Review of Physiology* **1992,** *54* (1), 579-599.

14.   Choi, J.; Bischof, J. C., Review of biomaterial thermal property measurements in the cryogenic regime and their use for prediction of equilibrium and non-equilibrium freezing applications in cryobiology. *Cryobiology* **2010,** *60* (1), 52-70.

15.   Natesan, H.; Choi, J. H.; Lubner, S. D.; Dames, C.; Bischof, J., Multi-scale thermal conductivity measurements for cryobiological applications. In *Micro and Nanotechnology in Cryomedicine: Implementation from Nano to Microscale*, 1st ed.; World Scientific: 2016.

16.   Steponkus, P. L., *Advances in Low-Temperature Biology*. Elsevier: 1996; p 337.

17.   Belzer, F. O.; Southard, J. H., Principles of solid-organ preservation by cold storage. *Transplantation* **1988,** *45* (4), 673-676.

18.   Gage, A. A.; Baust, J., Mechanisms of Tissue Injury in Cryosurgery. *Cryobiology* **1998,** *37* (3), 171-186.

19.   Hoffmann, N. E.; Bischof, J. C., The cryobiology of cryosurgical injury. *Urology* **2002,** *60* (2, Supplement 1), 40-49.

20.   Sapareto, S. A.; Dewey, W. C., Thermal dose determination in cancer therapy. *International Journal of Radiation Oncology*Biology*Physics* **1984,** *10* (6), 787-800.

21.   O'Neal, D. P.; Hirsch, L. R.; Halas, N. J.; Payne, J. D.; West, J. L., Photo-thermal tumor ablation in mice using near infrared-absorbing nanoparticles. *Cancer letters* **2004,** *209* (2), 171-176.

22.   Hill, J. E.; Leitman, J. D.; Sunderland, J. E., Thermal Conductivity of Various Meats. *Food Technology* **1967,** *21* (1143), 91 - 96.

23.   Poppendiek, H. F.; Randall, R.; Breeden, J. A.; Chambers, J. E.; Murphy, J. R., Thermal conductivity measurements and predictions for biological fluids and tissues. *Cryobiology* **1967,** *3* (4), 318-327.

24.   Committee, E. *Test Method for Evaluating the Resistance to Thermal Transmission of Materials by the Guarded Heat Flow Meter Technique*; ASTM International: 2011, 2011.

25.   Glassbrenner, C. J.; Slack, G. A., Thermal Conductivity of Silicon and Germanium from 3°K to the Melting Point. *Phys. Rev.* **1964,** *134* (4A), A1058-A1069.

26.   Vachon, R. I.; Walker, F. J.; Walker, D. F.; Nix, G. H. In *In vivo determination of thermal conductivity of bone using the thermal comparator technique*, 1967; 1967.

27.   Morley, M. J., Thermal conductivities of muscles, fats and bones. *International Journal of Food Science & Technology* **1966,** *1* (4), 303-311.

28.   Vendrik, A. J. H.; Vos, J. J., A method for the measurement of the thermal conductivity of human skin. *Journal of Applied Physiology* **1957,** *11* (2), 211-215.

29.   Grayson, J., Internal Calorimetry in the Determination of Thermal Conductivity and Blood Flow. *Journal of Physiology* **1952,** *118*, 54-72.

30.   Lee, W.; Fon, W.; Axelrod, B. W.; Roukes, M. L., High-sensitivity microfluidic calorimeters for biological and chemical applications. *Proceedings of the National Academy of Sciences of the United States of America* **2009,** *106* (36), 15225-30.

31.   Bhattacharya, A.; Mahajan, R. L., Temperature dependence of thermal conductivity of biological tissues. *Physiol. Meas.* **2003,** *24* (3).

32.   Blackwell, J. H., A Transient-Flow Method for Determination of Thermal Constants of Insulating Materials in Bulk Part I—Theory. *Journal of Applied Physics* **1954,** *25* (2).

33.   Andersson, P.; Backstrom, G., Thermal conductivity of solids under pressure by the transient hot wire method. *Review of Scientific Instruments* **1976,** *47* (2), 205-209.

34.   Assael, M. J.; Chen, C. F.; Metaxa, I.; Wakeham, W. A., Thermal Conductivity of Suspensions of Carbon Nanotubes in Water. *International Journal of Thermophysics* **2004,** *25* (4), 971-985.

35.   Ehrlich, L. E.; Feig, J. S. G.; Schiffres, S. N.; Malen, J. A.; Rabin, Y., Large Thermal Conductivity Differences between the Crystalline and Vitrified States of DMSO with Applications to Cryopreservation. *PloS one* **2015,** *10* (5), e0125862.

36.   Ehrlich, L. E.; Malen, J. A.; Rabin, Y., Thermal conductivity of the cryoprotective cocktail DP6 in cryogenic temperatures, in the presence and absence of synthetic ice modulators. *Cryobiology* **2016**.

37.   Chato, J. C. In *A Method for the Measurement of the Thermal Properties of Biological Materials*, Symposium on Thermal Problems in Biotechnology, New York, The American Society of Mechanical Engineers: New York, 1968; pp 16-25.

38.	Chato, J. C., Measurement of thermal properties of growing tumors. *Annals of the New York Academy of Sciences* **1980,** *335* (1), 67-85.

39.	Balasubramaniam, T. A.; Bowman, H. F., Thermal conductivity and thermal diffusivity of biomaterials: a simultaneous measurement technique. *Transactions of the ASME. Series K, Journal of Biomechanical Engineering* **1977,** *99* (3), 148-54.

40.	Chen, M. M.; Holmes, K. R.; Rupinskas, V., Pulse-decay method for measuring the thermal conductivity of living tissues. *Journal of Biomechanical Engineering* **1981,** *103*, 253-260.

41.	Valvano, J. W.; Cochran, J. R.; Diller, K. R., Thermal conductivity and diffusivity of biomaterials measured with self-heated thermistors. *International Journal of Thermophysics* **1985,** *6* (3), 301-311.

42.	Patel, P. A.; Valvano, J. W.; Pearce, J. A.; Prahl, S. A.; Denham, C. R., A self-heated thermistor technique to measure effective thermal properties from the tissue surface. *Journal of biomechanical engineering* **1987,** *109* (4).

43.	Choi, J.; Morrissey, M.; Bischof, J., Thermal Processing of Biological Tissue at High Temperatures: Impact of Protein Denaturation and Water Loss on the Thermal Properties of Human and Porcine Liver in the Range 25–80 °C. *Journal of Heat Transfer* **2013,** *135* (6), 061302.

44.	Zhang, H.; Cheng, S.; He, L.; Zhang, A.; Zheng, Y.; Gao, D., Determination of thermal conductivity of biomaterials in the temperature range 233-313K using a tiny detector made of a self-heated thermistor. *Cell Preservation Technology* **2002,** *1* (2), 141-147.

45.	Lubner, S. D.; Choi, J.; Wehmeyer, G.; Waag, B.; Mishra, V.; Natesan, H.; Bischof, J. C.; Dames, C., Reusable bi-directional 3ω sensor to measure thermal conductivity of 100-μm thick biological tissues. *Review of Scientific Instruments* **2015,** *86* (1).

46.	Dames, C.; Chen, G., 1ω,2ω, and 3ω methods for measurements of thermal properties. *Review of Scientific Instruments* **2005,** *76* (12).

47.   Cahill, D. G.; Pohl, R. O., Thermal conductivity of amorphous solids above the plateau. *Physical Review B (Condensed Matter)* **1987,** *35* (8), 4067-73.

48.   Parker, W. J.; Jenkins, R. J.; Butler, C. P.; Abbott, G. L., Flash Method of Determining Thermal Diffusivity, Heat Capacity, and Thermal Conductivity. *Journal of Applied Physics* **1961,** *32* (9), 1679.

49.   Cape, J. A.; Lehman, G. W., Temperature and Finite Pulse-Time Effects in the Flash Method for Measuring Thermal Diffusivity. *Journal of Applied Physics* **1963,** *34* (7), 1909-1913.

50.   Tada, Y.; Harada, M.; Tanigaki, M.; Eguchi, W., Laser flash method for measuring thermal conductivity of liquids ;application to low thermal conductivity liquids. *Review of Scientific Instruments* **1978,** *49* (9), 1305-1314.

51.   Park, B. K.; Yi, N.; Park, J.; Kim, Y.; Kim, D., Development of a thermal sensor to probe cell viability and concentration in cell suspensions. *AIP Advances* **2014,** *4* (4), 047120.

52.   Park, B. K.; Woo, Y.; Jeong, D.; Park, J.; Choi, T.-Y.; Simmons, D. P.; Ha, J.; Kim, D., Thermal conductivity of biological cells at cellular level and correlation with disease state. *Journal of Applied Physics* **2016,** *119* (22), 224701.

53.   Paddock, C. A.; Eesley, G. L., Transient thermoreflectance from thin metal films. *Journal of Applied Physics* **1986,** *60* (1), 285-290.

54.   Cahill, D. G., Analysis of heat flow in layered structures for time-domain thermoreflectance. *Review of Scientific Instruments* **2004,** *75* (12), 5119-5122.

55.   Majumdar, A.; Carrejo, J. P.; Lai, J., Thermal imaging using the atomic force microscope. *Applied Physics Letters* **1993,** *62* (20), 2501-2503.

56.   Pylkki, R. J.; Moyer, P. J.; West, P. E., Scanning Near-Field Optical Microscopy and Scanning Thermal Microscopy. *Japanese Journal of Applied Physics* **1994,** *33* (Part 1, No. 6B), 3785-3790.

116

57.   Wu, X.; Ni, Y.; Zhu, J.; Burrows, N. D.; Murphy, C. J.; Dumitrica, T.; Wang, X., Thermal Transport across Surfactant Layers on Gold Nanorods in Aqueous Solution. *ACS Appl. Mater. Interfaces* **2016,** *8* (16), 10581-10589.

58.   Huang, J.; Park, J.; Wang, W.; Murphy, C. J.; Cahill, D. G., Ultrafast Thermal Analysis of Surface Functionalized Gold Nanorods in Aqueous Solution. *ACS Nano* **2013,** *7* (1), 589-597.

59.   Ge, Z.; Cahill, D. G.; Braun, P. V., AuPd Metal Nanoparticles as Probes of Nanoscale Thermal Transport in Aqueous Solution. *J. Phys. Chem. B* **2004,** *108* (49), 18870-18875.

60.   Wilson, O. M.; Hu, X.; Cahill, D. G.; Braun, P. V., Colloidal metal particles as probes of nanoscale thermal transport in fluids. *Physical Review B* **2002,** *66* (22).

61.   Bhowmick, S.; Bischof, J. C., Source terms in thermal therapy: a parametric study. *ASME-PUBLICATIONS-HTD* **2000,** *368*, 161-170.

62.   Choi, J. H.; Bischof, J. C., A quantitative analysis of the thermal properties of porcine liver with glycerol at subzero and cryogenic temperatures. *Cryobiology* **2008,** *57* (2), 79-83.

63.   Cherneeva, L. I., Study of thermal properties of foods. *Report of Vnikhi (Scientific Research Institute of the Refrigeration Industry), Gostorgisdat, Moscow* **1956**.

64.   Lepock, J. R., Cellular effects of hyperthermia: relevance to the minimum dose for thermal damage. *International journal of hyperthermia : the official journal of European Society for Hyperthermic Oncology, North American Hyperthermia Group* **2003,** *19* (3), 252-66.

65.   Lerchner, J.; Wolf, A.; Schneider, H. J.; Mertens, F.; Kessler, E.; Baier, V.; Funfak, A.; Nietzsch, M.; Krügel, M., Nano-calorimetry of small-sized biological samples. *Thermochimica Acta* **2008,** *477* (1-2), 48-53.

66.   Lerchner, J.; Maskow, T.; Wolf, G., Chip calorimetry and its use for biochemical and cell biological investigations. *Chemical Engineering and Processing: Process Intensification* **2008,** *47* (6), 991-999.

117

67.   Yi, F.; Kim, I. K.; Li, S.; Lavan, D. A., Hydrated/Dehydrated Lipid Phase Transitions Measured Using Nanocalorimetry. *J Pharm Sci* **2014,** *103* (11), 3442-3447.

68.   Lerchner, J.; Mueller-Hagen, D.; Roehr, H.; Wolf, A.; Mertens, F.; Mueller, R.; Witte, W.; Klare, I., Chip-calorimetric evaluation of the efficacy of antibiotics and bacteriophages against bacteria on a minute-timescale. *Journal of Thermal Analysis and Calorimetry* **2011,** *104* (1), 31-36.

69.   Ahmad, L. M.; Towe, B.; Wolf, A.; Mertens, F.; Lerchner, J., Binding event measurement using a chip calorimeter coupled to magnetic beads. *Sensors and Actuators B: Chemical* **2010,** *145* (1), 239-245.

70.   Recht, M. I.; Torres, F. E.; Bruyker, D. D.; Bell, A. G.; Klumpp, M.; Bruce, R. H., Measurement of enzyme kinetics and inhibitor constants using enthalpy arrays. *Analytical biochemistry* **2009,** *388* (2), 204-212.

71.   Toda, A.; Androsch, R.; Schick, C., Insights into polymer crystallization and melting from fast scanning chip calorimetry. *Polymer* **2016,** *91*, 239-263.

72.   Minakov, A. A.; Schick, C., Ultrafast thermal processing and nanocalorimetry at heating and cooling rates up to 1 MK/s. *Review of Scientific Instruments* **2007,** *78* (7), 073902-073902.

73.   Bowman, H. F.; Cravalho, E. G.; Woods, M., Theory, Measurement, and Application of Thermal Properties of Biomaterials. *Annual Review of Biophysics and Bioengineering* **1975,** *4* (1), 43-80.

74.   Chato, J. C., Measurement of thermal properties of biological materials. *Heat transfer in medicine and biology* **1985,** *1*, 167-173.

75.   Eucken, A., Allgemeine Gesetzmäßigkeiten für das Wärmeleitvermögen verschiedener Stoffarten und Aggregatzustände. *Forsch Ing-Wes* **1940,** *11* (1), 6-20.

76.   Kopelman, I. J., *Transient Heat Transfer and Thermal Properties in Food Systems*. Michigan State University. Department of Food Science: 1966; p 270.

77.   Levy, F. L., A modified Maxwell-Eucken equation for calculating the thermal conductivity of two-component solutions or mixtures. *International Journal of Refrigeration* **1981,** *4* (4), 223-225.

78.   Murakami, E. G.; Okos, M. R., Measurement and Prediction of Thermal Properties of Foods. In *Food Properties and Computer-Aided Engineering of Food Processing Systems*, Singh, R. P.; Medina, A. G., Eds. Springer Netherlands: 1989; pp 3-48.

79.   Rabin, Y., The effect of temperature-dependent thermal conductivity in heat transfer simulations of frozen biomaterials. *Cryo Letters* **2000,** *21* (3), 163-170.

80.   Han, B.; Bischof, J. C., Thermodynamic nonequilibrium phase change behavior and thermal properties of biological solutins for cryobiology applications. *Journal of Biomechanical Engineering* **2004,** *126*, 196-203.

81.   Choi, J. H.; Bischof, J. C., A quantitative analysis on the thermal properties of phosphate buffered saline with glycerol at subzero temperatures. *International Journal of Heat and Mass Transfer* **2008,** *51* (3-4), 640-649.

82.   Mazur, P.; Leibo, S. P.; Chu, E. H., A two-factor hypothesis of freezing injury. Evidence from Chinese hamster tissue-culture cells. *Experimental Cell Research* **1972,** *71* (2), 345-55.

83.   Toner, M.; Cravalho, E. G.; Karel, M., Thermodynamics and kinetics of intracellular ice formation during freezing of biological cells. *Journal of Applied Physics* **1990,** *67* (3), 1582-1593.

84.   Choi, J.; Bischof, J. C., Cooling rate dependent biophysical and viability response shift with attachment state in human dermal fibroblast cells. *Cryobiology* **2011,** *63* (3), 285-291.

85.   Acker, J. P.; McGann, L. E., Protective effect of intracellular ice during freezing? *Cryobiology* **2003,** *46* (2), 197-202.

119

86.   Irimia, D.; Karlsson, J. O. M., Kinetics and Mechanism of Intercellular Ice Propagation in a Micropatterned Tissue Construct. *Biophysical journal* **2002,** *82* (4), 1858-1868.

87.   Acker, J. P.; Larese, A.; Yang, H.; Petrenko, A.; McGann, L. E., Intracellular Ice Formation Is Affected by Cell Interactions. *Cryobiology* **1999,** *38* (4), 363-371.

88.   Berger, W. K.; Uhrík, B., Freeze-induced shrinkage of individual cells and cell-to-cell propagation of intracellular ice in cell chains from salivary glands. *Experientia* **1996,** *52* (9), 843-850.

89.   Raphael, C. L.; Dajun, Z.; Hannig; Jurgen, Biophysical Injury Mechanisms in Electrical Shock Trauma. *Annual Review of Biomedical Engineering* **2000,** *2* (1), 477-509.

90.   Cahill, D. G.; Katiyar, M.; Abelson, J. R., Thermal conductivity of a-Si: H thin films. *Physical Review B* **1994,** *50* (9).

91.   Borca-Tasciuc, T.; Kumar, A. R.; Chen, G., Data reduction in 3omega method for thin-film thermal conductivity determination. *Review of Scientific Instruments* **2001,** *72* (4), 2139-2147.

92.   Olson, B. W.; Graham, S.; Chen, K., A practical extension of the 3ω method to multilayer structures. *Review of Scientific Instruments* **2005,** *76* (5).

93.   Kim, J. H.; Feldman, A.; Novotny, D., Application of the three omega thermal conductivity measurement method to a film on a substrate of finite thickness. *Journal of Applied Physics* **1999,** *86* (7), 3959-3963.

94.   Tong, T.; Majumdar, A., Reexamining the 3-omega technique for thin film thermal characterization. *Review of Scientific Instruments* **2006,** *77* (10), 104902-104902-9.

95.   Lu, L.; Yi, W.; Zhang, D. L., 3 w method for specific heat and thermal conductivity measurements. *Review of Scientific Instruments* **2001,** *72* (7), 2996-3003.

96.   Choi, S. R.; Kim, D., Real-time thermal characterization of 12 nl fluid samples in a microchannel. *The Review of scientific instruments* **2008,** *79* (6), 064901.

97.   Roy-Panzer, S.; Kodama, T.; Lingamneni, S.; Panzer, M. A.; Asheghi, M.; Goodson, K. E., Thermal characterization and analysis of microliter liquid volumes using the three-omega method. *The Review of scientific instruments* **2015,** *86* (2), 024901.

98.   Schiffres, S. N.; Malen, J. A., Improved 3-omega measurement of thermal conductivity in liquid, gases, and powders using a metal-coated optical fiber. *Review of Scientific Instruments* **2011,** *82* (6), 064903.

99.   Hobbs, P. V., *Ice physics*. Oxford: Clarendon Press: New York, 1974; Vol. 1.

100.   Caffrey, M., *LIPIDAT A Database of Thermo Data and Association Information on Lipid*. CRC Press: 1993; p 356.

101.   Privalov, P. L.; Khechinashvili, N. N., A thermodynamic approach to the problem of stabilization of globular protein structure: a calorimetric study. *Journal of molecular biology* **1974,** *86* (3), 665-684.

102.   Ohta, H.; Shibata, H.; Waseda, Y., New attempt for measuring thermal diffusivity of thin films by means of a laser flash method. *Review of Scientific Instruments* **1989,** *60* (3), 317-321.

103.   Natesan, H.; Hodges, W.; Choi, J.; Lubner, S.; Dames, C.; Bischof, J., A Micro-Thermal Sensor for Focal Therapy Applications. *Scientific Reports* **2016,** *6*, 21395.

104.   Park, B. K.; Yi, N.; Park, J.; Kim, D., Development of a microfabricated sensor to measure thermal conductivity of picoliter scale liquid samples. *The Review of scientific instruments* **2012,** *83* (10), 106102.

105.   Park, B. K.; Yi, N.; Park, J.; Kim, D., Thermal conductivity of single biological cells and relation with cell viability. *Applied Physics Letters* **2013,** *102* (20).

106.   Feldman, A., Algorithm for solutions of the thermal diffusion equation in a stratified medium with a modulated heating source. *High Temperatures - High Pressures* **1999,** *31* (3).

107.   Committee, E. *Test Method for Thermal Diffusivity by the Flash Method*; ASTM International: 2013, 2013.

108.   Choy, C. L.; Leung, W. P.; Ng, Y. K., Thermal diffusivity of polymer films by the flash radiometry method. *Journal of Polymer Science Part B: Polymer Physics* **1987,** *25* (9), 1779-1799.

109.   Nunes dos Santos, W.; Mummery, P.; Wallwork, A., Thermal diffusivity of polymers by the laser flash technique. *Polymer Testing* **2005,** *24* (5), 628-634.

110.   Akoshima, M.; Hata, K.; Futaba, D. N.; Mizuno, K.; Baba, T.; Yumura, M., Thermal Diffusivity of Single-Walled Carbon Nanotube Forest Measured by Laser Flash Method. *Japanese Journal of Applied Physics* **2009,** *48* (5S2), 05EC07.

111.   Mehling, H.; Hautzinger, G.; Nilsson, O.; Fricke, J.; Hofmann, R.; Hahn, O., Thermal Diffusivity of Semitransparent Materials Determined by the Laser-Flash Method Applying a New Analytical Model. *International Journal of Thermophysics* **1998,** *19* (3), 941-949.

112.   Rudkin, R. L.; Jenkins, R. J.; Parker, W. J., Thermal Diffusivity Measurements on Metals at High Temperatures. *Review of Scientific Instruments* **1962,** *33* (1), 21-24.

113.   Shibata, H.; Ohta, H.; Waseda, Y., New Laser-Flash Method for Measuring Thermal Diffusivity of Isotropic and Anisotropic Thin Films. *Materials Transactions, JIM* **1991,** *32* (9), 837-844.

114.   Ohta, H.; Shibata, H.; Waseda, Y., New attempt for measuring thermal diffusivity of thin films by means of a laser flash method. *Review of Scientific Instruments* **1989,** *60* (3), 317-321.

115.   Harada, T.; Hata, T.; Ishihara, S., Thermal constants of wood during the heating process measured with the laser flash method. *J Wood Sci* **1998,** *44* (6), 425-431.

116.   Coquard, R.; Panel, B., Adaptation of the FLASH method to the measurement of the thermal conductivity of liquids or pasty materials. *International Journal of Thermal Sciences* **2009,** *48* (4), 747-760.

117.   Kogure, Y.; Mugishima, Y.; Hiki, T., Low-Temperature Thermal Diffusivity Measurement by Laser-Flash Method. *J Phys Soc Jpn* **1986,** *55* (10), 3469-3478.

118.   Milošević, N.; Raynaud, M.; Maglić, K., Estimation of thermal Contact Resistance Between the Materials of Double-Layer Sample Using the Laser Flash Method. *Inverse Probl Eng* **2002,** *10* (1), 85-103.

119.   Campbell, R. C.; Smith, S. E.; Dietz, R. L. In *Measurements of adhesive bondline effective thermal conductivity and thermal resistance using the laser flash method*, Fifteenth Annual IEEE Semiconductor Thermal Measurement and Management Symposium (Cat. No.99CH36306), 1999/03//; 1999; pp 83-97.

120.   Casalegno, V.; Vavassori, P.; Valle, M.; Ferraris, M.; Salvo, M.; Pintsuk, G., Measurement of thermal properties of a ceramic/metal joint by laser flash method. *J Nucl Mater* **2010,** *407* (2), 83-87.

121.   Shitzer, A.; Becker, B. R.; Fricke, B. A., Thermal Properties of Foods. In *Refrigeration, 2006 ASHRAE Handbook*, S., O. M., Ed. ASHRAE: 2006; pp 9.1-9.31.

122.   Akoshima, M.; Neda, M.; Baba, T., *Quantitative evaluation of the Effect of Black-Coating for Laser Flash Measurement*. DEStech Publications, Inc: 2013; p 343.

123.   Hay, B.; Filtz, J. R.; Hameury, J.; Rongione, L., Uncertainty of Thermal Diffusivity Measurements by Laser Flash Method. *International Journal of Thermophysics* **2005,** *26* (6), 1883-1898.

124.   Foley, B. M.; Gorham, C. S.; Duda, J. C.; Cheaito, R.; Szwejkowski, C. J.; Constantin, C.; Kaehr, B.; Hopkins, P. E., Protein Thermal Conductivity Measured in the Solid State Reveals Anharmonic Interactions of Vibrations in a Fractal Structure. *J. Phys. Chem. Lett.* **2014,** *5* (7), 1077-1082.

125.   Ohta, H.; Ogura, G.; Waseda, Y.; Suzuki, M., Thermal diffusivity measurements of molten salts using a three layered cell by the laser flash method. *Review of Scientific Instruments* **1990,** *61* (10), 2645-2649.

126.   Panas, A. J.; Żmuda, S.; Terpiłowski, J.; Preiskorn, M., Investigation of the Thermal Diffusivity of Human Tooth Hard Tissue. *International Journal of Thermophysics* **2003,** *24* (3), 837-848.

127.   Capinski, W., Thermal-conductivity measurements of GaAs/AlAs superlattices using a picosecond optical pump-and-probe technique. *Physical Review B* **1999,** *59* (12), 8105-8113.

128.   Huxtable, S.; Cahill, D. G.; Fauconnier, V.; White, J. O.; Zhao, J.-C., Thermal conductivity imaging at micrometre-scale resolution for combinatorial studies of materials. *Nat Mater* **2004,** *3* (5), 298-301.

129.   Wang, X.; Ho, V.; Segalman, R. A.; Cahill, D. G., Thermal Conductivity of High-Modulus Polymer Fibers. *Macromolecules* **2013,** *46* (12), 4937-4943.

130.   Wang, X.; Liman, C. D.; Treat, N. D.; Chabinyc, M. L.; Cahill, D. G., Ultralow thermal conductivity of fullerene derivatives. *Physical Review B* **2013,** *88* (7).

131.   Schmidt, A. J.; Chen, X.; Chen, G., Pulse accumulation, radial heat conduction, and anisotropic thermal conductivity in pump-probe transient thermoreflectance. *Review of Scientific Instruments* **2008,** *79* (11).

132.   Feser, J. P.; Cahill, D. G., Probing anisotropic heat transport using time-domain thermoreflectance with offset laser spots. *Review of Scientific Instruments* **2012,** *83* (10), 104901-104901-7.

133.   Zhu, J.; Park, H.; Chen, J.-Y.; Gu, X.; Zhang, H.; Karthikeyan, S.; Wendel, N.; Campbell, S. A.; Dawber, M.; Du, X.; Li, M.; Wang, J.-P.; Yang, R.; Wang, X., Revealing the Origins of 3D

Anisotropic Thermal Conductivities of Black Phosphorus. *Adv. Electron. Mater.* **2016,** *2* (5), n/a-n/a.

134.   Schmidt, A.; Chiesa, M.; Chen, X.; Chen, G., An optical pump-probe technique for measuring the thermal conductivity of liquids. *Review of Scientific Instruments* **2008,** *79* (6).

135.   Costescu, R. M.; Wall, M. A.; Cahill, D. G., Thermal conductance of epitaxial interfaces. *Physical Review B* **2003,** *67* (5).

136.   Ge, Z.; Cahill, D. G.; Braun, P. V., Thermal Conductance of Hydrophilic and Hydrophobic Interfaces. *Physical Review Letters* **2006,** *96* (18).

137.   Wang, Z.; Carter, J. A.; Lagutchev, A.; Koh, Y. K.; Seong, N.-H.; Cahill, D. G.; Dlott, D. D., Ultrafast Flash Thermal Conductance of Molecular Chains. *Science* **2007,** *317* (5839), 787-790.

138.   Losego, M. D.; Grady, M. E.; Sottos, N. R.; Cahill, D. G.; Braun, P. V., Effects of chemical bonding on heat transport across interfaces. *Nat Mater* **2012,** *11* (6), 502-506.

139.   Koh, Y. K.; Singer, S. L.; Kim, W.; Zide, J. M. O.; Lu, H.; Cahill, D. G.; Majumdar, A.; Gossard, A. C., Comparison of the 3omega method and time-domain thermoreflectance for measurements of the cross-plane thermal conductivity of epitaxial semiconductors. *Journal of Applied Physics* **2009,** *105* (5), 054303-054303-7.

140.   Chen, J.-Y.; Zhu, J.; Zhang, D.; Lattery, D. M.; Li, M.; Wang, J.-P.; Wang, X., Time-Resolved Magneto-Optical Kerr Effect of Magnetic Thin Films for Ultrafast Thermal Characterization. *J. Phys. Chem. Lett.* **2016,** *7* (13), 2328-2332.

141.   Liu, J.; Choi, G.-M.; Cahill, D. G., Measurement of the anisotropic thermal conductivity of molybdenum disulfide by the time-resolved magneto-optic Kerr effect. *Journal of Applied Physics* **2014,** *116* (23), 233107.

142.   Ujihara, K., Reflectivity of Metals at High Temperatures. *Journal of Applied Physics* **2003,** *43* (5), 2376-2383.

125

143.   Schmidt, A. J.; Cheaito, R.; Chiesa, M., Characterization of thin metal films via frequency-domain thermoreflectance. *Journal of Applied Physics* **2010,** *107* (2), 024908.

144.   Yang, J.; Maragliano, C.; Schmidt, A. J., Thermal property microscopy with frequency domain thermoreflectance. *Review of Scientific Instruments* **2013,** *84* (10), 104904.

145.   Gao, Y.; Marconnet, A. M.; Xiang, R.; Maruyama, S.; Goodson, K. E., Heat Capacity, Thermal Conductivity, and Interface Resistance Extraction for Single-Walled Carbon Nanotube Films Using Frequency-Domain Thermoreflectance. *IEEE Transactions on Components, Packaging and Manufacturing Technology* **2013,** *3* (9), 1524-1532.

146.   Freedman, J. P.; Yu, X.; Davis, R. F.; Gellman, A. J.; Malen, J. A., Thermal interface conductance across metal alloy\dielectric interfaces. *Physical Review B* **2016,** *93* (3), 035309.

147.   Schmidt, A. J.; Cheaito, R.; Chiesa, M., A frequency-domain thermoreflectance method for the characterization of thermal properties. *Review of Scientific Instruments* **2009,** *80* (9).

148.   Qin, Z.; Bischof, J. C., Thermophysical and biological responses of gold nanoparticle laser heating. *Chemical Society reviews* **2012,** *41* (3), 1191-217.

149.   Li, M. H.; Gianchandani, Y. B., Applications of a low contact force polyimide shank bolometer probe for chemical and biological diagnostics. *Sensors and Actuators A: Physical* **2003,** *104* (3), 236-245.

150.   Park, J.; Huang, J.; Wang, W.; Murphy, C. J.; Cahill, D. G., Heat Transport between Au Nanorods, Surrounding Liquids, and Solid Supports. *J. Phys. Chem. C* **2012,** *116* (50), 26335-26341.

151.   Cahill, D. G.; Choi, G. M.; Park, J.; Huang, J.; Wang, W.; Wilson, R. Ultrafast Heat Transfer in Nanoscale Materials.

152.   Vasudevan, S.; Chen, G. C. K.; Andika, M., Application of thermal lens response to monitor health status of red blood cells: A quantitative study of the cell death process by extracting thermal diffusivity and size. *Applied Physics Letters* **2010,** *96* (11), 113703.

153.   ElAfandy, R. T.; AbuElela, A. F.; Mishra, P.; Janjua, B.; Oubei, H. M.; Büttner, U.; Majid, M. A.; Ng, T. K.; Merzaban, J. S.; Ooi, B. S., Nanomembrane-Based, Thermal-Transport Biosensor for Living Cells. *Small* **2016**, n/a-n/a.

154.   Nonnenmacher, M.; Wickramasinghe, H. K., Scanning probe microscopy of thermal conductivity and subsurface properties. *Applied Physics Letters* **1992,** *61* (2), 168-170.

155.   Assael, M. J.; Chen, C. F.; Metaxa, I.; Wakeham, W. A., Thermal Conductivity of Suspensions of Carbon Nanotubes in Water. *International Journal of Thermophysics* **2004,** *25* (4), 971-985.

156.   Gomès, S.; Newby, P.; Canut, B.; Termentzidis, K.; Marty, O.; Fréchette, L.; Chantrenne, P.; Aimez, V.; Bluet, J.-M.; Lysenko, V., Characterization of the thermal conductivity of insulating thin films by scanning thermal microscopy. *Microelectronics Journal* **2013,** *44* (11), 1029-1034.

157.   Florescu, D. I.; Mourokh, L. G.; Pollak, F. H.; Look, D. C.; Cantwell, G.; Li, X., High spatial resolution thermal conductivity of bulk ZnO (0001). *Journal of Applied Physics* **2002,** *91* (2), 890-892.

158.   Gu, Y. Q.; Ruan, X. L.; Han, L.; Zhu, D. Z.; Sun, X. Y., Imaging of Thermal Conductivity with Sub-Micrometer Resolution Using Scanning Thermal Microscopy. *International Journal of Thermophysics* **2002,** *23* (4), 1115-1124.

159.   Williams, C. C.; Wickramasinghe, H. K., Photothermal Imaging with Sub-100-nm Spatial Resolution. In *Photoacoustic and Photothermal Phenomena*, Hess, P. D. P.; Pelzl, P. D. J., Eds. Springer Berlin Heidelberg: 1988; pp 364-369.

160.   Kim, K.; Jeong, W.; Lee, W.; Reddy, P., Ultra-High Vacuum Scanning Thermal Microscopy for Nanometer Resolution Quantitative Thermometry. *ACS Nano* **2012,** *6* (5), 4248-4257.

161.   Lee, W.; Kim, K.; Jeong, W.; Zotti, L. A.; Pauly, F.; Cuevas, J. C.; Reddy, P., Heat dissipation in atomic-scale junctions. *Nature* **2013,** *498* (7453), 209-212.

162.   Hammiche, A.; Hourston, D. J.; Pollock, H. M.; Reading, M.; Song, M., Scanning thermal microscopy: Subsurface imaging, thermal mapping of polymer blends, and localized calorimetry. *Journal of Vacuum Science Technology B: Microelectronics and Nanometer Structures* **1996,** *14* (2), 1486-1491.

163.   Hammiche, A.; Pollock, H. M.; Song, M.; Hourston, D. J., Sub-surface imaging by scanning thermal microscopy. *Meas Sci Technol* **1996,** *7* (2).

164.   Hammiche, A.; Montagu-Pollock, H. M.; Reading, M.; Song, M. Method and apparatus for performing localized thermal analysis and sub-surface imaging by scanning thermal microscopy. 6,491,425, 2002/12//, 2002.

165.   Luo, K.; Shi, Z.; Lai, J.; Majumdar, A., Nanofabrication of sensors on cantilever probe tips for scanning multiprobe microscopy. *Applied Physics Letters* **1996,** *68* (3), 325-327.

166.   Shen, S.; Henry, A.; Tong, J.; Zheng, R.; Chen, G., Polyethylene nanofibres with very high thermal conductivities. *Nat Nano* **2010,** *5* (4), 251-255.

167.   Shi, L.; Zhou, J.; Kim, P.; Bachtold, A.; Majumdar, A.; McEuen, P. L., Thermal probing of energy dissipation in current-carrying carbon nanotubes. *Journal of Applied Physics* **2009,** *105* (10).

168.   Shnyrov, V. L.; Sanchez-Ruiz, J. M.; Boiko, B. N.; Zhadan, G. G.; Permyakov, E. A., Applications of scanning microcalorimetry in biophysics and biochemistry. *Thermochimica acta* **1997,** *302* (1), 165-180.

169.	Price, D. M.; Reading, M.; Hammiche, A.; Pollock, H. M., Micro-thermal analysis: scanning thermal microscopy and localised thermal analysis. *International journal of pharmaceutics* **1999,** *192* (1), 85-96.

170.	Craig, D. Q. M.; Kett, V. L.; Andrews, C. S.; Royall, P. G., Pharmaceutical applications of micro-thermal analysis. *J Pharm Sci* **2002,** *91* (5), 1201-1213.

171.	Zhang, J.; Bunker, M.; Chen, X.; Parker, A. P.; Patel, N.; Roberts, C. J., Nanoscale thermal analysis of pharmaceutical solid dispersions. *International journal of pharmaceutics* **2009,** *380* (1-2), 170-3.

172.	Nikiforov, M. P.; Hohlbauch, S.; King, W. P.; Voïtchovsky, K.; Contera, S. A.; Jesse, S.; Kalinin, S. V.; Proksch, R., Temperature-dependent phase transitions in zeptoliter volumes of a complex biological membrane. *Nanotechnology* **2011,** *22* (5).

173.	Shi, L.; Majumdar, A., Thermal Transport Mechanisms at Nanoscale Point Contacts. *Journal of Heat Transfer* **2001,** *124* (2), 329-337.

174.	Lefèvre, S.; Volz, S.; Chapuis, P.-O., Nanoscale heat transfer at contact between a hot tip and a substrate. *International Journal of Heat and Mass Transfer* **2006,** *49* (1–2), 251-258.

175.	Park, K.; Cross, G. L.; Zhang, Z. M.; King, W. P., Experimental Investigation on the Heat Transfer Between a Heated Microcantilever and a Substrate. *Journal of Heat Transfer* **2008,** *130* (10), 102401-102401.

176.	Lubner, S. D.; Choi, J.; Hasegawa, Y.; Fong, A.; Bischof, J. C.; Dames, C. In *Measurements of the Thermal Conductivity of Sub-Millimeter Biological Tissues*, ASME 2012 International Mechanical Engineering Congress and Exposition, American Society of Mechanical Engineers: 2012; pp 1397-1404.

177.	Rubinsky, B.; Ikeda, M., A cryomicroscope using directional solidification for the controlled freezing of biological material. *Cryobiology* **1985,** *22* (1), 55-68.

178.   Bischof, J.; Christov, K.; Rubinsky, B., A Morphological Study of Cooling Rate Response in Normal and Neoplastic Human Liver Tissue: Cryosurgical Implications. *Cryobiology* **1993,** *30* (5), 482-492.

179.   Rubinsky, B.; Lee, C. Y.; Bastacky, J.; Onik, G., The process of freezing and the mechanism of damage during hepatic cryosurgery. *Cryobiology* **1990,** *27* (1), 85-97.

180.   Hey, J.; MacFarlane, D., Crystallization of ice in aqueous solutions of glycerol and dimethyl sulfoxide 2: ice crystal growth kinetics. *Cryobiology* **1998,** *37* (2), 119-130.

181.   Feig, J. S. G.; Solanki, P. K.; Eisenberg, D. P.; Rabin, Y., Polarized light scanning cryomacroscopy, part II: Thermal modeling and analysis of experimental observations. *Cryobiology*.

182.   Feig, J. S. G.; Eisenberg, D. P.; Rabin, Y., Polarized light scanning cryomacroscopy, part I: Experimental apparatus and observations of vitrification, crystallization, and photoelasticity effects. *Cryobiology*.

183.   Fox, S. I., *Human Physiology*. 4 ed.; Wm C Brown Publishers: Dubuque, IA, 1993.

184.   Pham, Q. T.; Willix, J., Thermal Conductivity of Fresh Lamb Meat, Offals and Fat in the Range -40 to +30oC: Measurements and Correlations. *Journal of Food Science* **1989,** *54* (3), 508-515.

185.   Urban, A. S.; Fedoruk, M.; Horton, M. R.; Rädler, J. O.; Stefani, F. D.; Feldmann, J., Controlled nanometric phase transitions of phospholipid membranes by plasmonic heating of single gold nanoparticles. *Nano Lett.* **2009,** *9* (8), 2903-2908.

186.   Huettmann, G.; Radt, B.; Serbin, J.; Birngruber, R. In *Inactivation of proteins by irradiation of gold nanoparticles with nano- and picosecond laser pulses*, 2003; 2003; pp 88-95.

187.   Csaki, A.; Garwe, F.; Steinbrück, A.; Maubach, G.; Festag, G.; Weise, A.; Riemann, I.; König, K.; Fritzsche, W., A Parallel Approach for Subwavelength Molecular Surgery Using Gene-Specific Positioned Metal Nanoparticles as Laser Light Antennas. *Nano Lett.* **2007,** *7* (2), 247-253.

188.   Poon, L.; Zandberg, W.; Hsiao, D.; Erno, Z.; Sen, D.; Gates, B. D.; Branda, N. R., Photothermal Release of Single-Stranded DNA from the Surface of Gold Nanoparticles Through Controlled Denaturating and Au−S Bond Breaking. *ACS Nano* **2010,** *4* (11), 6395-6403.

189.   Rao, W.; Bellotti, A.; Littrup, P. J.; Yu, J.; Lu, X.; He, X., Nanoparticle-encapsulated doxorubicin enhances cryoablation of cancer stem-like cells. *Technology* **2014,** *02* (01), 28-35.

190.   Goel, R.; Swanlund, D.; Coad, J.; Paciotti, G. F.; Bischof, J. C., TNF-alpha-based accentuation in cryoinjury--dose, delivery, and response. *Mol. Cancer Ther.* **2007,** *6* (7), 2039-2047.

191.   Han, X.; Ma, H. B.; Wilson, C.; Critser, J. K., Effects of nanoparticles on the nucleation and devitrification temperatures of polyol cryoprotectant solutions. *Microfluid Nanofluid* **2008,** *4* (4), 357-361.

192.   Yue, C.; Zhao, G.; Yi, J.; Gao, C.; Shen, L.; Zhang, Y.; Wang, Z.; Liu, W., Effect of hydroxyapatite nanoparticles on osmotic responses of pig iliac endothelial cells. *Cryobiology* **2014,** *69* (2), 273-280.

193.   Etheridge, M. L.; Xu, Y.; Rott, L.; Choi, J.; Glasmacher, B.; Bischof, J. C., RF heating of magnetic nanoparticles improves the thawing of cryopreserved biomaterials. *Technology* **2014,** *02* (03), 229-242.

194.   Shenoi, M. M.; Iltis, I.; Choi, J.; Koonce, N. A.; Metzger, G. J.; Griffin, R. J.; Bischof, J. C., Nanoparticle Delivered Vascular Disrupting Agents (VDAs): Use of TNF-Alpha Conjugated Gold Nanoparticles for Multimodal Cancer Therapy. *Mol. Pharmaceutics* **2013,** *10* (5), 1683-1694.

195.   Liu, J.; Deng, Z.-S., Nano-Cryosurgery: Advances and Challenges. *Journal of Nanoscience and Nanotechnology* **2009,** *9* (8), 4521-4542.

196.   Govorov, A. O.; Richardson, H. H., Generating heat with metal nanoparticles. *Nano Today* **2007,** *2* (1), 30-38.

197.   Huettmann, G.; Radt, B.; Serbin, J.; Birngruber, R. In *Inactivation of proteins by irradiation of gold nanoparticles with nano- and picosecond laser pulses*, 2003; 2003; pp 88-95.

198.   Buchholz, A. C.; Schoeller, D. A., Is a calorie a calorie? *Am J Clin Nutr* **2004,** *79* (5), 899S-906S.

199.   Pl, P.; Ka, K.; Dr, M., Study of Heat Denaturation of DNA by Use of The Adiabatic Microcalorimeter. *Dokl Akad Nauk SSSR* **1964,** *156*, 951-953.

200.   Privalov, P. L.; Monaselidze, D. R.; Mrevlishvili, G. M.; Magaldadze, V. A., " INTRAMOLECULAR" HEAT OF FUSION OF MACROMOLECULES. *SOVIET PHYSICS JETP* **1965,** *20* (6).

201.   Beck, K.; Gill, S. J.; Downing, M., Heat of Transition of Ribonuclease A1. *Journal of the American Chemical Society* **1965,** *87* (4), 901-904.

202.   Danforth, R.; Krakauer, H.; Sturtevant, J. M., Differential Calorimetry of Thermally Induced Processes in Solution. *Review of Scientific Instruments* **1967,** *38* (4).

203.   Watson, E. S.; O'Neill, M. J.; Justin, J.; Brenner, N., A Differential Scanning Calorimeter for Quantitative Differential Thermal Analysis. *Analytical Chemistry* **1964,** *36* (7), 1233-1238.

204.   O'Neill, M. J., The Analysis of a Temperature-Controlled Scanning Calorimeter. *Analytical Chemistry* **1964,** *36* (7), 1238-1245.

205.   He, X.; Wolkers, W. F.; Crowe, J. H.; Swanlund, D. J.; Bischof, J. C., In Situ Thermal Denaturation of Proteins in Dunning AT-1 Prostate Cancer Cells: Implication for Hyperthermic Cell Injury. *Annals of Biomedical Engineering* **2004,** *32* (10), 1384-1398.

206.   Bronshteyn, V. L.; Steponkus, P. L., Calorimetric studies of freeze-induced dehydration of phospholipids. *Biophysical journal* **1993,** *65* (5), 1853-1865.

207.   Morley, M. J.; Fursey, G. a. J., The apparent specific heat and enthalpy of fatty tissue during cooling. *International Journal of Food Science & Technology* **1988,** *23* (5), 467-477.

208.   Reading, M.; Luget, A.; Wilson, R., Modulated differential scanning calorimetry. *Thermochimica Acta* **1994,** *238*, 295-307.

209.   Hammerstedt, R. H.; Lovrien, R. E., Calorimetric techniques for metabolic studies of cells and organisms under normal conditions and stress. *J. Exp. Zool.* **1983,** *228* (3), 459-469.

210.   Antonelli, M. L.; Luciani, M.; Silvestroni, L., The microcalorimetric approach to human sperm physiology. *Thermochimica Acta* **1991,** *180*, 107-115.

211.   Nordmark, M. G.; Laynez, J.; Schön, A.; Suurkuusk, J.; Wadsö, I., Design and testing of a new microcalorimetric vessel for use with living cellular systems and in titration experiments. *J. Biochem. Biophys. Methods* **1984,** *10* (3-4), 187-202.

212.   Nogueira-Machado, J. A.; Mares-Guia, M. L.; Lima e Silva, F. C.; Magalhães, T. V. B.; Chaves, M. M., Calorimetry: a highly sensitive technique for evaluating the effect of IL-2, IFN-γ and IL-10 on the response of peripheral blood mononuclear cells. *Thermochimica Acta* **1999,** *327* (1–2), 57-62.

213.   Mares-Guia, M.; do Nascimento, V. V.; Lovrien, R.; Melo, M. N., Microcalorimetric determination of glucose utilization by leishmania. *Thermochimica Acta* **1990,** *172*, 203-211.

214.   Anderson, C. R.; Flickinger, M. C., Monitoring growth and acetic acid secretion by a thermotolerantBacillus using conduction microcalorimetry. *Journal of Industrial Microbiology* **1993,** *12* (2), 114-120.

215.   Torres, F. E.; Kuhn, P.; De Bruyker, D.; Bell, A. G.; Wolkin, M. V.; Peeters, E.; Williamson, J. R.; Anderson, G. B.; Schmitz, G. P.; Recht, M. I., Enthalpy arrays. *Proceedings of the National Academy of Sciences of the United States of America* **2004,** *101* (26), 9517-9522.

216.   Wang, L.; Sipe, D. M.; Xu, Y.; Lin, Q., A MEMS Thermal Biosensor for Metabolic Monitoring Applications. *Journal of Microelectromechanical Systems* **2008,** *17* (2), 318-327.

217.   Zhang, Y.; Tadigadapa, S., Calorimetric biosensors with integrated microfluidic channels. *Biosensors & bioelectronics* **2004,** *19* (12), 1733-43.

218.   Johannessen, E. A.; Weaver, J. M. R.; Bourova, L.; Svoboda, P.; Cobbold, P. H.; Cooper, J. M., Micromachined Nanocalorimetric Sensor for Ultra-Low-Volume Cell-Based Assays. *Analytical Chemistry* **2002,** *74* (9), 2190-2197.

219.   Xiao, K.; Gregoire, J. M.; McCluskey, P. J.; Dale, D.; Vlassak, J. J., Scanning AC nanocalorimetry combined with in-situ x-ray diffraction. *Journal of Applied Physics* **2013,** *113* (24), 243501.

220.   Lee, D.; Sim, G.-D.; Xiao, K.; Choi, Y. S.; Vlassak, J. J., Scanning AC nanocalorimetry study of Zr/B reactive multilayers. *Journal of Applied Physics* **2013,** *114* (21), 214902.

221.   Sadat, S.; Chua, Y. J.; Lee, W.; Ganjeh, Y.; Kurabayashi, K.; Meyhofer, E.; Reddy, P., Room temperature picowatt-resolution calorimetry. *Applied Physics Letters* **2011,** *99* (4), 043106.

222.   Kearns, K. L.; Whitaker, K. R.; Ediger, M. D.; Huth, H.; Schick, C., Observation of low heat capacities for vapor-deposited glasses of indomethacin as determined by AC nanocalorimetry. *The Journal of Chemical Physics* **2010,** *133* (1), 014702.

223.   Lerchner, J.; Wolf, A.; Wolf, G., Recent Developments in Integrated Circuit Calorimetry. *Journal of Thermal Analysis and Calorimetry* **1999,** *57* (1), 241-251.

224.   Merzlyakov, M., Integrated circuit thermopile as a new type of temperature modulated calorimeter. *Thermochimica Acta* **2003,** *403* (1), 65-81.

225.   Xie, B.; Mecklenburg, M.; Danielsson, B.; Öhman, O.; Norlin, P.; Winquist, F., Development of an integrated thermal biosensor for the simultaneous determination of multiple analytes. *Analyst* **1995,** *120* (1), 155-160.

226.   Berger, R. L.; Friauf, W. S.; Cascio, H. E., A Low-Noise Thermistor Bridge for Use in Calorimetry. *Clinical Chemistry* **1974,** *20* (8), 1009-1012.

227.   Moffat, R. J.; Kim, J., *Temperature and Heat Transfer Measurements*. CRC Press: 2004; p 2698.

228.   Garden, J. L.; Chateau, E.; Chaussy, J., Highly sensitive ac nanocalorimeter for microliter-scale liquids or biological samples. *Applied Physics Letters* **2004,** *84* (18), 3597-3599.

229.   Swaminathan, P.; Burke, B. G.; Holness, A. E.; Wilthan, B.; Hanssen, L.; Weihs, T. P.; LaVan, D. A., Optical calibration for nanocalorimeter measurements. *Thermochimica Acta* **2011,** *522* (1), 60-65.

230.   Sadat, S.; Meyhofer, E.; Reddy, P., Resistance thermometry-based picowatt-resolution heat-flow calorimeter. *Applied Physics Letters* **2013,** *102* (16), 163110.

231.   Sadat, S.; Chua, Y. J.; Lee, W.; Ganjeh, Y.; Kurabayashi, K.; Meyhofer, E.; Reddy, P., Room temperature picowatt-resolution calorimetry. *Applied Physics Letters* **2011,** *99* (4), 043106.

232.   Dechaumphai, E.; Chen, R., Sub-picowatt resolution calorimetry with niobium nitride thin-film thermometer. *Review of Scientific Instruments* **2014,** *85* (9), 094903.

233.   Dechaumphai, E.; Chen, R., Sub-picowatt resolution calorimetry with niobium nitride thin-film thermometer. *Review of Scientific Instruments* **2014,** *85* (9), 094903.

234.   Zheng, J.; Wingert, M. C.; Dechaumphai, E.; Chen, R., Sub-picowatt/kelvin resistive thermometry for probing nanoscale thermal transport. *Review of Scientific Instruments* **2013,** *84* (11), 114901.

235.   Echlin, P., *Low-Temperature Microscopy and Analysis*. Springer Science & Business Media: 2013; p 553.

236.   Wang, L.; Lin, Q. In *A MEMS Nanocalorimeter for Biomolecular Characterization*, 2006; 2006; pp 349-352.

237.   Kuwayama, M.; Vajta, G.; Kato, O.; Leibo, S. P., Highly efficient vitrification method for cryopreservation of human oocytes. *Reproductive BioMedicine Online* **2005,** *11* (3), 300-308.

238.   Shi, M.; Ling, K.; Yong, K. W.; Li, Y.; Feng, S.; Zhang, X.; Pingguan-Murphy, B.; Lu, T. J.; Xu, F., High-Throughput Non-Contact Vitrification of Cell-Laden Droplets Based on Cell Printing. *Scientific Reports* **2015,** *5*.

239.   Vajta, G.; Holm, P.; Kuwayama, M.; Booth, P. j.; Jacobsen, H.; Greve, T.; Callesen, H., Open pulled straw (OPS) vitrification: A new way to reduce cryoinjuries of bovine ova and embryos. *Mol. Reprod. Dev.* **1998,** *51* (1), 53-58.

240.   Heo, Y. S.; Nagrath, S.; Moore, A. L.; Zeinali, M.; Irimia, D.; Stott, S. L.; Toth, T. L.; Toner, M., "Universal" vitrification of cells by ultra-fast cooling. *Technology* **2015,** *03* (01), 64-71.

241.   Jin, B.; Kleinhans, F. W.; Mazur, P., Survivals of mouse oocytes approach 100% after vitrification in 3-fold diluted media and ultra-rapid warming by an IR laser pulse. *Cryobiology* **2014,** *68* (3), 419-430.

242.   Hopkins, J. B.; Badeau, R.; Warkentin, M.; Thorne, R. E., Effect of common cryoprotectants on critical warming rates and ice formation in aqueous solutions. *Cryobiology* **2012,** *65* (3), 169-178.

243.   Yi, F.; La Van, D. A., Nanoscale thermal analysis for nanomedicine by nanocalorimetry. *Wiley Interdisciplinary Reviews: Nanomedicine and Nanobiotechnology* **2012,** *4* (1), 31-41.

244.   De Santis, F.; Adamovsky, S.; Titomanlio, G.; Schick, C., Scanning nanocalorimetry at high cooling rate of isotactic polypropylene. *Macromolecules* **2006,** *39* (7), 2562-2567.

245.   Kearns, K. L.; Whitaker, K. R.; Ediger, M. D.; Huth, H.; Schick, C., Observation of low heat capacities for vapor-deposited glasses of indomethacin as determined by AC nanocalorimetry. *Journal of Chemical Physics* **2010,** *133* (1), 014702-(10 pp.).

246.   Ahrenberg, M.; Chua, Y. Z.; Whitaker, K. R.; Huth, H.; Ediger, M. D.; Schick, C., In situ investigation of vapor-deposited glasses of toluene and ethylbenzene via alternating current chip-nanocalorimetry. *The Journal of chemical physics* **2013,** *138*.

247.   Wolf, A.; Hartmann, T.; Bertolini, M.; Schemberg, J.; Grodrian, A.; Lemke, K.; Förster, T.; Kessler, E.; Hänschke, F.; Mertens, F.; Paus, R.; Lerchner, J., Toward high-throughput chip calorimetry by use of segmented-flow technology. *Thermochimica Acta* **2015,** *603*, 172-183.

248.   Torres, F. E.; Recht, M. I.; Coyle, J. E.; Bruce, R. H.; Williams, G., Higher throughput calorimetry: opportunities, approaches and challenges. *Current opinion in structural biology* **2010,** *20* (5), 598-605.

249.   Pyne, A.; Chatterjee, K.; Suryanarayanan, R., Solute crystallization in mannitol–glycine systems—implications on protein stabilization in freeze-dried formulations. *J Pharm Sci* **2003,** *92* (11), 2272-2283.

250.   Chi, E. Y.; Krishnan, S.; Randolph, T. W.; Carpenter, J. F., Physical Stability of Proteins in Aqueous Solution: Mechanism and Driving Forces in Nonnative Protein Aggregation. *Pharmaceutical Research* **2003,** *20* (9), 1325-1336.

251.   Carpenter, J. F.; Pikal, M. J.; Chang, B. S.; Randolph, T. W., Rational design of stable lyophilized protein formulations: some practical advice. *Pharmaceutical research* **1997,** *14* (8), 969-975.

252.   Katayama, D. S.; Carpenter, J. F.; Manning, M. C.; Randolph, T. W.; Setlow, P.; Menard, K. P., Characterization of amorphous solids with weak glass transitions using high ramp rate differential scanning calorimetry. *J Pharm Sci* **2008,** *97* (2), 1013-1024.

253.   Svanidze, A. V.; Huth, H.; Lushnikov, S. G.; Schick, C., Study of phase transition in tetragonal lysozyme crystals by AC-nanocalorimetry. *Thermochimica Acta* **2012,** *544*, 33-37.

254.   WeiB, T.; Igel, G.; Urban, G. In *Chip-Based Scanning Nano-Calorimeter for Protein Stability Analysis in Biosensor Membranes*, Solid-State Sensors, Actuators and Microsystems Conference, 2007. TRANSDUCERS 2007. International, 2007/06//; 2007; pp 1761-1764.

255.   Kim, B. Y. S.; Rutka, J. T.; Chan, W. C. W., Nanomedicine. *New England Journal of Medicine* **2010,** *363* (25), 2434-2443.

256.   Svanidze, A. V.; Huth, H.; Lushnikov, S. G.; Kojima, S.; Schick, C., Phase transition in tetragonal hen egg-white lysozyme crystals. *Applied Physics Letters* **2009,** *95* (26).

257.   Wang, L.; Wang, B.; Lin, Q., Demonstration of MEMS-based differential scanning calorimetry for determining thermodynamic properties of biomolecules. *Sensors and Actuators B: Chemical* **2008,** *134* (2), 953-958.

258.   Olson, E. A.; Efremov, M. Y.; Kwan, A. T.; Lai, S.; Petrova, V.; Schiettekatte, F.; Warren, J. T.; Zhang, M.; Allen, L. H., Scanning calorimeter for nanoliter-scale liquid samples. *Applied Physics Letters* **2000,** *77* (17), 2671-2673.

259.   Yoon, S.-I.; Park, S.-C.; Kim, Y.-J., A micromachined microcalorimeter with split-flow microchannel for biochemical sensing applications. *Sensors and Actuators B: Chemical* **2008,** *134* (1), 158-165.

260.   Lerchner, J.; Wolf, A.; Wolf, G.; Baier, V.; Kessler, E.; Nietzsch, M.; Krügel, M., A new micro-fluid chip calorimeter for biochemical applications. *Thermochimica Acta* **2006,** *445* (2), 144-150.

261.   van Herwaarden, A. W.; Sarro, P. M.; Gardner, J. W.; Bataillard, P., Liquid and gas micro-calorimeters for (bio)chemical measurements. *Sensors and Actuators A: Physical* **1994,** *43* (1–3), 24-30.

138

262.   Bataillard, P.; Steffgen, E.; Haemmerli, S.; Manz, A.; Widmer, H. M., An integrated silicon thermopile as biosensor for the thermal monitoring of glucose, urea and penicillin. *Biosensors and Bioelectronics* **1993,** *8* (2), 89-98.

263.   Esfandyarpour, H.; Zheng, B.; Pease, R. F. W.; Davis, R. W., Structural optimization for heat detection of DNA thermosequencing platform using finite element analysis. *Biomicrofluidics* **2008,** *2* (2), 024102.

264.   Chancellor, E. B.; Wikswo, J. P.; Baudenbacher, F.; Radparvar, M.; Osterman, D., Heat conduction calorimeter for massively parallel high throughput measurements with picoliter sample volumes. *Applied Physics Letters* **2004,** *85* (12), 2408.

265.   Xu, J.; Reiserer, R.; Tellinghuisen, J.; Wikswo, J. P.; Baudenbacher, F. J., A Microfabricated Nanocalorimeter: Design, Characterization, and Chemical Calibration. *Analytical Chemistry* **2008,** *80* (8), 2728-2733.

266.   van Herwaarden, S.; Iervolino, E.; van Herwaarden, F.; Wijffels, T.; Leenaers, A.; Mathot, V., Design, performance and analysis of thermal lag of the UFS1 twin-calorimeter chip for fast scanning calorimetry using the Mettler-Toledo Flash DSC 1. *Thermochimica Acta* **2011,** *522* (1–2), 46-52.

267.   Higuera-Guisset, J.; Rodríguez-Viejo, J.; Chacón, M.; Muñoz, F. J.; Vigués, N.; Mas, J., Calorimetry of microbial growth using a thermopile based microreactor. *Thermochimica Acta* **2005,** *427* (1–2), 187-191.

268.   Johannessen, E. A.; Weaver, J. M. R.; Bourova, L.; Svoboda, P.; Cobbold, P. H.; Cooper, J. M., Micromachined Nanocalorimetric Sensor for Ultra-Low-Volume Cell-Based Assays. *Analytical Chemistry* **2002,** *74* (9), 2190-2197.

269.   Verhaegen, K.; Baert, K.; Simaels, J.; Van Driessche, W., A high-throughput silicon microphysiometer. *Sensors and Actuators A: Physical* **2000,** *82* (1–3), 186-190.

270.   Lerchner, J.; Wolf, A.; Buchholz, F.; Mertens, F.; Neu, T. R.; Harms, H.; Maskow, T., Miniaturized calorimetry — A new method for real-time biofilm activity analysis. *Journal of Microbiological Methods* **2008,** *74* (2–3), 74-81.

271.   He, X.; Bischof, J. C., Quantification of temperature and injury response in thermal therapy and cryosurgery. *Crit. Rev. Biomed. Eng.* **2003,** *31* (5&6).

272.   Rabin, Y.; Taylor, M. J.; Wolmark, N., Thermal expansion measurements of frozen biological tissues at cryogenic temperatures. *Journal of Biomechanical Engineering* **1998,** *120* (2), 259-266.

273.   Rabin, Y.; Shitzer, A., Numerical solution of the multidimensional freezing problem during cryosurgery. *Journal of Biomechanical Engineering* **1998,** *120*, 32-37.

274.   Etheridge, M. L.; Choi, J.; Ramadhyani, S.; Bischof, J. C., Methods for Characterizing Convective Cryoprobe Heat Transfer in Ultrasound Gel Phantoms. *Journal of Biomechanical Engineering* **2013,** *135* (2), 021002-021002.

275.   Rubinsky, B., Cryosurgery. *Annual Reviews of Biomedical Engineering* **2000,** *2*, 157-187.

276.   Rossmanna, C.; Haemmerich, D., Review of temperature dependence of thermal properties, dielectric properties, and perfusion of biological tissues at hyperthermic and ablation temperatures. *Critical Reviews in Biomedical Engineering* **2014,** *42* (6), 467-492.

277.   Pennes, H. H., Analysis of tissue and arterial blood temperatures in the resting human forearm. *Journal of Applied Physiology* **1948,** *1*, 93-122.

278.   Karlsson, J. O.; Toner, M., Long-term storage of tissues by cryopreservation: critical issues. *Biomaterials* **1996,** *17* (3), 243-256.

279.   Natesan, H.; Bischof, J. C., Multi-Scale Thermal Property Measurements for Biomedical Applications. *ACS Biomater. Sci. Eng.* **2016**.

280.   Charny, C. K., Mathematical models of bioheat transfer. *Advances in heat transfer* **1992,** *22*, 19-155.

281.   Diller, K. R., Modeling of bioheat transfer processes at high and low temperatures. *Advances in heat transfer* **1992,** *22*, 157-357.

282.   Arkin, H.; Xu, L. X.; Holmes, K. R., Recent developments in modeling heat transfer in blood perfused tissues. *IEEE Transactions on Biomedical Engineering* **1994,** *41* (2), 97-107.

283.   Baish, J., Microvascular Heat Transfer In *Biomeidcal Engineering Handbook,2* 2000; pp 98-1.

284.   Diller, K. R.; Valvano, J. W.; Pearce, J. A., Bioheat transfer. In *The CRC handbook of thermal engineering*, Kreith, F., Ed. 1999; pp 4114-4187.

285.   Hohne, G.; Hemminger, W.; Flammersheim, H. J., *Differential scanning calorimetry: an introduction for practitioners*. Springer: 1996.

286.   Reading, M.; Hahn, B. K.; Crowe, B. S. Method and apparatus for modulated differential analysis. 5224775, 1993/07/06/, 1993.

287.   Marcus, S. M.; Reading, M. Method and apparatus for thermal conductivity measurements. 5335993, 1994/08/09/, 1994.

288.   Hasgall, P. A.; Neufeld, E.; Gosselin, M. C.; Klingenböck, A.; Kuster, N., IT'IS Database for thermal and electromagnetic parameters of biological tissues. 2015.

289.   Yuan, S.; Diller, K. R., An optical differential scanning calorimeter cryomicroscope. *Journal of Microscopy* **2005,** *218* (2), 85-93.

290.   Duck, F. A., *Physical Properties of Tissues: A Comprehensive Reference Book*. Academic Press: 2013; p 357.

291.   Yuan, D. Y.; Xu, L. X.; Zhu, L.; Holmes, K. R.; Valvano, J. W. In *Perfusion And Temperature Measurements In Hyperthermic Canine Prostates*, Proceedings of the 17th Southern Biomedical Engineering Conference, 1998/02//; 1998; pp 85-85.

292.   Liu, J.; Xu, L. X., Estimation of blood perfusion using phase shift in temperature response to sinusoidal heating at the skin surface. *IEEE Transactions on Biomedical Engineering* **1999,** *46* (9), 1037-1043.

293.   Valvano, J. W., Tissue Thermal Properties and Perfusion. **2010**, 455-485.

294.   Guntur, S. R.; Lee, K. I.; Paeng, D.-G.; Coleman, A. J.; Choi, M. J., Temperature-Dependent Thermal Properties of ex Vivo Liver Undergoing Thermal Ablation. *Ultrasound in Medicine & Biology* **2013,** *39* (10), 1771-1784.

295.   Han, B.; Bischof, J. C., Effect of Thermal Properties on Heat Transfer in Cryopreservation and Cryosurgery. **2002**, 7-15.

296.   Ozisik, M. N., *Heat conduction*. 2 ed.; Wiley: New York, 1993.

297.   Zhang, Y.; Tadigadapa, S., Thermal characterization of liquids and polymer thin films using a microcalorimeter. *Applied Physics Letters* **2005,** *86* (3), 034101.

298.   Bald, W. B.; Fraser, J., Cryogenic surgery. *Reports on Progress in Physics* **1982,** *45* (12), 1381-434.

299.   Lentz, C. P., Thermal conductivity of meats, fats, gelatin gels and ice. *Food Technol* **1961,** *15* (5), 243-247.

300.   Cherneeva, L. I. *Study of thermal properties of foods. In : Report of VNIKHI(Scientific Research Institute of the Refrigeration Industry)*; Gostorgisdat, Moscow, 1956.

301.   Moline, S. W., Thermal properties of foods at low temperatures. *Journal of Food Technology* **1961,** *15*, 228-231.

302.   Henriques, F. C.; Moritz, A. R., Studies of Thermal Injury- I. The Conduction of Heat to and through Skin and the Temperatures Attained Therein. A Theoretical and an Experimental Investigation. *Am J Pathol* **1947,** *23* (4), 530-549.

303.   Bowman, H. F., Heat Transfer and Thermal Dosimetry. *Journal of Microwave Power* **1981,** *16* (2), 121-133.

304.   Avitall, B.; Urboniene, D.; Rozmus, G.; Lafontaine, D.; Helms, R.; Urbonas, A., New Cryotechnology for Electrical Isolation of the Pulmonary Veins. *Journal of Cardiovascular Electrophysiology* **2003,** *14* (3), 281-286.

305.   Kojodjojo, P.; O'Neill, M. D.; Lim, P. B.; Malcolm-Lawes, L.; Whinnett, Z. I.; Salukhe, T. V.; Linton, N. W.; Lefroy, D.; Mason, A.; Wright, I.; Peters, N. S.; Kanagaratnam, P.; Davies, D. W., Pulmonary venous isolation by antral ablation with a large cryoballoon for treatment of paroxysmal and persistent atrial fibrillation: medium-term outcomes and non-randomised comparison with pulmonary venous isolation by radiofrequency ablation. *Heart* **2010,** *96* (17), 1379-1384.

306.   Van Belle, Y.; Janse, P.; Theuns, D.; Szili-Torok, T.; Jordaens, L., One year follow-up after cryoballoon isolation of the pulmonary veins in patients with paroxysmal atrial fibrillation. *Europace: European Pacing, Arrhythmias, and Cardiac Electrophysiology: Journal of the Working Groups on Cardiac Pacing, Arrhythmias, and Cardiac Cellular Electrophysiology of the European Society of Cardiology* **2008,** *10* (11), 1271-1276.

307.   Sarabanda, A. V.; Bunch, T. J.; Johnson, S. B.; Mahapatra, S.; Milton, M. A.; Leite, L. R.; Bruce, G. K.; Packer, D. L., Efficacy and Safety of Circumferential Pulmonary Vein Isolation Using a Novel Cryothermal Balloon Ablation System. *Journal of the American College of Cardiology* **2005,** *46* (10), 1902-1912.

308.   Shenoi, M. M.; Zhang, X.; Venkatasubramanian, R. T.; Grassl, E. D.; George, L.; Schmechel, S.; Coad, J. E.; Bischof, J. C., CT Visualization and Histopathological Assessment of Cryoablation in Pulmonary Veins. **2009**, 207-208.

309.   Cabrera, J. A.; Sánchez-Quintana, D.; Farré, J.; Navarro, F.; Rubio, J. M.; Cabestrero, F.; Anderson, R. H.; Ho, S. Y., Ultrasonic Characterization of the Pulmonary Venous Wall Echographic and Histological Correlation. *Circulation* **2002,** *106* (8), 968-973.

310.   Kato, R.; Lickfett, L.; Meininger, G.; Dickfeld, T.; Wu, R.; Juang, G.; Angkeow, P.; LaCorte, J.; Bluemke, D.; Berger, R.; Halperin, H. R.; Calkins, H., Pulmonary Vein Anatomy in Patients Undergoing Catheter Ablation of Atrial Fibrillation Lessons Learned by Use of Magnetic Resonance Imaging. *Circulation* **2003,** *107* (15), 2004-2010.

311.   Xia, F.; Mao, J.; Ding, J.; Yang, H., Observation of normal appearance and wall thickness of esophagus on CT images. *Eur J Radiol* **2009,** *72* (3), 406-411.

312.   Cahill, D. G., Thermal conductivity measurement from 30 to 750 K: the 3ω method. *Review of Scientific Instruments* **1990,** *61* (2), 802-808.

313.   Lee, S. M.; Cahill, D. G., Heat transport in thin dielectric films. *Journal of Applied Physics* **1997,** *81* (6), 2590-2595.

314.   Cahill, D. G.; Bullen, A.; Seung-Min, L., Interface thermal conductance and the thermal conductivity of multilayer thin films. *High Temperatures High Pressures* **2000,** *32* (2), 135-142.

315.   Kim, D.-H.; Lu, N.; Ghaffari, R.; Kim, Y.-S.; Lee, S. P.; Xu, L.; Wu, J.; Kim, R.-H.; Song, J.; Liu, Z.; Viventi, J.; de Graff, B.; Elolampi, B.; Mansour, M.; Slepian, M. J.; Hwang, S.; Moss, J. D.; Won, S.-M.; Huang, Y.; Litt, B.; Rogers, J. A., Materials for multifunctional balloon catheters with capabilities in cardiac electrophysiological mapping and ablation therapy. *Nat Mater* **2011,** *10* (4), 316-323.

316.   Webb, R. C.; Bonifas, A. P.; Behnaz, A.; Zhang, Y.; Yu, K. J.; Cheng, H.; Shi, M.; Bian, Z.; Liu, Z.; Kim, Y.-S.; Yeo, W.-H.; Park, J. S.; Song, J.; Li, Y.; Huang, Y.; Gorbach, A. M.; Rogers, J. A., Ultrathin conformal devices for precise and continuous thermal characterization of human skin. *Nat Mater* **2013,** *12* (11).

317.   Klinker, L.; Lee, S.; Work, J.; Wright, J.; Ma, Y.; Ptaszek, L.; Webb, R. C.; Liu, C.; Sheth, N.; Mansour, M.; Rogers, J. A.; Huang, Y.; Chen, H.; Ghaffari, R., Balloon catheters with integrated stretchable electronics for electrical stimulation, ablation and blood flow monitoring. *Extreme Mechanics Letters* **2015,** *3*, 45-54.

318.   Lee, S. P.; Klinker, L. E.; Ptaszek, L.; Work, J.; Liu, C.; Quivara, F.; Webb, C.; Dagdeviren, C.; Wright, J. A.; Ruskin, J. N.; Slepian, M.; Huang, Y.; Mansour, M.; Rogers, J. A.; Ghaffari, R., Catheter-Based Systems With Integrated Stretchable Sensors and Conductors in Cardiac Electrophysiology. *Proceedings of the IEEE* **2015,** *103* (4), 682-689.

319.   Wang, H.; Sen, M., Analysis of the 3-omega method for thermal conductivity measurement. *International Journal of Heat and Mass Transfer* **2009,** *52* (7-8), 2102-2109.

320.   Dames, C., Measuring the Thermal Conducitivity of Thin Films: 3 omega and Related Electrothermal Methods. *Annual Review of Heat Transfer* **2013,** *16* (1), 7-49.

321.   Vargaftik, N. B., *Handbook of Thermal Conductivity of Liquids and Gases*. CRC Press: 1993; p 362.

322.   Pease, G. R.; Wong, S. T. S.; Roos, M. S.; Rubinsky, B., Mr image-guided control of cryosurgery. *Journal of Magnetic Resonance Imaging* **1995,** *5* (6), 753-760.

323.   Asirvatham, S. J.; Bruce, C. J.; Friedman, P. A., Advances in imaging for cardiac electrophysiology : Coronary Artery Disease. *Coronary Artery Diesease* **2003,** *14* (1), 3-13.

324.   Butts, K.; Sinclair, J.; Daniel, B. L.; Wansapura, J.; Pauly, J. M., Temperature quantitation and mapping of frozen tissue. *Journal of Magnetic Resonance Imaging* **2001,** *13* (1), 99-104.

325.   Daniel, B. L.; Butts, K.; Block, W. F., Magnetic resonance imaging of frozen tissues: Temperature-dependent MR signal characteristics and relevance for MR monitoring of cryosurgery. *Magnetic Resonance in Medicine* **1999,** *41* (3), 627-630.

326.   Gilbert, J. C.; Rubinsky, B.; Roos, M. S.; Wong, S. T. S.; Brennan, K. M., MRI-monitored cryosurgery in the rabbit brain. *Magnetic Resonance Imaging* **1993,** *11* (8), 1155-1164.

327.   Wansapura, J. P.; Daniel, B. L.; Vigen, K. K.; Butts, K., In Vivo MR Thermometry of Frozen Tissue Using R2* and Signal Intensity1. *Acad. Radiol.* **2005,** *12* (9), 1080-1084.

328.   Gilbert, J. C.; Onik, G. M.; Hoddick, W. K.; Rubinsky, B., Real time ultrasonic monitoring of hepatic cryosurgery. *Cryobiology* **1985,** *22* (4), 319-330.

329.   Onik, G.; Cooper, C.; Goldberg, H. I.; Moss, A. A.; Rubinsky, B.; Christianson, M., Ultrasonic characteristics of frozen liver. *Cryobiology* **1984,** *21* (3), 321-328.

330.   Bruce, C. J.; Packer, D. L.; Seward, J. B., Intracardiac doppler hemodynamics and flow: new vector, phased-array ultrasound-tipped catheter. *American Journal of Cardiology* **1999,** *83* (10), 1509-1512.

331.   Lomas, C. G., *Fundamentals of Hot Wire Anemometry*. Cambridge University Press: 2011; p 225.

332.   Bruun, H. H., Hot-Wire Anemometry: Principles and Signal Analysis. *Meas Sci Technol* **1996,** *7* (10), null.

333.   Incropera, F. P., *Fundamentals of Heat and Mass Transfer*. John Wiley & Sons: 2011; p 2249.

334.   Andreano, A.; Brace, C. L., A Comparison of Direct Heating During Radiofrequency and Microwave Ablation in Ex Vivo Liver. *Cardiovasc Intervent Radiol* **2013,** *36* (2), 505-511.

335.   Onik, G. M.; Cohen, J. K.; Reyes, G. D.; Rubinsky, B.; Chang, Z.; Baust, J., Transrectal ultrasound-guided percutaneous radical cryosurgical ablation of the prostate. *Cancer* **1993,** *72* (4), 1291-1299.

336.   Onik, G.; Rubinsky, B.; Zemel, R.; Weaver, L.; Diamond, D.; Cobb, C.; Porterfield, B., Ultrasound-guided hepatic cryosurgery in the treatment of metastatic colon carcinoma. Preliminary results. *Cancer* **1991,** *67* (4), 901-907.

337.   Sandison, G. A.; Loye, M. P.; Rewcastle, J. C.; Hahn, L. J.; Saliken, J. C.; McKinnon, J. G.; Donnelly, B. J., X-ray CT monitoring of iceball growth and thermal distribution during cryosurgery. *Physics in Medicine and Biology* **1998,** *43* (11).

338.   Schwartz, B. F.; Rewcastle, J. C.; Powell, T.; Whelan, C.; Manny Jr, T.; Vestal, J. C., Cryoablation of small peripheral renal masses: A retrospective analysis. *Urology* **2006,** *68* (1, Supplement), 14-18.

339.   Haïssaguerre, M.; Gencel, L.; Fischer, B.; Le Métayer, P.; Poquet, F.; Marcus, F. I.; Clémenty, J., Successful Catheter Ablation of Atrial Fibrillation. *Journal of Cardiovascular Electrophysiology* **1994,** *5* (12), 1045-1052.

340.   Kuck, K.-H.; Fürnkranz, A., Cryoballoon Ablation of Atrial Fibrillation. *Journal of Cardiovascular Electrophysiology* **2010,** *21* (12), 1427-1431.

341.   Haeusler, K. G.; Koch, L.; Ueberreiter, J.; Endres, M.; Schultheiss, H.-P.; Heuschmann, P. U.; Schirdewan, A.; Fiebach, J. B., Stroke risk associated with balloon based catheter ablation for atrial fibrillation: Rationale and design of the MACPAF Study. *BMC Neurology* **2010,** *10* (1).

342.   Reddy, V. Y.; Neuzil, P.; Themistoclakis, S.; Danik, S. B.; Bonso, A.; Rossillo, A.; Raviele, A.; Schweikert, R.; Ernst, S.; Kuck, K.-H.; Natale, A., Visually-Guided Balloon Catheter Ablation of Atrial Fibrillation Experimental Feasibility and First-in-Human Multicenter Clinical Outcome. *Circulation* **2009,** *120* (1), 12-20.

343.   Doppalapudi, H.; Yamada, T.; Kay, G. N., Complications during catheter ablation of atrial fibrillation: Identification and prevention. *Heart Rhythm* **2009,** *6* (12, Supplement), S18-S25.

344.   Calkins, H.; Reynolds, M. R.; Spector, P.; Sondhi, M.; Xu, Y.; Martin, A.; Williams, C. J.; Sledge, I., Treatment of Atrial Fibrillation With Antiarrhythmic Drugs or Radiofrequency Ablation Two Systematic Literature Reviews and Meta-Analyses. *Circ Arrhythm Electrophysiol* **2009,** *2* (4), 349-361.

345.   Haíssaguerre, M.; Jaís, P.; Shah, D. C.; Gencel, L.; Pradeau, V.; Garrigues, S.; Chouairi, S.; Hocini, M.; Le Métayer, P.; Roudaut, R.; Clémenty, J., Right and Left Atrial Radiofrequency Catheter Therapy of Paroxysmal Atrial Fibrillation. *Journal of Cardiovascular Electrophysiology* **1996,** *7* (12), 1132-1144.

346.   Malmborg, H.; Lönnerholm, S.; Blomström-Lundqvist, C., Acute and clinical effects of cryoballoon pulmonary vein isolation in patients with symptomatic paroxysmal and persistent atrial fibrillation. *Europace* **2008,** *10* (11), 1277-1280.

347.   Ahmed, H.; Neuzil, P.; d'Avila, A.; Cha, Y.-M.; Laragy, M.; Mares, K.; Brugge, W. R.; Forcione, D. G.; Ruskin, J. N.; Packer, D. L.; Reddy, V. Y., The esophageal effects of cryoenergy during cryoablation for atrial fibrillation. *Heart Rhythm* **2009,** *6* (7), 962-969.

348.   Kuck, K.-H.; Fürnkranz, A.; Chun, K. R. J.; Metzner, A.; Ouyang, F.; Schlüter, M.; Elvan, A.; Lim, H. W.; Kueffer, F. J.; Arentz, T.; Albenque, J.-P.; Tondo, C.; Kühne, M.; Sticherling, C.; Brugada, J., Cryoballoon or radiofrequency ablation for symptomatic paroxysmal atrial fibrillation: reintervention, rehospitalization, and quality-of-life outcomes in the FIRE AND ICE trial. *Eur Heart J* **2016,** *37* (38), 2858-2865.

349.   Packer, D. L.; Kowal, R. C.; Wheelan, K. R.; Irwin, J. M.; Champagne, J.; Guerra, P. G.; Dubuc, M.; Reddy, V.; Nelson, L.; Holcomb, R. G.; Lehmann, J. W.; Ruskin, J. N.; Investigators, S. A. F. C., Cryoballoon Ablation of Pulmonary Veins for Paroxysmal Atrial Fibrillation: First

Results of the North American Arctic Front (STOP AF) Pivotal Trial. *Journal of the American College of Cardiology* **2013,** *61* (16), 1713-1723.

350.   Lalonde, J.-P.; Groves, R. E.; Laske, T. G.; Iaizzo, P. A.; Bischof, J. C. Feedback system for cryoablation of cardiac tissue. US20150119868A1, 2015/04/30/, 2015.

351.   Tian, L.; Li, Y.; Webb, R. C.; Krishnan, S.; Bian, Z.; Song, J.; Ning, X.; Crawford, K.; Kurniawan, J.; Bonifas, A.; Ma, J.; Liu, Y.; Xie, X.; Chen, J.; Liu, Y.; Shi, Z.; Wu, T.; Ning, R.; Li, D.; Sinha, S.; Cahill, D. G.; Huang, Y.; Rogers, J. A., Flexible and Stretchable 3ω Sensors for Thermal Characterization of Human Skin. *Advanced Functional Materials* **2017,** *27* (26), 1701282.

352.   Webb, R. C.; Pielak, R. M.; Bastien, P.; Ayers, J.; Niittynen, J.; Kurniawan, J.; Manco, M.; Lin, A.; Cho, N. H.; Malyrchuk, V.; Balooch, G.; Rogers, J. A., Thermal Transport Characteristics of Human Skin Measured In Vivo Using Ultrathin Conformal Arrays of Thermal Sensors and Actuators. *PloS one* **2015,** *10* (2).

353.   Mishra, V.; Hardin, C. L.; Garay, J. E.; Dames, C., A 3 omega method to measure an arbitrary anisotropic thermal conductivity tensor. *Review of Scientific Instruments* **2015,** *86* (5), 054902.

354.   Kim, Y.-H.; Marom, E. M.; Herndon, J. E.; McAdams, H. P., Pulmonary vein diameter, cross-sectional area, and shape: CT analysis. *Radiology* **2005,** *235* (1), 43-49; discussion 49-50.

355.   Davalos, R.; Rubinsky, B. Tissue ablation with irreversible electroporation. US8048067 B2, 2011/11/01/, 2011.

356.   Sugrue, A.; Maor, E.; Ivorra, A.; Vaidya, V.; Witt, C.; Kapa, S.; Asirvatham, S., Irreversible electroporation for the treatment of cardiac arrhythmias. *Expert Review of Cardiovascular Therapy* **2018,** *16* (5), 349-360.

Appendix A. Reusable Bi-Directional 3ω Sensor to Measure Thermal Conductivity of 100-micron Thick Biological Tissues

The following chapter appeared in publication:

A.1. Abstract

Accurate knowledge of the thermal conductivity (k) of biological tissues is important for cryopreservation, thermal ablation, and cryosurgery. Here, we adapt the 3ω method—widely used for rigid, inorganic solids—as a reusable sensor to measure k of soft biological samples, two orders of magnitude thinner than conventional tissue characterization methods. Analytical and numerical studies quantify the error of the commonly used "boundary mismatch approximation" of the bi-directional 3ω geometry, confirm that the generalized slope method is exact in the low-frequency limit, and bound its error for finite frequencies. The bi-directional 3ω measurement device is validated using control experiments to within ± 2% (liquid water, std. dev.) and ± 5% (ice). Measurements of mouse liver cover a temperature range from -69 ℃ to + 33 ℃. The liver results are independent of sample thicknesses from 3 mm down to 100 μm, and agree with available literature for non-mouse liver to within the measurement scatter.

Appendix B. Biomaterial Scaffolds for Non-Invasive Focal Hyperthermia as a Potential Tool to Ablate Metastatic Cancer Cells

The following chapter appeared in publication:

Pelaez, F., Manuchehrabadi, N., Roy, P., Natesan, H., Wang, Y., Racila, E., ...,Bischof, J., & Azarin, S. M. (2018). Biomaterial scaffolds for non-invasive focal hyperthermia as a potential tool to ablate metastatic cancer cells. Biomaterials, 166, 27-37.

B.1 Abstract

Currently, there are very few therapeutic options for treatment of metastatic disease, as it often remains undetected until the burden of disease is too high. Microporous poly(ε-caprolactone) biomaterials have been shown to attract metastasizing breast cancer cells *in vivo* early in tumor progression. In order to enhance the therapeutic potential of these scaffolds, they were modified such that infiltrating cells could be eliminated with non-invasive focal hyperthermia. Metal disks were incorporated into poly(ε-caprolactone) scaffolds to generate heat through electromagnetic induction by an oscillating magnetic field within a radiofrequency coil. Heat generation was modulated by varying the size of the metal disk, the strength of the magnetic field (at a fixed frequency), or the type of metal. When implanted subcutaneously in mice, the modified scaffolds were biocompatible and became properly integrated with the host tissue. Optimal parameters for *in vivo* heating were identified through a combination of computational modeling and *ex vivo* characterization to both predict and verify heat transfer dynamics and cell death kinetics during inductive heating. *In vivo* inductive heating of implanted, tissue-laden composite scaffolds led to tissue necrosis as seen by histological analysis. The ability to thermally ablate captured cells non-invasively using biomaterial scaffolds has the potential to extend the application of focal thermal therapies to disseminated cancers.

Appendix C. Measurement of Specific Heat and Crystallization in VS55, DP6 and M22

Cryoprotectant Systems with and without Sucrose.

The following chapter appeared in publication:

C.1 Abstract

Cryopreservation represents one if not the only long-term option for tissue and perhaps future organ banking. In one particular approach, cryopreservation is achieved by completely avoiding ice formation (or crystallization) through a process called vitrification. This "ice-free" approach to tissue banking requires a combination of high concentration cryoprotective additives such as M22 (9.4 M), VS55 (8.4 M) or DP6 (6 M) and sufficiently fast rates of cooling and warming to avoid crystallization. In this paper we report the temperature-dependent specific heat capacity of the above-mentioned cryoprotective additives in small volumes (10 mg sample pans) at rates of 5 and 10 °C/min using a commercially available DSC (TA Instruments Q1000), in the temperature range of -150°C to 30°C. This data can be utilized in heat-transfer models to predict thermal histories in a cryopreservation protocol. More specifically, the effects of temperature dependence of the specific heat due to presence of three different phases (liquid, ice and vitreous phase) can dramatically impact the thermal history and therefore the outcome of the cryopreservation procedure. The crystallization potential of these CPAs was also investigated by studying cases of maximal and minimal crystallization in VS55 and DP6, where M22 did not crystallize under any rates tested. To further reduce crystallization in VS55 and DP6, a stabilizing sugar (sucrose) was

added in varying concentrations (0.15 M, 0.6 M) and shown to further reduce crystallization, particularly in VS55, at modest rates of cooling (1, 5 and 10 °C/min).